AD-A272 851

CUMENTATION PAGE

Form Approved
OMB No. 0704-0188

1. AGENCY USE ONLY (Leave blank)	2. REPORT DATE	3. REPORT TYPE AND DATES COVERED
	10/15/93	Final Tech Report: 8/15/92-7/31/93

4. TITLE AND SUBTITLE

(U) Liquid-Phase Circulation and Mixing in Multicomponent Droplets Vaporizing in a Laminar Convective Environment

5. FUNDING NUMBERS

PE - 61102F
PR - 2308
SA - BS
G - F49620-92-J-0476

6. AUTHOR(S)

Constantine M. Megaridis
Joseph T. Hodges

7. PERFORMING ORGANIZATION NAME(S) AND ADDRESS(ES)

University of Illinois at Chicago
Dept. of Mech. Eng. (M/C251)
842 W. Taylor Street
Chicago IL 60607-7022

8. PERFORMING ORGANIZATION REPORT NUMBER

AFOSR-TR- 93 0823

9. SPONSORING/MONITORING AGENCY NAME(S) AND ADDRESS(ES)

AFOSR/NA
110 Duncan Avenue, Suite B115
Bolling AFB DC 20332-0001

10. SPONSORING/MONITORING AGENCY REPORT NUMBER

11. SUPPLEMENTARY NOTES

12a. DISTRIBUTION/AVAILABILITY STATEMENT

Approved for public release; distribution is unlimited

12b. DISTRIBUTION CODE

13. ABSTRACT (Maximum 200 words)

A combined theoretical/experimental study of internal circulation induced by surface rotation of mm-sized pendant droplets was completed. The study consistently revealed predictable helical three–dimensional circulation patterns that bear little resemblance to the two–dimensional toroidal internal flows established within droplets under axisymmetric convective conditions. The observed complex flow patterns suggested substantially enhanced liquid mixing rates, thus indicating that droplet spinning may be very important in practical situations involving droplet convective transport. In a parallel study, charged droplets up to $100\mu m$ in diameter were stably levitated and exposed to uniform air streams with Reynolds numbers up to 3. The evaporation rate of levitated dodecanol droplets was measured under quiescent conditions and followed the familiar d^2–law. No detailed information could be obtained on internal circulation of levitated droplets impregnated with scattering or fluorescent agents.

14. SUBJECT TERMS	15. NUMBER OF PAGES
Droplet Evaporation, Droplet Internal Mixing, Droplet Rotation, Flow Visualization, Internal Circulation, Multicomponent Droplets	92
	16. PRICE CODE

17. SECURITY CLASSIFICATION OF REPORT	18. SECURITY CLASSIFICATION OF THIS PAGE	19. SECURITY CLASSIFICATION OF ABSTRACT	20. LIMITATION OF ABSTRACT
Unclassified	Unclassified	Unclassified	UL

1 Summary of Research Progress

This report summarizes the progress in various aspects of the work in three different categories: suspended droplets, levitated droplets and numerically simulated droplets.

1.1 Suspended Droplets: Internal Circulation Induced by Surface–Driven Rotation

A combined theoretical/experimental study of droplet internal circulation induced by surface rotation has been completed. Droplet interface rotation is expected to arise in actual processes when a shear or locally rotating flow imposes a spinning motion to the droplet surface. The rotational frequencies considered were of the order of several Hz, and corresponded to low values of rotational Reynolds numbers. A numerical model was formulated to quantify the fluid transport processes within a droplet whose surface is subjected to a steady rotation about its own axis. Planar laser-induced fluorescence techniques were employed to provide high-resolution images of flow patterns developed within mm-sized pendant droplets, that were exposed to steady, laminar, air streams to induce surface rotation. The experimentally observed flow patterns showed excellent agreement with those predicted by the numerical model.

The study consistently revealed helical (spiral) three dimensional circulation patterns that bear little resemblance to the toroidal internal flows established within droplets under axisymmetric conditions. The rotation of the liquid interface around the droplet axis induced a secondary fluid motion, directed inward from the equator, and outward to the poles of rotation. The steady liquid motion along the azimuthal coordinate resembled a rigid–body rotation only at the outer layers of the droplet, while it lagged substantially in the core of the droplet. The results showed that processes involving shear–induced droplet rotation may exhibit substantially enhanced liquid mixing rates, thus suggesting that droplet spinning may be very important in practical situations involving droplet convective transport. The details of the modeling and experimental aspects of this study are given in Appendix A.

1.2 Droplet Levitation Experiments

An electrodynamic balance was designed and built to levitate individual micron-sized droplets. This apparatus was used to investigate processes of mass transport and internal circulation of droplets exposed to convective environments. However, the visualization of internal circulation within levitated droplets proved to be an elusive goal – difficult to realize due to a number of experimental problems associated with such microscopic systems. Nevertheless, many technical problems were overcome, and several diagnostics were developed in the course of the experimental work. The primary experimental achievements were:

a) design and assembly of a proportional-integral-derivative (PID) controller.

b) stable levitation of droplets up to $100\mu m$ in diameter in the presence of a laminar air jet.

c) time–resolved measurements of absolute droplet size via elastic light scattering profiles.

d) time–resolved measurement of relative droplet size by changes in the balance null point voltage.
e) high magnification imaging of the droplet interior using depolarized elastic light scattering from inclusions.

a) PID controller

A microprocessor-based real-time control system was designed and assembled. This system consists of an illuminating laser and associated optics, a particle position-tracking element (512 element linear photodiode array), a 20 KHz data acquisition board installed in a 386-based personal computer, and a custom-made dc power supply. The principle of operation is as follows. A collimated laser beam is used to cast a shadow of the droplet onto the photodiode array (PDA). The PDA is triggered and scanned by the data acquisition board so that the relative position of the shadow centroid can be determined by the computer. With the droplet position known, the control error function is calculated and the revised null point voltage is fed back to the balance dc power supply. The control signal can be updated at a rate of the order of 10 Hz.

Real-time control of the null point voltage allows one to investigate dynamic systems where the droplet mass and/or external forces are changing with time. One can therefore accommodate evaporating or growing droplets, as well as situations where drag forces on the droplet are variable. It was clearly demonstrated that the controller functioned properly for these two dynamic situations where the null point voltage was time dependent.

b) Droplet levitation in an air stream

The upper flowrate limit for stable levitation in the presence of an air flow was found to depend significantly on droplet diameter and flow configuration. In order to maintain stability, the air stream needed to be laminar and symmetric so that the drag force remained constant without a radial component. Among the nozzles considered, were three different straight-edged orifices with internal diameters of 1.7 mm, 1.5 mm and 0.5 mm, respectively. Each tube was mounted coincident with the bottom electrode axis and its edge flush with the apex of that electrode. It was found that the smallest i.d. tube produced a jet of poor quality. The optimal nozzle had an i.d. of 1.5 mm. Using this nozzle, the limit of stability was measured for three different droplet sizes. The results, shown in Table 1 for glycerol or dioctyl–phthalate droplets, indicate that the stability increased nonlinearly with droplet diameter. From the standpoint of internal circulation phenomena, it would have been desirable to consider Reynolds numbers as great as 100. However, in order to achieve droplet Reynolds numbers of this magnitude, droplets of the order of 1 mm (and hence dc voltages as high as 5 kv) were needed. These requirements could not be met with the present system. Instead, the maximum observable Reynolds number was of the order of 3.0 for a 90 μm–diameter droplet.

c) Elastic light scattering measurements

The droplet diameter was easily measured to an accuracy of the order of 10% by imaging the droplet under high magnification using strobe illumination and a video microscope system. However, for better sizing accuracy, principles of elastic light scattering were exploited. To this end,

Table 1: Variation of stability limit with diameter of levitated droplet

Diameter (microns)	g's of drag force	V_{max} (cm/s)	Re_{max}
90	3.0	53.4	3.0
50	3.8	25.0	0.79
20	5.3	6.0	0.08

the angular profile of elastically scattered light from a slowly evaporating glycerol was monitored using a CCD camera (with objective lens removed). This time dependent measured profile was compared with predictions based on the Lorenz-Mie theory (LMT) of elastic light scattering. For each angular profile, a best fit diameter (experiment to theory) was obtained. Two representative scans are depicted in Figs. 1a-b, for a droplet of nominal diameter $15.5\mu m$. The solid line represents the LMT best fit, and the dashed line indicates the measured profile. Note the significant and measurable changes in the scattering profile yielded by a $0.1\mu m$ reduction in droplet diameter. The variation of the measured diameter vs. time, for the same glycerol droplet is shown in Fig. 1c. For this droplet, evaporation was quite slow, proceeding on the order of $0.5\mu m$/h. The particular case shown in Fig. 1 corresponds to a 15% reduction of the liquid mass.

d) Droplet evaporation using variation of null point voltage

For more rapidly evaporating droplets, it was found that the null point voltage is proportional to droplet mass – assuming no charge losses. Hence, relative changes in the droplet mass were tracked by maintaining evaporating droplets at the null point and concurrently monitoring the dc voltage. Figures 2a-c are based on the null point data for an evaporating droplet of dodecanol. The null point voltage, shown in Fig. 2a, decayed monotonically until about 22 min after injection. At this point, the voltage discontinuously increased, an event that was attributed to the loss of electrical charge from the surface of the droplet. In Fig. 2b, a plot of $Vnull$ to the 2/3 power, (which is proportional to the droplet diameter squared) shows that the evaporating droplet follows the familiar d^2–law up to the moment of sudden charge loss. The slope of this linear curve was found to be -0.0354/min. As seen in Fig. 2c, a droplet size reduction from an initial diameter of $20\mu m$ to $5\mu m$ occurred in about 20 minutes, at which instant the discontinuous charge loss occurred.

e) Light scattering from inclusions

As expected, the image of a perfectly homogeneous droplet illuminated by a laser beam showed no contrast, therefore, no information could be obtained on internal circulation. In order to visualize the field within a droplet, it was necessary that an emission or scattering source be placed within the droplet. Both the fluorescence and scattering approaches were attempted by levitating droplets made from a mixture of $6\mu m$ polymer fluorescent microspheres in glycerol.

For the purpose of droplet interior visualization, it was found that the scattering method worked best with the following configuration. The incident beam was linearly polarized and the elastically

scattered light was observed under high magnification at 90 degrees through a microscope/video camera apparatus. The best images were obtained by placing a cross-polarized polarization filter in front of the receiving optics. With this arrangement, the very bright glare spots were suppressed, so that the depolarized scattered light was dominant. A very bright ring or 'halo' was clearly seen inside the droplet. There was, however, very little emission apparent in the droplet center. Furthermore, the images were not sufficiently resolved in order to see the motion of individual flow tracing particles. Nevertheless, given a sufficiently large droplet and an appropriate concentration of scattering particles, it is likely that this method would reveal patterns of motion as the scattering particles are convected within the droplet.

The fluorescence visualization method was unsuccessful because, for the droplets observed in this work (of the order of $100\mu m$ or less), the laser dye became photobleached. This process occurred because of the continuous illumination of a relatively small mass of fluorescent dye contained within the micron-sized droplets. Photobleaching occurs because each dye molecule can undergo only a finite amount of excitations before being chemically altered. It is noted that photobleaching effects may be avoided in droplet stream configurations and in relatively large systems where 'fresh' dye can be fed into the probe volume.

1.3 Numerical Models

a) Multicomponent Droplets

A detailed numerical model was developed to examine multicomponent droplet evaporation in a uniform, high-temperature gaseous stream. The model was based on the work of Megaridis and Sirignano (1990) [*23rd Intl. Symposium on Combustion*, p. 1413], and accounts for variable gas- and liquid-phase thermophysical properties. Detailed data on the temporal and spatial variation of the liquid-phase concentration fields throughout the lifetime of a n-octane/benzene droplet provided new insight on the liquid mass-transport mechanisms within typical vaporizing hydrocarbon droplets. Overall mass evaporation rates from a bicomponent droplet surface showed an increasing trend during the early stages and achieved a temporal maximum near the droplet half-life point. The evaporation rates decreased monotonically thereafter, as the more volatile species was gradually depleted from the droplet interior. Droplet thermal expansion occurred under certain conditions as a result of the substantial reduction of liquid-phase densities during the heating stage of the droplet lifetime. The model predictions also showed that when droplet swelling occurred, it was generally limited, causing only small deviations from the initial droplet volume. However, the consideration of temperature-dependent liquid densities effectively enhanced liquid mass evaporation rates, which in turn reduced the droplet lifetime by as much as 25% under the conditions investigated in this study. In addition, the model predictions showed that the classical d^2-law for liquid droplet evaporation was not valid for a substantial portion of the droplet lifetime, especially during the heating stage of the liquid. In general, our bicomponent droplet simulations indicated that the variation of liquid densities with temperature must be taken into account for an adequate representation of the transport processes in droplet convective vaporization. Finally, the effect of the variation of liquid heat capacities with temperature proved to be rather minor, thus suggesting that a concentration

dependent approach is adequate for most practical applications. The details of this work are given in Appendix B.

b) Single–Component Droplets

The data of a recent experimental investigation performed by Wong and Lin (1992) [*J. Fluid Mech.* 237, p. 671] on suspended, evaporating droplets was used to evaluate and validate the methods employed in a detailed numerical model simulating the vaporization behavior of liquid droplets vaporizing at high-temperature laminar convective conditions. A series of comparisons was performed between model-predicted and experimentally-measured vaporization rates and internal temperature distributions at atmospheric pressures and Reynolds numbers below 100, as representative of practical situations of interest. The agreement between experimental measurements and model predictions on the temporal variation of certain temperatures in the droplet interior was good, with largest discrepancies occurring near the droplet center. The predicted temperature distributions in the droplet interior were also in very good agreement with those measured experimentally throughout the droplet lifetime, with the exception of regions near the droplet center and during the early stages of the droplet lifetime. Both experiments and modeling agreed on the establishment of internal circulation in liquid vaporizing droplets exposed to laminar, high-temperature, gaseous flows. In addition, the model predicted slightly higher liquid vaporization rates, as indicated by consistently lower values (up to 10 %) of the droplet diameter throughout the droplet lifetime.

Comparisons of the calculated internal droplet temperature distributions for two different values of the Reynolds number showed that a considerable increase of free-stream momentum failed to have a substantial effect on the temperature distributions within the droplet interior. This observation was consistent with the results reported in the relevant experimental investigation. However, the model predictions suggested that liquid-phase circulation and vaporization dynamics are highly influenced by ambient momentum. The model showed that substantially increased liquid viscosities affect the establishment and the strength of the liquid-phase motion. On the other hand, the experimental observations concluded that substantially higher liquid viscosities eliminate the liquid-phase motion entirely.

The comparisons showed that the experiment suggests a weaker liquid-phase motion than that predicted by the model. Possible sources for disagreement between experiment and theory were attributed to the context of the experimental setup and the limitations of the employed instrumentation. In conclusion, the overall agreement between model predictions and experimental measurements showed that modeling can be used in a reliable manner to examine liquid-droplet convective evaporation under conditions that are not easily reproduced experimentally, or when time constraints prohibit any experimental setup implementation. The details of this study are given in Appendix C.

2 Personnel

The Principal investigator collaborated with Dr. Joseph T. Hodges of NIST throughout the duration of the program. Two graduate students were also involved and contributed to the completion of the study: Mr. Joseph M. Day who will be receiving his M.S. degree this Fall, and Mr. Jun Xin who is a Ph.D. candidate in the Department of Mechanical Engineering of UIC.

3 Publications

The following peer-reviewed publications appeared in the archival literature during the past year:

1. C. M. Megaridis, "Comparison Between Experimental Measurements and Numerical Predictions of Internal Temperature Distributions of a Droplet Vaporizing under High-Temperature Convective Conditions," *Combustion and Flame* **93**, 287-302, 1993.

2. C. M. Megaridis, "Liquid-Phase Variable Property Effects in Multicomponent Droplet Convective Evaporation," *Combustion Science and Technology* **92**, 291-312, 1993.

The following peer-reviewed publications will be appearing soon or are currently under review:

1. T. M. Shih and C. M. Megaridis, "Finite-Difference Discretization Effects on Multidimensional Droplet Evaporation Modeling," *Numerical Heat Transfer.*

2. J. T. Hodges, C. M. Megaridis, J. Xin, J. M. Day and C. Presser, "Three dimensional internal droplet circulation induced by surface driven rotation," *Physics of Fluids.*

4 Presentation

1. J. T. Hodges, J. M. Day and C. M. Megaridis, "Visualization of Convective Transport within Droplets by Planar Laser Induced Fluorescence," 12^{th} Annual Meeting of the American Association for Aerosol Research, Oak Brook, Illinois, October 11-15, 1993.

5 Interactions Related to the Research

The program combined the resources and expertise at two Institutions; the University of Illinois at Chicago (UIC) and the National Institute of Standards and Technology (NIST). Close interaction was followed and frequent visits were exchanged between the research collaborators during the one-year duration of the study. In addition, three industrial firms (Nalco Fuel Tech, Clean Air Engineering, Advanced Fuel Research) have expressed interest in the AFOSR-sponsored work.

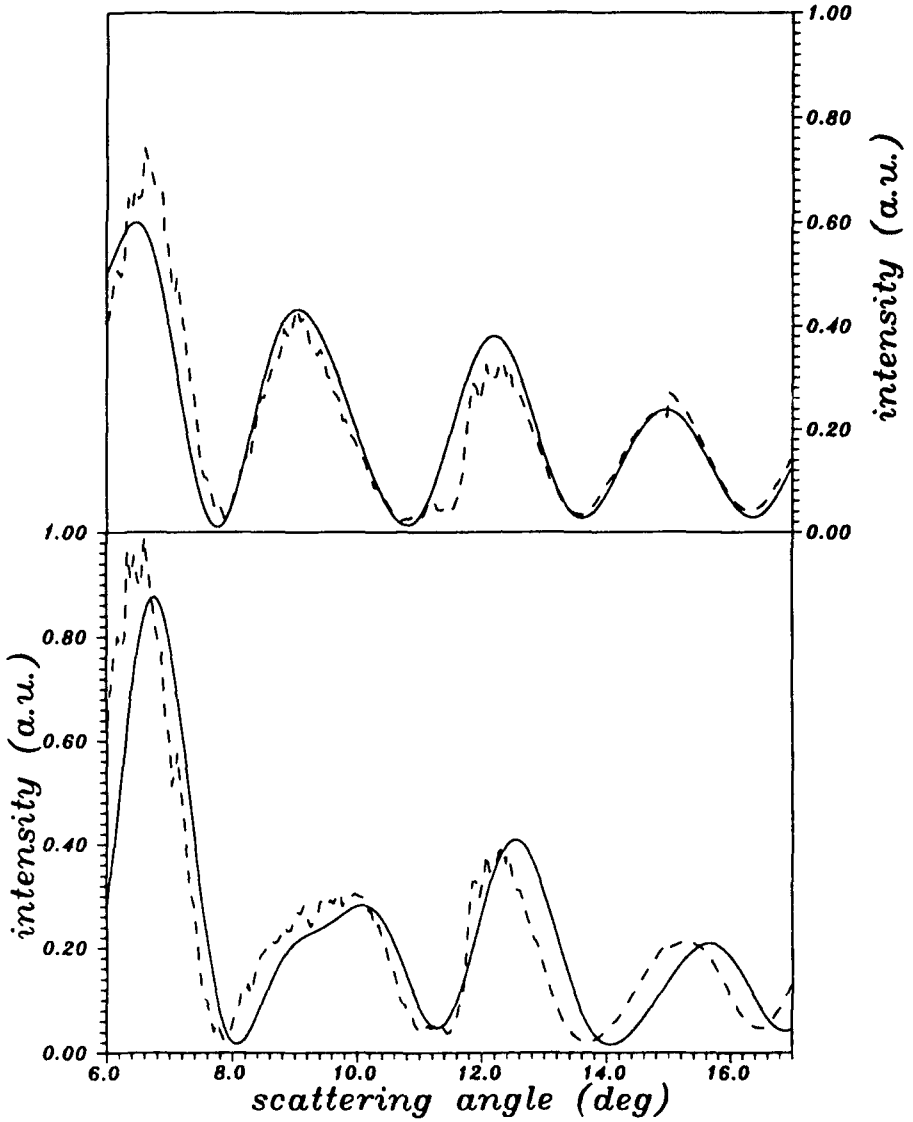

Figure 1a-b. Measured (dashed line) and LMT best fit (solid line) for an evaporating glycerol droplet. (a) upper curve: $t - t_0$ = 14 min, d = 15.531μm; (b) lower curve; $t - t_0$= 19 min, d = 15.388μm.

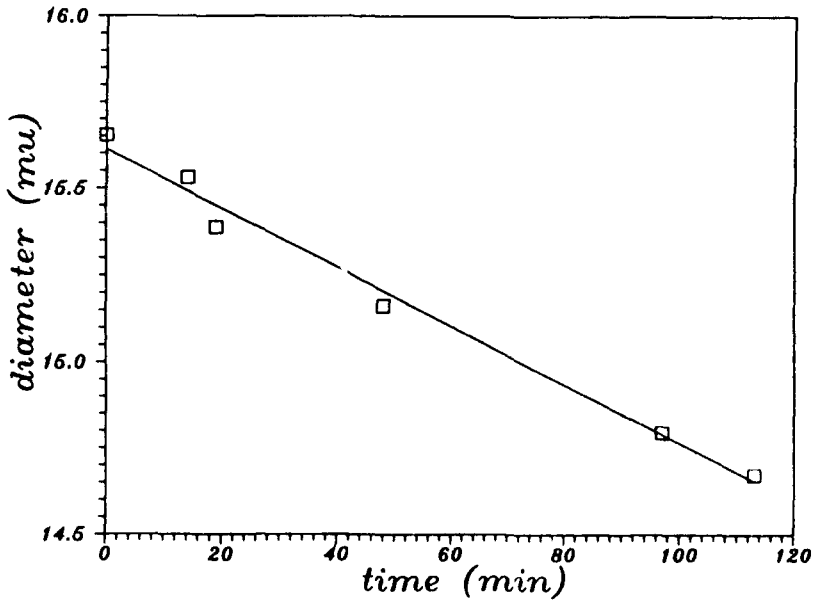

Figure 1c. Time dependence of best fit diameter of evaporating glycerol droplet.

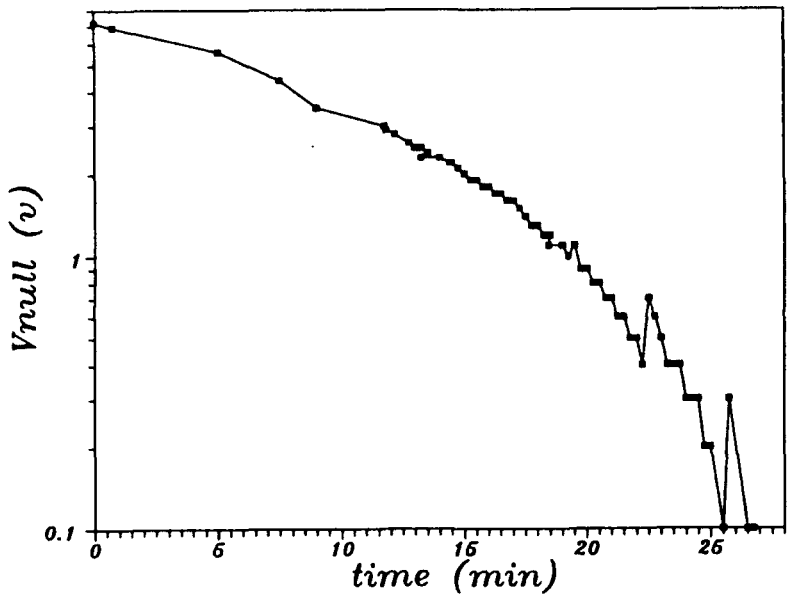

Figure 2a. Variation in null point voltage for evaporating dodecanol droplet.

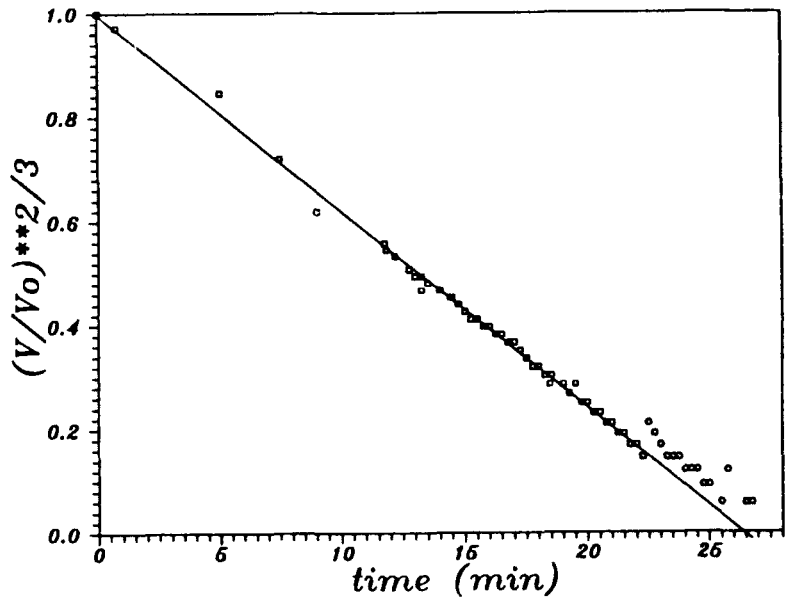

Figure 2b. "d^2-law" behavior of evaporating dodecanol droplet.

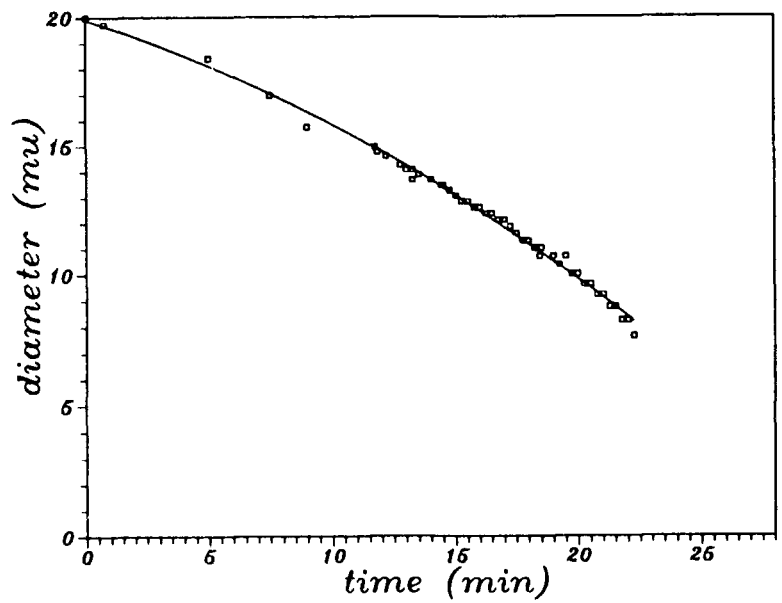

Figure 2c. Time dependence of dodecanol diameter based on null point voltage data.

APPENDIX A

Three dimensional internal droplet circulation induced by surface driven rotation

Joseph T. Hodges

National Institute of Standards and Technology, Gaithersburg Maryland 20899

Constantine M. Megaridis*, Jun Xin, Joseph M. Day

Department of Mechanical Engineering, The University of Illinois at Chicago, Chicago, Illinois 60607

and

Cary Presser

National Institute of Standards and Technology, Gaithersburg, Maryland 20899

Abstract

This paper presents a combined theoretical/experimental study of internal liquid circulation induced by droplet–surface rotation. A numerical model is presented first examining the fluid transport processes within a spherical liquid volume, whose surface is subjected to a steady rotation about its own axis. Planar laser-induced fluorescence is employed to provide high-resolution images of flow patterns developed within mm-size suspended droplets, that are exposed to steady, laminar, air streams to induce surface rotation. Very good agreement between experiment and theory is demonstrated. The motion established from surface rotation bears little resemblance to the toroidal internal flows developed within droplets under axisymmetric conditions. Consistent spiral flow patterns are revealed, suggesting that droplet rotation or spinning may be significant in practical situations involving droplet convective transport.

* Corresponding author

I. INTRODUCTION

Droplet phenomena are relevant to a wide variety of physical processes ranging from atmospheric transport of rain droplets, to liquid-fuel evaporation and combustion. Most of the above phenomena involve situations where the droplets have a relative translational velocity with respect to the surrounding gaseous medium. The shear interaction of the two phases across the gas/liquid interface frequently establishes droplet internal motion. In non-isothermal flows, droplet internal circulation can also be developed because of interfacial temperature gradients [1]. The fluid motion within liquid droplets is of great importance for practical applications involving droplet transport. For example, liquid circulation in a fuel droplet enhances both heat and mass transport, thus affecting the relevant evaporation and combustion rates. Internal circulation can also impact the drag force exerted by the host medium on the droplet, and in so doing, affect the bulk motion. It is therefore evident, that in order to enhance our current understanding of droplet-related processes, e.g., combustion [2]–[5], it is necessary to adequately characterize the droplet internal motion and determine its influence on liquid evaporation dynamics.

The fundamental mode of internal motion within a droplet was described a century ago by Hill [6]. It was then shown that a two dimensional axisymmetric vortex structure (known as Hill's vortex) can satisfy the equations of continuity and momentum within a spheroidal droplet. It was later postulated that such an internal flow could be induced by exposing a droplet to a steady laminar axisymmetric fluid flow. The basic hydrodynamics of the flow (both internal and external to a droplet) were solved by Hadamard [7] and Rybczinski [8]. These analyses considered creeping viscous flows past liquid spheres. Just after the middle of this century and spanning over twenty years, several investigators [9]–[15] visualized Hill's vortices in mm-sized droplets using a number of experimental configurations. These studies (which included both liquid and gaseous media) proved beyond doubt that toroidal internal

circulation can occur in droplets having a relative velocity with respect to the host medium. However, these measurements were generally too qualitative to provide sufficiently detailed data for model validation.

The effect of internal motion on rates of mass transport for small droplets was initially believed to be insignificant, although, it was predicted that (for a sufficiently high droplet Reynolds number) mass transfer coefficients of circulating droplets could be as much as two and a half time greater than those of quiescent droplets [16]. Indeed, the importance of internal circulation has become increasingly apparent with time. The aerodynamics of internal circulation in large, free falling, deformable, non-evaporating water droplets were initially addressed by McDonald [17]. LeClair et al. [18] used seed particles and streak photography to obtain data on the particle trajectories and estimate average liquid velocities inside droplets suspended in laminar airstreams. Since the flow patterns were visualized inside droplets that were highly loaded with seed particles, there was some ambiguity in the results regarding the unknown influence of such large populations of solid tracers on the induced liquid motion.

More recently, Winter and Melton [19] utilized oxygen quenching of laser-induced fluorescence from naphthalene to examine the significance of internal circulation within sub-millimeter hydrocarbon droplets at room temperature. The fluorescing droplets studied by Winter and Melton [19] were illuminated with a laser sheet and photographed. The spatial distribution of fluorescent intensity was dependent upon the local oxygen concentration and thus indirectly revealed patterns of internal circulation within the droplets. The authors stated that the liquid circulation may have been influenced (to a questionable degree) by the process of droplet injection. In that study, liquid-component vaporization was entirely suppressed due to the nature of the liquid compound (decane) used in that work and the room-temperature experimental conditions.

In a subsequent study [20], Winter used different droplet generation techniques to unambiguously determine the source of internal circulation of droplets falling a short distance in a chamber filled with a shear flow of nitrogen and a variable amount of oxygen. These measurements provided internal flow patterns that occasionally revealed signs of droplet spin. No direct comparisons with numerical models of internal circulation were made.

Another recent experimental study by Wong and Lin [21] provided indirect evidence of toroidal shear–induced circulation in the interior of large, hydrocarbon droplets that were exposed to high-temperature gaseous streams at atmospheric pressure. The JP-10 and decane droplets studied by Wong and Lin had an initial diameter of 2 mm, and were suspended using a thin shell-shaped probe specially designed to minimize interference to the internal liquid motion. It is important to note, however, that Wong and Lin [21] deduced results on internal droplet dynamics from transient internal temperature distributions.

The mechanism of internal liquid circulation has been included in several detailed droplet evaporation models that were developed over the past decade [22]–[26]. These models examined isolated droplets exposed to axisymmetric, laminar, convective flows, and predicted the occurrence of two dimensional toroidal internal circulation patterns –similar to Hill's vortices– at sufficiently high droplet Reynolds numbers. On the other hand, the comparatively slow development of quantitative diagnostic techniques has produced very little experimental data for validation of such models. At present, there exist only a few studies [27] that compare model predictions with transient, spatially-resolved experimental field measurements in well-defined droplet flow systems.

The objective of this investigation is to characterize a unique mode of droplet internal flow that –to the best of the authors' knowledge– has not yet been identified (even though its occurrence is highly probable in practical situations of interest where droplets are exposed to non-uniform flow streams). The internal flow examined in the current study is that induced

by a droplet–surface rotational motion, which can develop when a droplet encounters a non-uniform stream (shear flow, for example), or a locally rotating gaseous field (a turbulent eddy, for example, where a droplet is instantaneously located) or perhaps by the angular momentum imparted to a droplet during spray atomization. It should be noted, however, that the liquid motion examined herein is not equivalent to the rigid body droplet rotation (spinning) that was theoretically addressed by Lozinski and Matalon [1, 28], or the fiber–induced droplet rotation investigated by Pearlman and Sohrab [29].

First, a numerical model is presented to predict the internal flow developed when a uniform rotation is imposed upon the droplet surface. Subsequently, an experimental setup is described, featuring a flow configuration that has been specifically designed to induce a uniform droplet–surface rotation. Planar laser-induced fluorescence measurements are employed to provide high resolution images of the flow patterns developed within mm-sized pendant water droplets exposed to steady laminar air streams. The measurements of shear-induced droplet circulation are then combined with the predictions of the numerical model to produce a physical interpretation of the observed flow patterns.

II. NUMERICAL MODEL

In most spray combustion applications, the Reynolds number (based on droplet diameter, ambient properties, and relative velocity between liquid and gas) rarely exceeds 100 [4]. The corresponding Reynolds numbers of free-falling rain droplets may be slightly higher, especially for the largest droplets. In this context, droplet flows involving Reynolds numbers around 100 are appropriate for most practical situations of interest. Although the above flows are laminar, a detailed simulation of the domains within and around the droplet requires the solution of the full Navier-Stokes equations in both the liquid and gas phases, with appropriate boundary conditions at the gas/liquid interface.

The exposure of a solid sphere to a shear flow has been known to generate rotational mo-

tion with respect to its own axis. Eichhorn and Small [30] used a Poiseuille flow to levitate hydrodynamically mm-size spheres within an inclined glass tube. When flow Reynolds numbers ranged from 80 to 250, steady angular velocities up to 34 s^{-1} were consistently observed. Liquid droplets can also acquire an angular velocity around their own axis, as a result of atomizer design and/or turbulence vorticity. Observations of the smoky wake of burning n-pentane droplets have also been reported as evidence of droplet spinning [31]. Rigid body droplet rotation and its effect on droplet evaporation has been theoretically examined by Lozinski and Matalon [28] in the limit of small Reynolds and Marangoni numbers. No translational motion between droplet and ambient gas was considered in that study. Pearlman and Sohrab [29] used a rotating fiber to induce droplet angular velocities up to 40 rps for mm-size droplets suspended at the tip of the fiber. The droplet rotation in that configuration, however, was produced by the shear interaction between fiber and liquid, and was thus initiated from the droplet axis. When liquid droplets encounter a locally rotating or nonuniform ambient flow, it is naturally expected that the droplet surface will first be affected through shear interaction. The droplet interior will subsequently adjust to the kinematic conditions imposed on the droplet surface.

The current model examines the liquid flow within a spherical isothermal volume, whose surface is rotated at a uniform angular velocity ω. The model configuration is depicted in Fig. 1, and simulates a liquid droplet with a steady surface rotation around the z-axis passing through its center. Since the surface rotation is time independent, the resulting droplet internal motion eventually becomes time invariant. The appropriate spherical coordinate system (r, θ, φ) is shown in Fig. 1, along with the respective velocity components (u, v, w). This flow configuration suggests:

1: Symmetry with respect to the x-y plane. This implies that only half of the droplet volume (on either side of the x-y plane) needs to be modeled, and that the fluid motion in

the symmetry plane is two dimensional.

2: Symmetry with respect to the azimuthal coordinate φ about the z-axis. This condition simplifies the calculation considerably, since the droplet internal field need be determined only on a constant φ plane.

The aforementioned symmetries thus effectively reduce the computational domain to a quarter-circle. The following assumptions were also adopted in our analysis:

(1) no liquid vaporization occurs,

(2) gravitational effects can be neglected,

(3) fluid properties are constant.

Based on these assumptions, the nondimensional governing equations for a spherical coordinate system (Fig. 1) are given below. At steady state, the momentum equations are of elliptic character. Due to the increased numerical requirements of elliptic partial differential equations, the model equations include the time dependent (parabolic) term. This is done because the relevant time-marching technique has advantageous numerical stability and convergence properties. An additional advantage of the time-dependent features of the model is the ability to readily obtain characteristic time scales of the relevant flow patterns. The steady state solution is obtained after completion of a transient stage which is not of interest in the current study. In the following, ν denotes the kinematic viscosity of the liquid, ρ the liquid density, ω the angular velocity of the droplet surface, and R the droplet radius. The time has been normalized with respect to $1/\omega$, the velocities with respect to ωR, the radial coordinate with respect to R, and the pressure with respect to $\rho(\omega R)^2$.

Continuity equation

$$\frac{1}{r^2}\frac{\partial(r^2u)}{\partial r} + \frac{1}{rsin\theta}\frac{\partial}{\partial\theta}(vsin\theta) = 0 \qquad (1)$$

Radial Momentum Equation

$$\frac{\partial u}{\partial t} + u\frac{\partial u}{\partial r} + \frac{v}{r}\frac{\partial u}{\partial \theta} - \frac{w^2 + v^2}{r} = -\frac{\partial P}{\partial r}$$

$$+ \frac{\nu}{\omega R^2}\frac{1}{r^2}[\frac{\partial}{\partial r}(r^2\frac{\partial u}{\partial r}) + \frac{1}{sin\theta}\frac{\partial}{\partial \theta}(sin\theta\frac{\partial u}{\partial \theta}) - 2u - 2\frac{\partial v}{\partial \theta} - 2vcot\theta] \quad (2)$$

Polar Momentum Equation

$$\frac{\partial v}{\partial t} + u\frac{\partial v}{\partial r} + \frac{v}{r}\frac{\partial v}{\partial \theta} + \frac{1}{r}(uv - w^2cot\theta) = -\frac{1}{r}\frac{\partial P}{\partial \theta}$$

$$+ \frac{\nu}{\omega R^2}\frac{1}{r^2}[\frac{\partial}{\partial r}(r^2\frac{\partial v}{\partial r}) + \frac{1}{sin\theta}\frac{\partial}{\partial \theta}(sin\theta\frac{\partial v}{\partial \theta}) + 2\frac{\partial u}{\partial \theta} - \frac{v}{sin^2\theta}] \quad (3)$$

Azimuthal Momentum Equation

$$\frac{\partial w}{\partial t} + u\frac{\partial w}{\partial r} + \frac{v}{r}\frac{\partial w}{\partial \theta} + \frac{uw + vwcot\theta}{r} = \frac{\nu}{\omega R^2}\frac{1}{r^2}[\frac{\partial}{\partial r}(r^2\frac{\partial w}{\partial r}) + \frac{1}{sin\theta}\frac{\partial}{\partial \theta}(sin\theta\frac{\partial w}{\partial \theta}) - \frac{w}{sin^2\theta}] \quad (4)$$

Initial and Boundary Conditions

The liquid droplet is assumed to be initially quiescent ($u = v = w$=0). In addition, the pressure in the droplet interior is initially uniform (atmospheric plus surface tension pressure).

The droplet–surface boundary conditions were formulated to reflect a uniform rotation (angular velocity ω) around the z-axis. The non-dimensional form of these conditions is

$$= sin\theta \; ; \quad r = 1, \; 0 \leq \theta \leq \frac{\pi}{2} \quad (5)$$

$$u = 0 = \frac{\partial v}{\partial r} = \frac{\partial p}{\partial r} \; ; \quad r = 1, \; 0 < \theta < \frac{\pi}{2} \quad (6)$$

$$\frac{\partial u}{\partial \theta} = 0 = v = \frac{\partial p}{\partial \theta} \; ; \quad \theta = 0 \quad (7)$$

$$\frac{\partial u}{\partial \theta} = \frac{\partial w}{\partial \theta} = 0 = v = \frac{\partial p}{\partial \theta} \; ; \quad \theta = \pi/2 \quad (8)$$

Note that the conditions for v allow for a non-zero value of this velocity component on the droplet surface.

Numerical Solution Procedure

The solution procedure was implemented using the methods given in references [32, 33]. The system of governing equations was discretized spatially on a staggered mesh. Central finite differencing was employed for the diffusion terms, while upwind differentiation was employed for the convection terms. The time-splitting algorithm [33] was employed for temporal discretization. This technique expresses the radial and polar momentum equations as

$$\frac{\partial u}{\partial t} = -\frac{\partial P}{\partial r} + F_r(\vec{V}) \tag{9}$$

$$\frac{\partial v}{\partial t} = -\frac{1}{r}\frac{\partial P}{\partial \theta} + F_\theta(\vec{V}) \tag{10}$$

where $\vec{V}$ denotes the velocity vector, and F_r, F_θ represent all convective and viscous terms of the corresponding momentum equation. A first-order difference for the time derivative is used to advance the solution from the current step n to an intermediate level (superscript T)

$$\frac{u^T - u^n}{\Delta t} = -\frac{\partial P^n}{\partial r} + F_r^n(\vec{V}) \tag{11}$$

$$\frac{v^T - v^n}{\Delta t} = -\frac{1}{r}\frac{\partial P^n}{\partial \theta} + F_\theta^n(\vec{V}) \tag{12}$$

The intermediate–level velocity values must be corrected so that the pressure field and velocity field at the next time step $(n+1)$ satisfy the momentum and continuity equations, simultaneously. At that level, the discretized momentum and continuity equations are

$$\frac{u^{n+1} - u^n}{\Delta t} = -\frac{\partial P^{n+1}}{\partial r} + F_r^n(\vec{V}) \tag{13}$$

$$\frac{v^{n+1} - v^n}{\Delta t} = -\frac{1}{r}\frac{\partial P^{n+1}}{\partial \theta} + F_\theta^n(\vec{V}) \tag{14}$$

$$\frac{1}{r^2}\frac{\partial}{\partial r}(r^2 u^{n+1}) + \frac{1}{r sin\theta}\frac{\partial}{\partial \theta}(v^{n+1} sin\theta) = 0 \tag{15}$$

Combining the above equations we obtain

$$\frac{u^{n+1} - u^T}{\Delta t} = -\frac{\partial P^{n+1}}{\partial r} + \frac{\partial P^n}{\partial r} \tag{16}$$

$$\frac{v^{n+1} - v^T}{\Delta t} = -\frac{1}{r}\frac{\partial P^{n+1}}{\partial \theta} + \frac{1}{r}\frac{\partial P^n}{\partial \theta} \tag{17}$$

When equations (16) and (17) are substituted into Eq. (15), we obtain an expression used to update the pressure field

$$\nabla^2 P^{n+1} - \nabla^2 P^n = \frac{1}{\Delta t}[\frac{\partial}{\partial r}(r^2 u^T) + \frac{r}{sin\theta}\frac{\partial}{\partial \theta}(v^T sin\theta)] \tag{18}$$

The numerical solution procedure can thus be summarized by these steps: (i) Eqs. (11) and (12) are used to calculate u^T, v^T, respectively. (ii) Eq. (18) is employed to calculate P^{n+1}. This is a Poisson equation and is solved using the successive over-relaxation (SOR) method. (iii) The velocities u^{n+1}, v^{n+1} are corrected using Eqs. (16) and (17). (iv) Finally, since the azimuthal component of the momentum equation is independent of the pressure field, the corresponding velocity w^{n+1} is directly calculated from Eq. (4). The above steps describe one complete computational cycle. This procedure is advanced in time and repeated until steady state is reached. Finally, the three dimensional character of the fluid flow is reconstructed by effectively rotating the computational quarter-circle domain around the z-axis by 360°.

III. MODEL PREDICTIONS

The model was first employed to investigate the motion induced in the interior of a 2mm–diameter water droplet whose surface is rotated around the z-axis at a steady frequency f_s=3 Hz. Both droplet size and surface rotation frequency were selected to be relevant to the experimental measurements presented below. Initially, the sensitivity of the model

predictions to both the time-step and numerical grid were examined. A grid of 12 (along r) $\times$ 20 (along θ) nodes along with a nondimensional time step of 10^{-4} proved to be adequate for both time-step and grid independent results. Steady state was reached after approximately 2×10^4 time steps ($\sim$1 s). The computations were performed on a DEC 5000PXG workstation and a Cray Y-MP supercomputer; a typical run required approximately 4 CPU hours on the DECstation, or 2 CPU minutes on the Cray Y-MP.

Figure 2 presents a typical trajectory of a flow–tracing element that is periodically transported in the vicinity of the droplet surface. The time required for the completion of this trajectory is approximately 6 s. The entire path lies on the same side of the x-y plane, and has a complex three dimensional character. It is seen that, although the imposed surface motion is rotational with respect to the z-axis, a secondary motion develops as a result of the spherical shape of the droplet. As shown in Fig. 2, the fluid particle follows a spiraling motion away from the pole of the axis of rotation, while simultaneously moving closer to the equatorial (x-y) plane of symmetry with an almost constant value of radial distance from the droplet center (r $\sim$0.9 for the path shown). After approaching the x-y plane, the fluid spirals inward from the equator to the droplet center, subsequently turns and finally winds around the z-axis until it reaches its original position near the droplet surface. The same trajectory is repeated thereafter. The particle movement (from the pole to the equatorial plane) results from the centrifugal force which tends to drive the particle away from the axis of rotation and hence in the direction of increasing polar angle. It should be noted that the trajectory shown in Fig. 2 is very different from typical trajectories within droplets exposed to axisymmetric flows. Therefore, it is apparent that the characteristic length scales of fluid transport in the interior of droplets whose surface is uniformly rotated, are different than those established in toroidal recirculation flows within droplets.

Figures 3A and 3B, produced by the numerical model, represent characteristic project-

ed views of the complex three dimensional field within the droplet. Figure 3A presents a flow-tracing particle path within the symmetry (x-y) plane shown in Fig. 1. This trajectory indicates that the fluid is convected in a spiral fashion towards the droplet center, before it turns away from the x-y plane in a direction parallel to the axis of rotation (Fig. 2). Figure 3B presents the streamlines (upper half) and velocity vectors (lower half) of the droplet secondary motion on a constant-φ plane, as attributed only to the radial (u) and polar (v) components of the liquid velocity field. The composite internal motion consists of the well-defined double toroidal circulation shown in this figure, superimposed on the rotational component around the z-axis. The remarkable similarity between the toroidal flow pattern shown in Fig. 3B and that depicted in Fig. 4 of ref. [1] is worth noting. However, the internal motion in the current study is induced by a uniform rotation of the droplet surface. On the contrary, the qualitatively similar motion reported by Lozinski and Matalon [1] is due to thermocapillary forces established on the non-isothermal surface of a droplet rotated in a rigid-body fashion.

IV. FLOW VISUALIZATION EXPERIMENTS

The experimental apparatus described below, features water droplets suspended on a vertical, flat-tipped hypodermic needle. As depicted in the schematic of Fig. 4, the droplet surface was observed to rotate at a steady angular velocity $\omega = \frac{d\varphi}{dt}$ with respect to the z-axis (Fig. 1), after exposure to a uniform gas stream directed perpendicular to the needle/droplet vertical axis. The droplet surface rotation is attributed to the presence of the needle at the top of the droplet. The needle obstructs the gaseous flow in its vicinity. Consequently, there is relatively little momentum exchange between air and liquid near the top of the pendant droplet. In addition, there exist attractive capillary forces at the liquid-needle interface which oppose fluid flow. Thus, the shear differential between the upper and lower portions

of the droplet, as well as the "pinning" of the droplet at the liquid-needle interface, combine to maintain the experimentally observed surface rotational pattern (Fig. 4). It should be noted that all experiments were performed at room temperature, therefore, the rate of liquid evaporation was low and fluid properties were essentially constant. The droplet surface regression was intentionally suppressed, to assure that the shear-induced liquid flow was not affected by the evaporative mechanisms.

A schematic of the experimental setup is presented in Fig. 5. The droplet–suspending needle was mounted on a three-axis translation stage with a positioning accuracy of 2 μm. A steady flow of air was generated through a laminar flow device from which the gas flowed out horizontally (see Fig. 5). The laminar flow device proved to be a critical component of the experimental setup, since steady reproducible flows were necessary for adequate levels of repeatability. Metered air entered a cylindrical glass enclosure via a 5 mm i.d. tube which gradually tapered to an inside diameter of 33 mm. The entrance chamber of the device was followed by a porous plug, then a packed bed of 1 mm glass beads, a fine screen, a ceramic honeycomb with a cell density of 0.5 cell/mm^2, and finally a fine nylon mesh. The air flow to the device was regulated with a calibrated rotameter. Typical gas velocities employed were approximately 1 m/s. A hot-wire anemometer was used to determine the uniformity of the air stream. The air velocities were measured with a grid spacing of the order of 4 mm. The velocity data indicated a temporally quiet flow with spatial uniformity well within 10 % over the stream cross section.

The droplet was observed in real time through a high–magnification microscope. Distilled water droplets of 2 mm in diameter were placed at the flat tip of the vertically-oriented 10 μl syringe (dimensions: 0.7 mm–o.d. , 0.1 mm–i.d.) and subsequently exposed to a steady air stream emanating from the laminar flow device. The flow device was oriented perpendicular to the syringe needle so that the resulting cross flow caused the droplet surface to rotate

in the manner depicted in Fig. 4. A steady motion was established within a few seconds after exposure of the initially quiescent pendant droplet to the gaseous stream. The flow Reynolds numbers –based on droplet diameter, and free-stream velocity and properties– were in the range from 100 to 130. Although suspended from the needle, the droplets were nearly spherical (with typical aspect ratios of about 0.9).

The droplet internal convective motion was visualized via planar, laser–induced fluorescence. Fluorescence signals were induced by laser excitation of a small mass of dilute aqueous laser dye solution (1E-6M Rhodamine B/H_2O) that was occasionally introduced at the top of the suspended droplet by slightly depressing the syringe plunger. The addition of dye was estimated to alter the droplet mass by less than 1 % at a time, so that the impact of dye injection on the internal droplet dynamics was minimal. Observation of dye-doped droplets without the external gas cross flow indicated that molecular diffusion of the dye under quiescent liquid conditions was negligibly slow.

Each droplet was illuminated by a thin laser sheet passing through its midplane at three mutually orthogonal orientations (see planes A, B and C in Fig. 6). Note that plane A coincides with the equatorial (x-y) plane of the droplet. The internal motion was visualized from three respectively perpendicular directions (views or perspectives A, B, and C; Fig. 6). The fluorescent emission from the dye was used to follow the liquid-phase circulation and was recorded with a high spatial-resolution microscope and CCD camera/video recording system (see Fig. 5).

A continuous wave argon ion laser ope ..ted at a wavelength λ=514.5 nm was used to excite the dye fluorescence. The laser sheet was produced by a set of spherical and cylindrical lenses preceding the droplet. In order to ensure that the beam width was sufficiently small, the intensity profile of the laser sheet (along its minor axis) was measured with a CCD camera/frame grabber system. This measurement gave a $1/e^2$ full sheet thickness of the

order of 100 μm. The sheet thickness was maintained over a longitudinal range of 3 mm. The receiving optics included an f/2.8 dual port long-distance microscope coupled to a black and white CCD video camera. A long-pass filter (with a cut–off at 530 nm) was placed in front of the microscope objective to suppress elastically scattered laser light from the droplet and needle. With a 5×-microscope objective placed 100 mm from the droplet, the linear magnification of the microscope was approximately 1.6:1 to yield a horizontal spatial resolution of 10.5 μm/pixel. For real-time data observation and storage, the video output of the camera was connected to a video monitor and recorded with a videocassette recorder. Once the events were recorded, individual frames of the videotape were digitized using a frame grabber/386 computer system. This digitization gave 8 bit gray level images with dimensions of 512 columns by 480 lines.

Real-time observations performed on a series of water droplets showed distinct patterns of internal circulation throughout the range of Reynolds numbers examined. Since the water droplets vaporized with time (within several minutes), the Reynolds number gradually decreased as a result of droplet size reduction. Our observations focused primarily on the early stages of droplet lifetime during which the effect of the suspending needle was expected to be less important.

V. FLOW VISUALIZATION RESULTS

The internal motion of a series of pendant water droplets was observed using the fluorescence patterns which traced the liquid flow for several seconds after each dye injection event. As the dye was convected through the liquid medium, the fluorescence signal decayed due to dilution effects. The occasional transport of microscopic fluorescing tracer particles on the droplet surface provided an excellent means for following the liquid surface motion in real time. The steady surface rotation depicted in Fig. 4 revealed a very repeatable pattern, particularly from perspective B of Fig. 6. The angular frequency of this motion was measured

with a timing device to be approximately 3 Hz, with a corresponding rotational Reynolds number around 0.2. This quantity, based on rotation velocity, droplet size, and free-stream properties, is frequently employed to characterize the intensity of rotation [28].

The droplet internal circulation was observed at different perspectives (A, B or C of Fig. 6), one viewing angle at a time. The consistency and reproducibility of the flow patterns were of primary concern. Reproducibility was needed to ensure that an accurate picture of the internal circulation was obtained by the nonsimultaneous observation of different sections of the droplets. It was found that the induced liquid motion was sensitive to the relative orientation of the suspended droplet with respect to the incoming air stream. This point was emphasized by the highly unstructured internal fluid motion obtained when the ambient flow was intentionally positioned at nonorthogonal angles with respect to the axis of the suspended droplet. Conversely, with the droplet axis orthogonal to the air stream, the patterns observed for the shear-induced liquid flow showed excellent reproducibility over a series of tracing injections.

Three sequences of images are presented in Fig. 7 for 2-mm droplets that were exposed to a uniform air stream of velocity 1 m/s and room temperature. The Reynolds number was 130, based on droplet diameter and free stream properties. The three sequences correspond to the different perspectives (A, B and C) illustrated in Fig. 6. Note that each set displayed in Fig. 7 corresponds to a unique injection event. Sequence 7A presents a typical temporal variation of the fluorescence signal as observed from perspective A of Fig. 6 In Fig. 7A, the gaseous flow is directed from right to left and the needle is positioned at top of the droplet. The laser sheet was oriented vertically and passed through the droplet center in the direction of the ambient flow (x-y plane). The suspending needle is barely visible at the top of the droplet. Some background scattering from the laser sheet and the needle is indicated by two thin bright sections of the droplet surface located at either side of the needle

near the top of the droplet. The images of Fig. 7A reveal a spiral internal motion in that plane, in the clockwise direction, with a characteristic frequency that gradually increases as the dye approaches the center of the droplet. The timewise weakening of the intensity of the fluorescence signal, as shown in Fig. 7A, was attributed to the gradual convection of dye away from the imaging (x-y) plane. Note that, in principle, the motion of the fluid located within the x-y plane should (by symmetry) be confined to that plane. Although the fluorescence signal did decay as the tracer dye continued to move towards the droplet center, a significant amount of dye remained on the slicing plane toward the end of the spiral. This suggests that the observed motion was nearly planar for perspective A and that the laser sheet passed through the droplet center. The excellent agreement between the flow-tracing path of Fig. 7A and the model-predicted trajectory shown in Fig. 3A suggests that the model captures a main feature of the droplet internal flow.

The complex three dimensional particle trajectory predicted by the model in Fig. 2 was also corroborated by the experimental observations. Specifically, in a video film obtained from perspective B (x-z plane), one can follow a tracing particle as it propagates along the droplet surface (alternately moving in and out of the laser sheet). This particle begins near the pole and moves along the droplet surface toward the equator whereupon it penetrates into the equatorial plane. In accord with Fig. 2, the particle remains in this plane as it can be seen to spiral inward toward the rotational axis. Once near the droplet center, the particle follows a helical path in the droplet interior moving back toward the original pole and finally reappearing at the droplet surface. The rather striking similarity between the numerical prediction and observations thus provides further support for the validity of the model and the existence of such three dimensional trajectories as the one depicted in Fig. 2.

Figure 7B shows the temporal variation of the fluorescence signal during an injection event as observed from perspective B (see Fig. 6). The air flow in that series is normal

to the laser sheet which coincides with the x-z plane of observation. The spiral motion displayed in Fig. 7A was exhibited by a sequential flashing (in a temporal sense) of the fluorescent islands shown in the early frames of sequence 7B. As evidence of data consistency, we note that the characteristic frequency of the flashing events matched that of the spiral motion in perspective A. The planar images of Fig. 7B appear nearly symmetric with respect to the vertical x-axis through the droplet center. The presence of the needle at the top of the droplet resulted in some minor asymmetry with respect to the horizontal axis (see intermediate frames of Fig. 7B). Nevertheless, the overall dependence of the internal flow on the azimuthal coordinate φ appears to be minimal. The transport of dye reveals significant convective motion towards the droplet center and away from the vertical x-y plane that divides the liquid in the direction of the air flow. The quad-cell flow pattern clearly marked in the last frame of Fig. 7B, is consistent with the earlier tracer motion depicted in this sequence. This pattern also agrees well with the motion predicted by the model (Fig. 3B), thus confirming the numerical predictions. Finally, the characteristic time for diffusion of the dye on plane B, was at least an order of magnitude longer than that of the helical motion on plane A.

Figure 7C shows the temporal variation of the fluorescence signal during injection as observed from the bottom of the droplet; perspective C of Fig. 6. The air flow in that series was directed from top to bottom. The laser sheet was oriented horizontally and passed through the droplet center. The similarity between the flow patterns of Figs. 7B and 7C also suggests that the overall dependence of the internal flow on the azimuthal coordinate φ appears to be minimal. The close similarity between the observed flow in planes B and C thus validates one of the major assumptions of the model.

The data presented in Fig. 7 were obtained by imaging the dye fluorescence as seen through a hemisphere of transparent liquid. In interpreting these data, one must therefore

bear in mind the following spatial effects created by light refraction. First, the incident sheet beam is refracted upon entering the droplet, causing the beam to converge. Consequently, the local intensity of the sheet beam increases in the direction of propagation. Second, the fraction of all emitted photons which cross the droplet/air interface and reach the camera sensor (quantum collection efficiency) varies with position. This efficiency depends on the refractive index of the liquid as well as the f/# of the receiving optics.

A third consequence of light refraction is the geometric distortion that occurs when imaging an object located within a droplet. The liquid hemisphere acts like a lens with variable magnification. As a result, images are "stretched" radially outward [34]. Kintner and coworkers [11] [12] [35] derived an expression for such geometrical distortion of an object point in the midplane of an ellipsoidal droplet. They determined the apparent origin of a light ray which leaves the object point positioned at the midplane of the droplet and propagates parallel to the optical axis. The angular deflection of this ray, occurring at the droplet/air interface, was calculated by principles of geometrical optics. By symmetry, the geometrical distortion for a spherical droplet is only dependent on the radial position. Assuming a relative refractive index of 1.3334 (water droplet to air), a mathematical formula [35] was used to calculate the radial coordinate of an image point vs. its conjugate radial object point (see Fig. 8A). The dashed curve corresponds to the apparent position, while the solid line represents the position under zero distortion. It is noted that for this refractive index ratio, the image appears to be further out than the actual object point in the radial direction. The radial stretch factor is nearly constant (~30%) for object coordinates up to 60 % of the droplet radius. At larger radial coordinates, the distortion starts to decrease until the edge of the droplet where no distortion occurs. Figure 8B is an illustration of the geometrical distortion of a spiral (solid line) and its conjugate image (dashed line) based on the same refractive index ratio as Fig. 8A. In comparison to Fig. 7A, we deduce that image restora-

tion would only alter the length scales with no significant effects on the overall liquid flow behavior. Nor would there be any effect on the measured time scale of the observed spiral period (as seen in plane A), since there is no distortion at the edge and center of the droplet.

V. DISCUSSION

The predicted fluid trajectory in the droplet interior shown in Fig. 2 is consistent with the experimental observations, which suggest that tracing particles introduced near the top of the droplet undergo a spiral motion as they translate toward the center, and are subsequently convected away from the x-y plane of symmetry. The physical presence of the suspending needle at top of the droplet (Fig. 4), however, suggests a model formulation that accounts for variation of the liquid velocities along the azimuthal (φ) direction. Our experimental observations consistently indicated that the magnitude of the azimuthal velocity component (w) was substantially larger than the magnitudes of the radial (u) and polar (v) velocity components (Fig. 1). Therefore, the region most influenced by the needle consists of a strip of fluid which is moving on the droplet surface between two parallel vertical planes (P1, P2), as shown in Fig. 1. The distance between these two planes is of the order of the needle diameter. The fluid particles moving on the droplet surface and within the droplet strip in question are decelerated by the needle (no slip condition). From that perspective, the azimuthal velocity component, w, on the droplet surface is expected to be lowest in the immediate vicinity of the needle and highest near the lowest portions of the suspended droplet. Given this physical picture, the w velocity component must be φ dependent. Such a situation would require a three dimensional modeling domain. However, the experimental observations clearly indicated that any azimuthal asymmetry induced by the needle is rather minimal. Therefore, the relevant model assumption regarding symmetry along φ is well justified.

The effect of the needle on the droplet internal motion was examined using the numerical model. As a reasonable first-step approximation of the actual behavior, the needle-induced deceleration was accounted for by assuming an averaged effect throughout the zone of influence. To this end, the liquid retardation effect of the needle was assumed to be localized on the droplet surface between planes P1 and P2 of Fig. 1. The retardation was assumed to be uniform along φ. The flow retardation between planes P1 and P2 was imposed numerically by slowing down the surface rotation in this region by a specific percentage, represented by a variable c. Thus, the surface azimuthal velocity component between P1 and P2 was taken as $w = c\omega R sin\theta$; The value c=0 corresponded to no motion at all, while the value c=1 reflected unrestricted rotation. In reality, the retardation constant c would be zero in the immediate vicinity of the needle and non-zero for other regions. Constant "average" values of c between 0 and 1 were used in a series of simulations. This approach preserved the azimuthal symmetry, yet allowed the retarding effect of the needle to be taken into account. It was found that the value of c did not influence the overall appearance of the internal flow (Fig. 2), even though it did affect the relative ratios between characteristic transport times and lengths. A value of c=0.8 was found to provide the best agreement between characteristic transport times measured experimentally, and those calculated by the model.

The excellent agreement between model predictions and flow visualization regarding the character of the induced flow, suggests that the numerical model may be used to elucidate further the steady liquid motion established by a uniform surface rotation. The predicted motion induced in the interior of a 2mm–diameter water droplet with a steady surface rotation around the z-axis (frequency f_s=3 Hz) was examined further. Figure 9 presents the variation of the dimensionless azimuthal velocity component w along a radius positioned at θ=52.5°. The values of the predicted velocity w, drawn by the solid curve, are compared to those corresponding to a rigid–body rotation with the same frequency f_s =3 Hz (dashed line).

The deviation of the two curves is more pronounced away from the surface of the droplet, thus suggesting that the surface–driven motion studied herein differs from the rigid–body rotation considered in other studies. Figure 9 also presents the radial variation of the time period required for a fluid element to complete its closed trajectory. The specific curve shown in this figure corresponds to θ=52.5°, and indicates that the fluid particles transported through the core of the toroidal vortices shown in Fig. 3B take significantly shorter periods to close their trajectories. Furthermore, the circulation period of the fluid elements near the droplet center is substantially longer. This trend is anticipated, since the liquid flow is surface driven.

Figure 10 presents the predicted variation of the polar velocity component v on the droplet surface vs. θ, for several values of the imposed boundary rotation frequency f_s. Since the velocities shown in Fig. 10 are normalized with respect to ωR, they essentially represent the ratio of polar (on the droplet surface) to azimuthal velocity (in the equatorial plane). It is apparent that the polar component induced by the imposed azimuthal surface rotation is very weak at low rotation frequencies. However, higher frequencies result in substantially enhanced values of v; see f_s = 10 Hz curve. It is also worth noting that for each curve, there exists a peak which shifts to lower values of θ with increasing rotational frequency f_s.

The above analysis and flow visualization experiments provide information on fluid transport processes within droplets that encounter non-uniform flows. This information is of practical importance, in the sense of its implications regarding the mixing efficiency and segregation of components in multicomponent droplets, energy transport rates, etc. The results indicate that the spiral liquid motion observed in rotating droplets reduces the characteristic lengths of the mixing processes by approximately a factor of two (compare the double toroidal pattern shown in Fig. 3B, with the single toroidal Hill's vortex established in axisymmetric configurations). Since the characteristic times for mass diffusion and energy transport are inversely proportional to the square of the above characteristic length,

it is concluded that processes involving droplet spinning may exhibit substantially reduced mixing times.

The fluid motion examined in the current study is qualitatively similar to that reported by Lozinski and Matalon [1], even though the origin of the induced motion is fundamentally different for the two investigations (surface rotation vs. thermocapillary forces). It would be useful to quantitatively compare the internal circulation induced by variable surface tension [1], with the motion established due to droplet–surface rotation. Lozinski and Matalon's analysis [1] is applicable in the limit of small values of the parameter $\Omega = R^2\omega/\alpha << 1$, where α is the gaseous thermal diffusivity. The parameter Ω represents the ratio of the droplet rotational velocity to the gaseous diffusion velocity. Due to the room temperature conditions employed in the current study, Ω is of the order of unity, thus making a direct comparison not possible.

VI. CONCLUSIONS

This paper presented a combined theoretical/experimental study of internal liquid circulation induced by a rotational motion of the droplet surface. Such conditions are expected to arise in actual processes when a shear or locally rotating flow imposes a spinning motion to the droplet interface. The rotational frequencies considered were of the order of several Hz, and correspond to low values of rotational Reynolds numbers. A numerical model was formulated first to quantify the fluid transport processes within a droplet whose surface is subjected to a steady rotation about its own axis. Planar laser-induced fluorescence techniques were employed to provide high-resolution images of flow patterns developed within mm-sized pendant droplets. These droplets were exposed to steady, laminar, air streams at room temperature and atmospheric pressure. When the ambient flow was directed perpendicular to the needle/droplet axis, the droplet surface was observed to rotate at a steady

angular velocity. The experimentally observed flow patterns showed excellent agreement with those predicted by the numerical model.

The study consistently revealed helical (spiral) three dimensional circulation patterns that bear little resemblance to the widely–studied two dimensional toroidal internal flows established within droplets under axisymmetric conditions. The rotation of the liquid interface around the droplet axis induced a secondary fluid motion, directed inward from the equator, and outward to the poles. This pattern of internal flow is qualitatively similar to that induced by droplet interfacial temperature gradients, as reported by other investigators [1]. The steady liquid motion along the azimuthal coordinate resembled a rigid–body rotation only at the outer layers of the droplet, while it lagged substantially in the core of the droplet. The results showed that processes involving shear–induced droplet rotation may exhibit substantially enhanced liquid mixing rates, thus suggesting that droplet spinning may be very important in practical situations involving droplet convective transport.

ACKNOWLEDGMENTS

Useful discussions with Dr. Hratch Semerjian of NIST are acknowledged with appreciation. This work was sponsored in part by the Air Force Office of Scientific Research, Air Force Systems Command, USAF, under grant number AFOSR 92-J-0476. The US Government is authorized to reproduce and distribute reprints for Governmental purposes notwithstanding any copyright notation thereon. The support of the NIST Scientific Computing Facility through an allocation of computer time on the Cray Y-MP is also acknowledged.

References

[1] D. Lozinski and M. Matalon, "Thermocapillary motion in a spinning vaporizing droplet," Phys. Fluids A **5**, 1596 (1993).

[2] C. K. Law, "Recent advances in droplet vaporization and combustion," Prog. Energy Combust. Sci. **8**, 171 (1982).

[3] G. M. Faeth, "Evaporation and combustion of sprays," Prog. Energy Combust. Sci. **9**, 1 (1983).

[4] W. A. Sirignano, "Fuel droplet vaporization and spray combustion theory," Prog. Energy Combust. Sci. **9**, 291 (1983).

[5] H. A. Dwyer, "Calculations of droplet dynamics in high temperature environments," Prog. Energy Combust. Sci. **15**, 131 (1989).

[6] M. J. M. Hill, "On a spherical vortex," Phil. Trans. Roy. Soc. **185**, 213 (1894).

[7] J. Hadamard, "Mouvement permanent lent d'une sphere liquide et visquese dan un liquid viscqueux," Com. Ren. de Sci. de l'Acad. de Sci. **152**, 1735 (1911).

[8] W. Rybczinski, Bull. Acad. Sci., Cracovie, Ser. A, 40 (1911).

[9] K. E. Spells, Proc. Phys. Soc. (London) **B65**, 541 (1952).

[10] F. H. Garner, A. H. P. Skelland and P. J. Haycock, "Speed of circulation in droplets," Nature **173**, 1239 (1954).

[11] R. C. Kintner, T.J. Horton, R. E. Graumann and S. Amberkar, "Photography in bubble and drop research," Can. J. Chem. Eng. **39**, 235 (1961).

[12] T. J. Horton, T. R. Fritsch and R. C. Kintner, "Experimental determination of circulation velocities inside drops," Can. J. Chem. Eng. **43**, 143 (1965).

[13] H. R. Pruppacher and K. V. Beard, "A wind tunnel investigation of the internal circulation and shape of water droplets falling at terminal velocity in air," Quar. J. Met. Soc. **96**, 247 (1970).

[14] S. K. Dayal, B. C. Srivastava and N. K. Srivastava, "Circulation patterns in charged and uncharged drops," Indian J. Pure Appl. Phys. **9**, 195 (1971).

[15] B. S. Sarma and P. K. Mondal, "Spatial filtering techniques applied to internal flow visualization," Indian J. Pure Appl. Phys. **13**, 97 (1975).

[16] P. Harriott, "A review of mass transfer to interfaces," Can. J. Chem. Eng. **40**, 60 (1962).

[17] J. E. McDonald, "The shape and aerodynamics of large raindrops," J. Meteor. **11**, 478 (1954).

[18] B. P. LeClair, A. E. Hamielec, H. R. Pruppacher and W. D. Hall, "A theoretical and experimental study of the internal circulation in water drops falling at terminal velocity in air," Journal of the Atmospheric Sciences **29**, 728 (1972).

[19] M. Winter and L. A. Melton, "Measurement of internal circulation in droplets using laser-induced fluorescence," Applied Optics **29**, 4574 (1990).

[20] M. Winter, "Droplet slicing measurements of internal circulation," Paper 93-0900, 31st Aerospace Sciences Meeting, Reno, Nevada, January 1993.

[21] S.-C. Wong and A.-C. Lin, "Internal temperature distributions of droplets vaporizing in high-temperature convective flows," J. Fluid Mech. **237**, 671 (1992).

[22] S. Prakash and W. A. Sirignano, "Theory of convective droplet vaporization with unsteady heat transfer in the circulating liquid phase," Int. J. Heat Mass Transfer **23**, 253 (1980).

[23] M. Renksizbulut and R. J. Haywood, "Transient droplet evaporation with variable properties and internal circulation at intermediate Reynolds numbers," Int. J. Multiphase Flow **14**, 189 (1988).

[24] R. J. Haywood, R. Nafziger and M. Renksizbulut, "A detailed examination of gas and liquid phase transient processes in convective droplet evaporation," Journal of Heat Transfer **111**, 495 (1989).

[25] C. N. Yung, K. J. De Witt, J. L. Brockwell and A. T. Chai, "The transient motion of a spherical fluid droplet," Chem. Eng. Comm. **110**, 163 (1991).

[26] C. H. Chiang, M. S. Raju and W. A. Sirignano, "Numerical analysis of convecting, vaporizing fuel droplet with variable properties," Int. J. Heat Mass Transfer **35**, 1307 (1992).

[27] C. M. Megaridis, "Comparison between experimental measurements and numerical predictions of internal temperature distributions of a droplet vaporizing under high-temperature convective conditions," Comb. Flame **93**, 287 (1993).

[28] D. Lozinski and M. Matalon, "Vaporization of a spinning fuel droplet," Proceedings of the Twenty-Fourth Symposium (Intl.) on Combustion, The Combustion Institute, pp. 1483-1491 (1992).

[29] H. G. Pearlman and S. H. Sohrab, "The role of droplet rotation in turbulent spray combustion modeling," Combust. Sci. Tech. **76**, 321 (1991).

[30] R. Eichhorn and S. Small, "Experiments on the lift and drag of spheres suspended in a Poiseuille flow," J. Fluid Mech." **20**, 513 (1964).

[31] R. Natarajan, "Some experimental observations of rotation, oscillation, spinning and swerving of falling burning drops," Can. J. Chem. Eng. **52**, 834 (1974).

[32] J. H. Ferziger, "Large eddy numerical simulations of turbulent flows," AIAA J. **15**, 1261 (1977).

[33] J. K. Dukowicz, "A particle-fluid numerical model for liquid sprays," J. Comp. Physics **35**, 229 (1980).

[34] D. S. Benincasa, P. W. Barber, J.-Z. Zhang, W.-F. Hsieh and R. K. Chang, "Spatial distribution of the internal and near-field intensities of large cylindrical and spherical scatterers," Applied Optics **26**, 1348 (1987).

[35] R. C. Kintner, "Drop phenomena affecting liquid extraction," Adv. Chem. Eng. **4**, 51 (1973).

FIGURE CAPTIONS

Fig. 1 Droplet model configuration along with the relevant spherical coordinate system (r, θ, φ), and the respective velocity components (u, v, w).

Fig. 2 Typical trajectory of a flow–tracing element that is periodically transported in the vicinity of the droplet surface. Note the distinct difference from the toroidal trajectories established within droplets exposed to axisymmetric flows.

Fig. 3 (A) Numerically-predicted trajectory of a flow–tracing element within the symmetry (x-y) plane of the droplet. (B) Streamlines (upper half) and velocity vectors (lower half) of the droplet secondary motion on a constant–φ plane, as attributed to the radial (u) and polar (v) components of the liquid velocity field.

Fig. 4 Liquid surface rotation pattern observed experimentally.

Fig. 5 Suspended-droplet experimental setup: 1) CW Argon ion laser, 2) sheet forming optics, 3) laser sheet, 4) suspended droplet, 5) laminar flow device, 6) computer, 7) frame grabber, 8) microscope, 9) video camera, 10) video monitor, 11) video cassette recorder.

Fig. 6 Experimental configuration for needle-suspended droplet internal flow visualization. The three mutually orthogonal orientations (A, B and C) represent the laser slicing directions.

Fig. 7 False color fluorescence images for perspectives A, B, C displayed in Fig. 6. The times after the onset of each dye injection event are shown beside each frame.

Fig. 8 (A) Geometric distortion of conjugate image-object pairs for a spherical droplet calculated according to Ref. [35]; the units are fractions of the droplet radius. The dashed curve corresponds to the distorted image, while the solid line represents zero distortion. (B)

Actual trajectory of a spiral path (solid) line and apparent path (dashed line) for the same relative refractive index as in (A).

Fig. 9 Dimensionless azimuthal velocity component w along a radius at θ=52.5°; the solid curve shows predicted values, while the dashed line corresponds to a rigid-body rotation. The radial variation of the time period required for a fluid element to complete a closed trajectory is also shown.

Fig. 10 Model-predicted variation of polar velocity component v on the droplet surface vs. θ, for several values of the imposed boundary rotation frequency f_s.

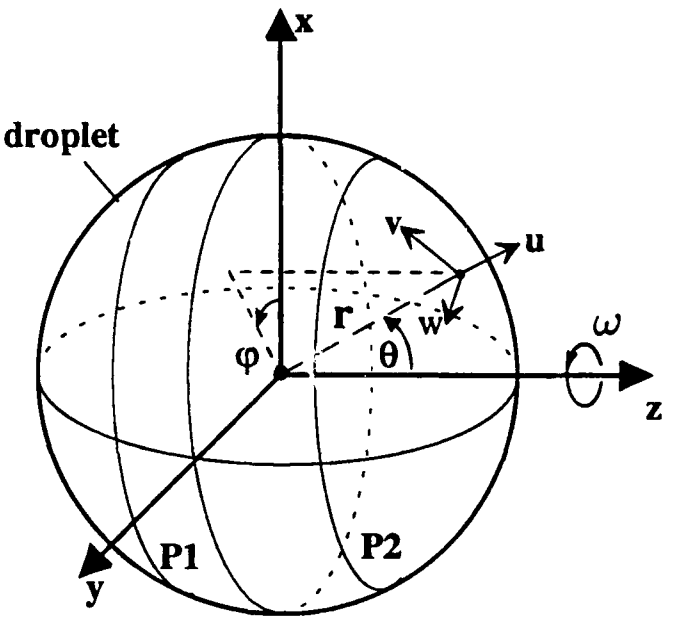

Fig. 1

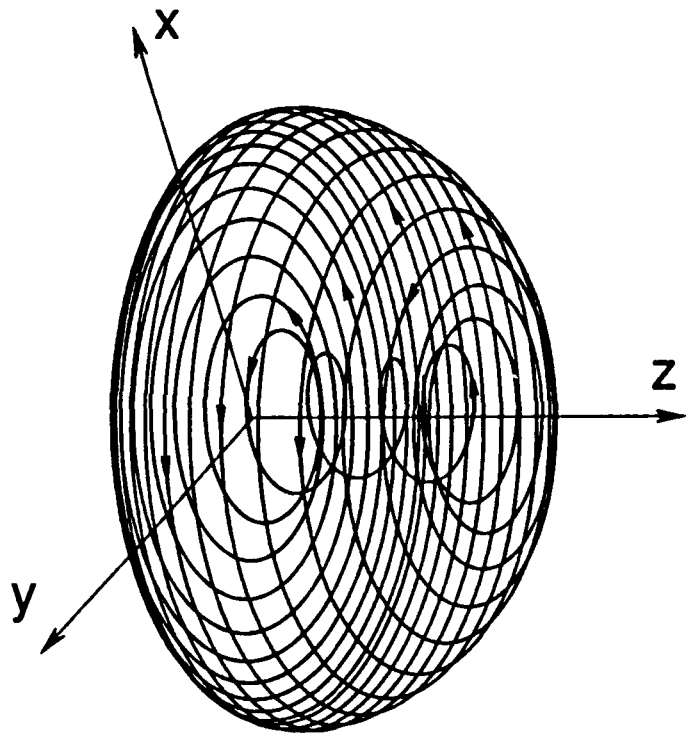

Fig. 2

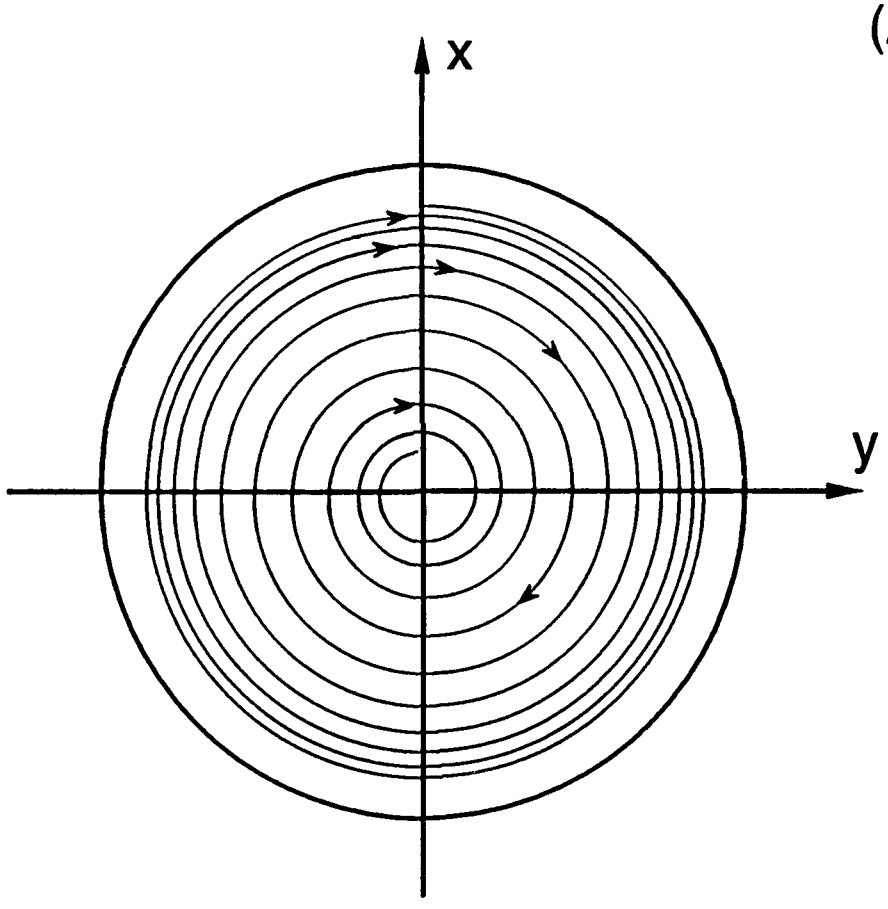

Fig. 3A

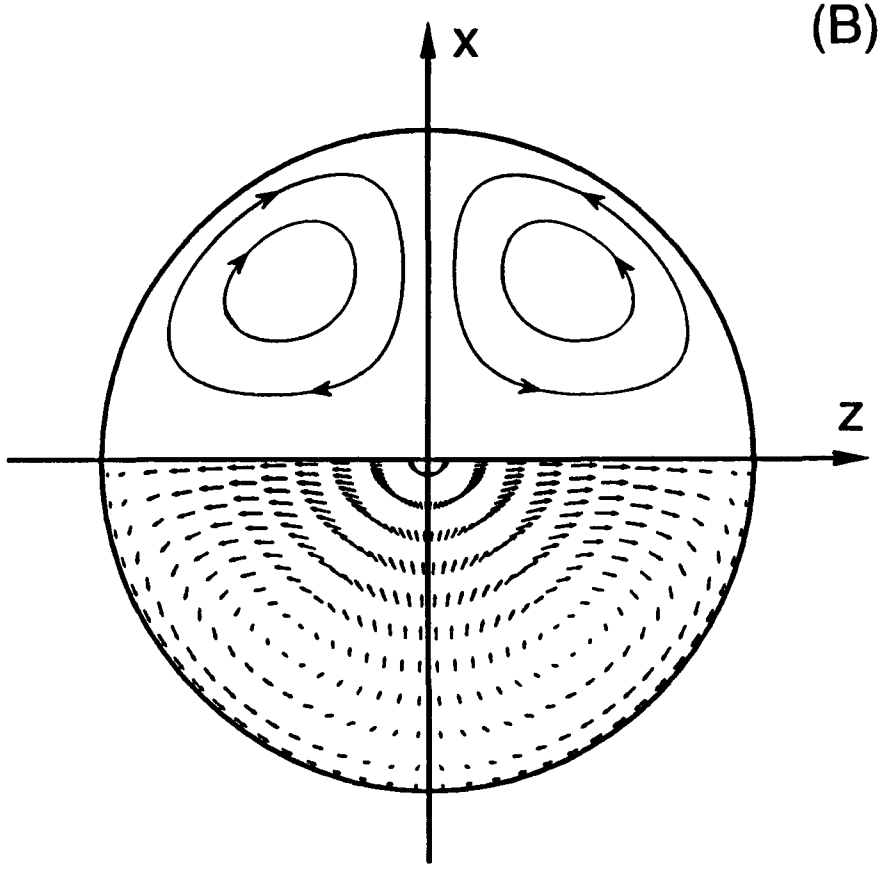

Fig. 3E

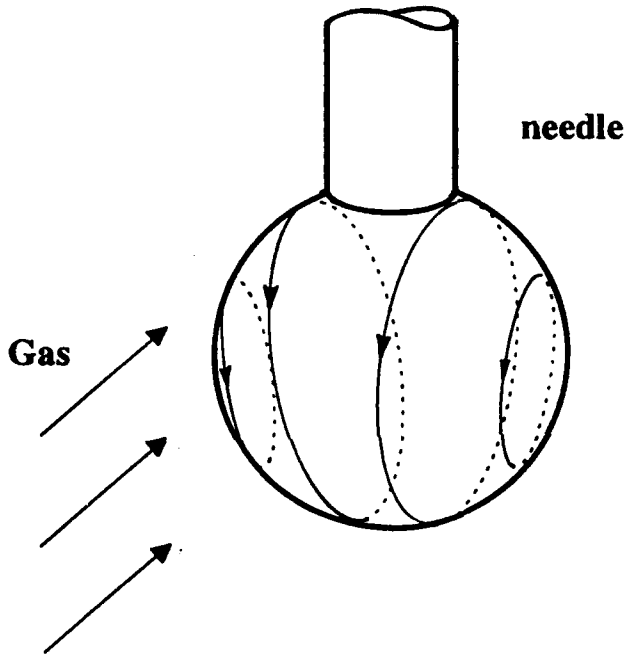

Fig. 4

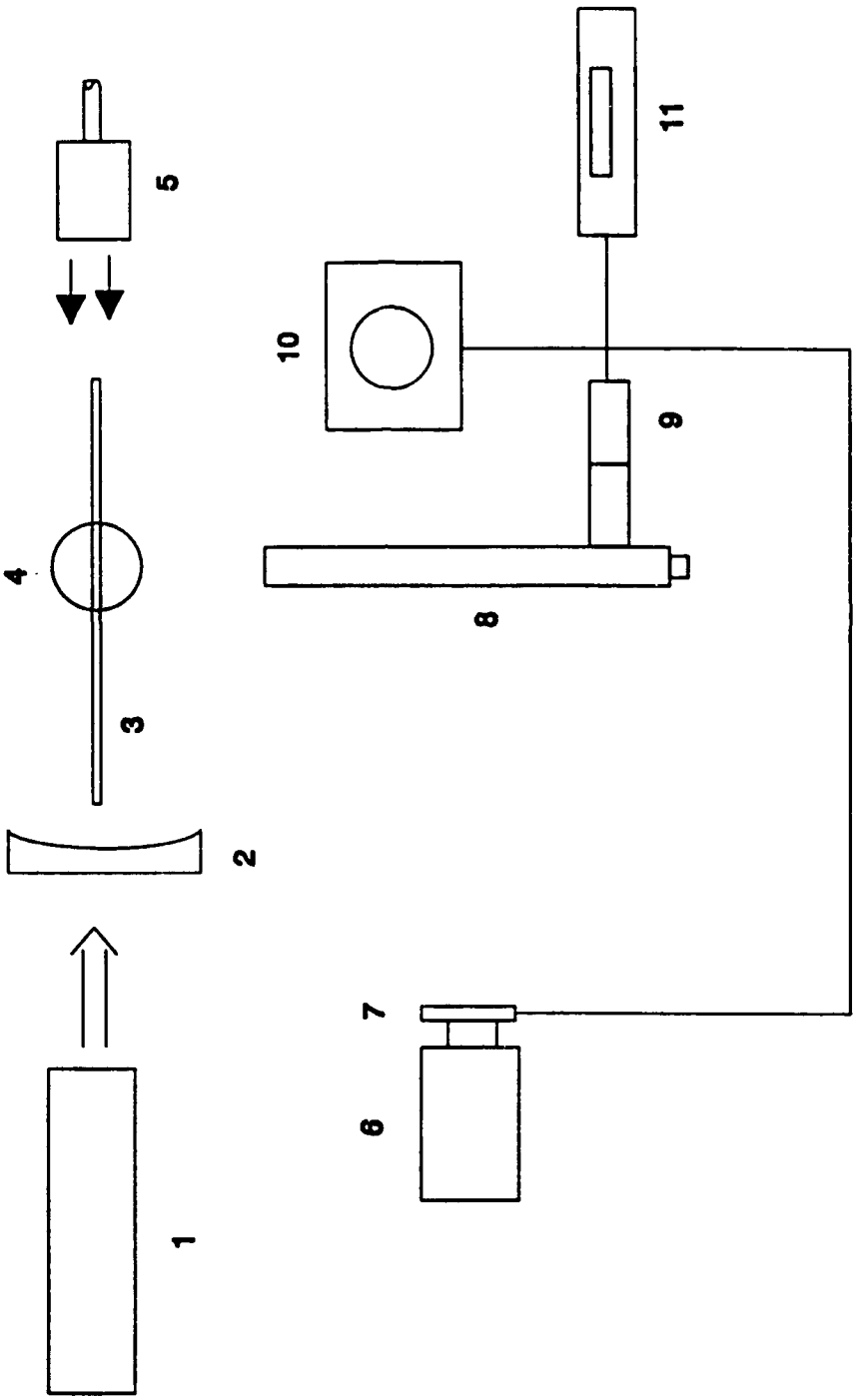

Fig. 5

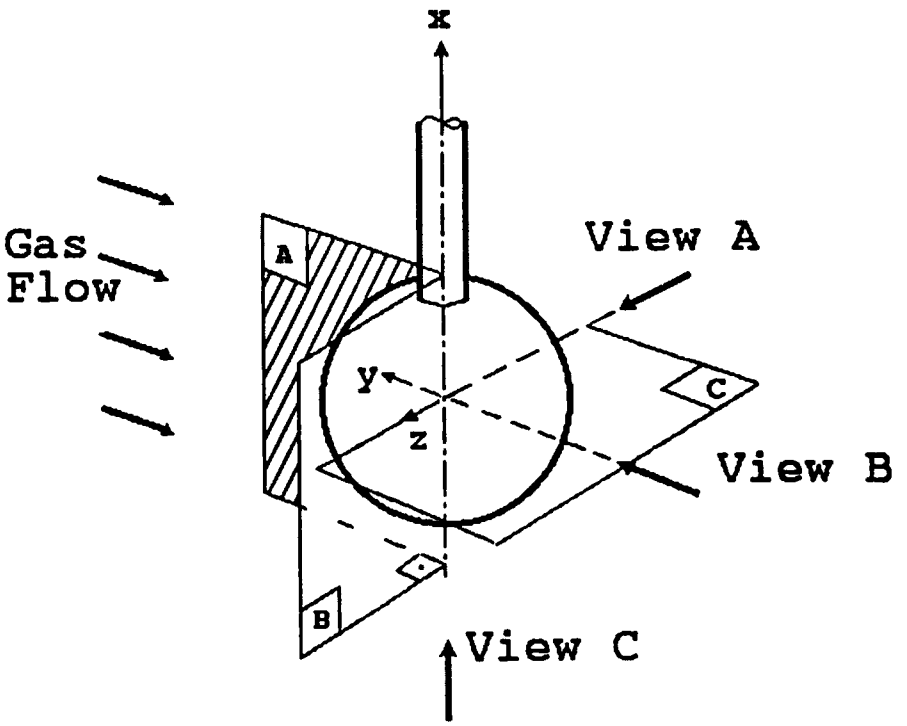

Fig. 6

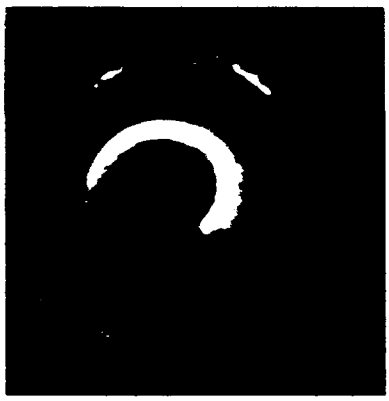

Gas Flow ←

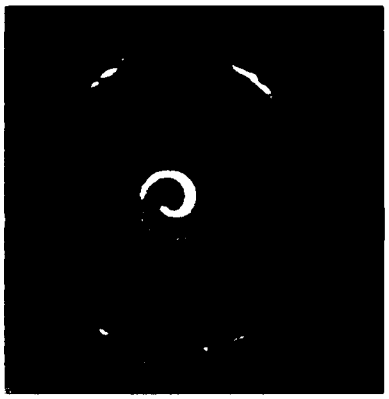

Gas Flow

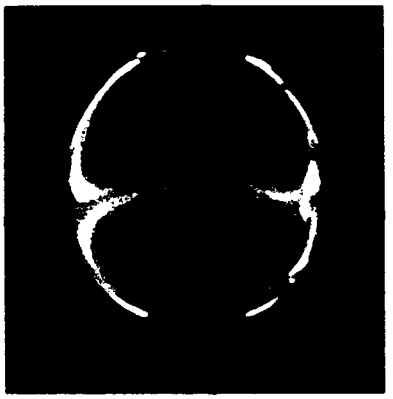

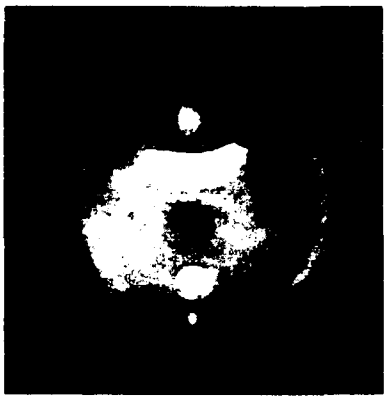

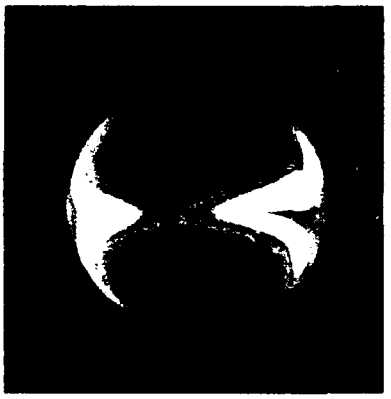

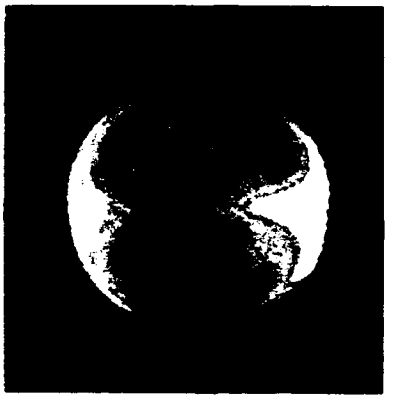

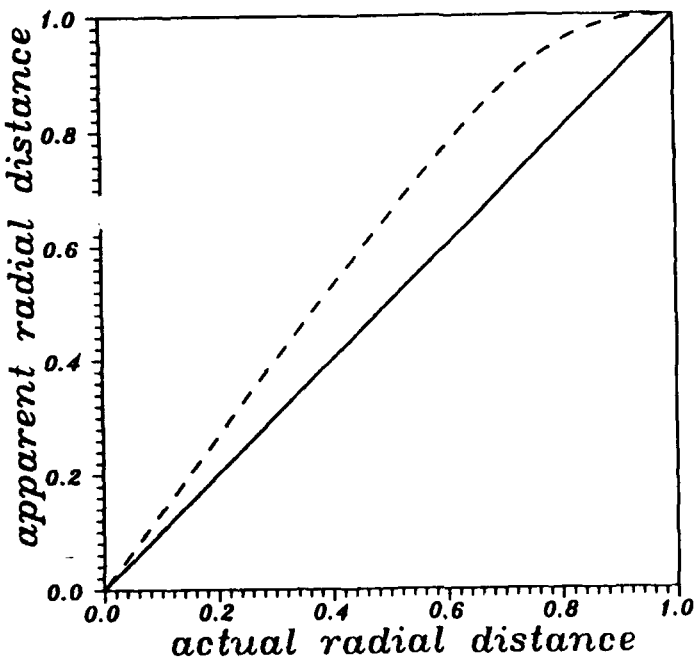
apparent radial distance
actual radial distance
1.0
0.8
0.6
0.4
0.2
0.0
0.0
0.2
0.4
0.6
0.8
1.0

Fig. 8A

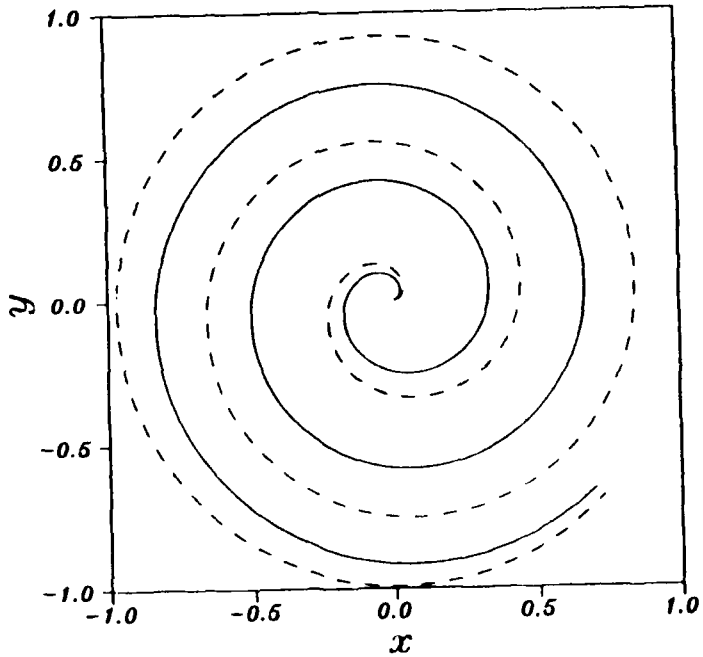
y
x
1.0
0.5
0.0
-0.5
-1.0
-1.0
-0.5
0.0
0.5
1.0

Fig. 8B

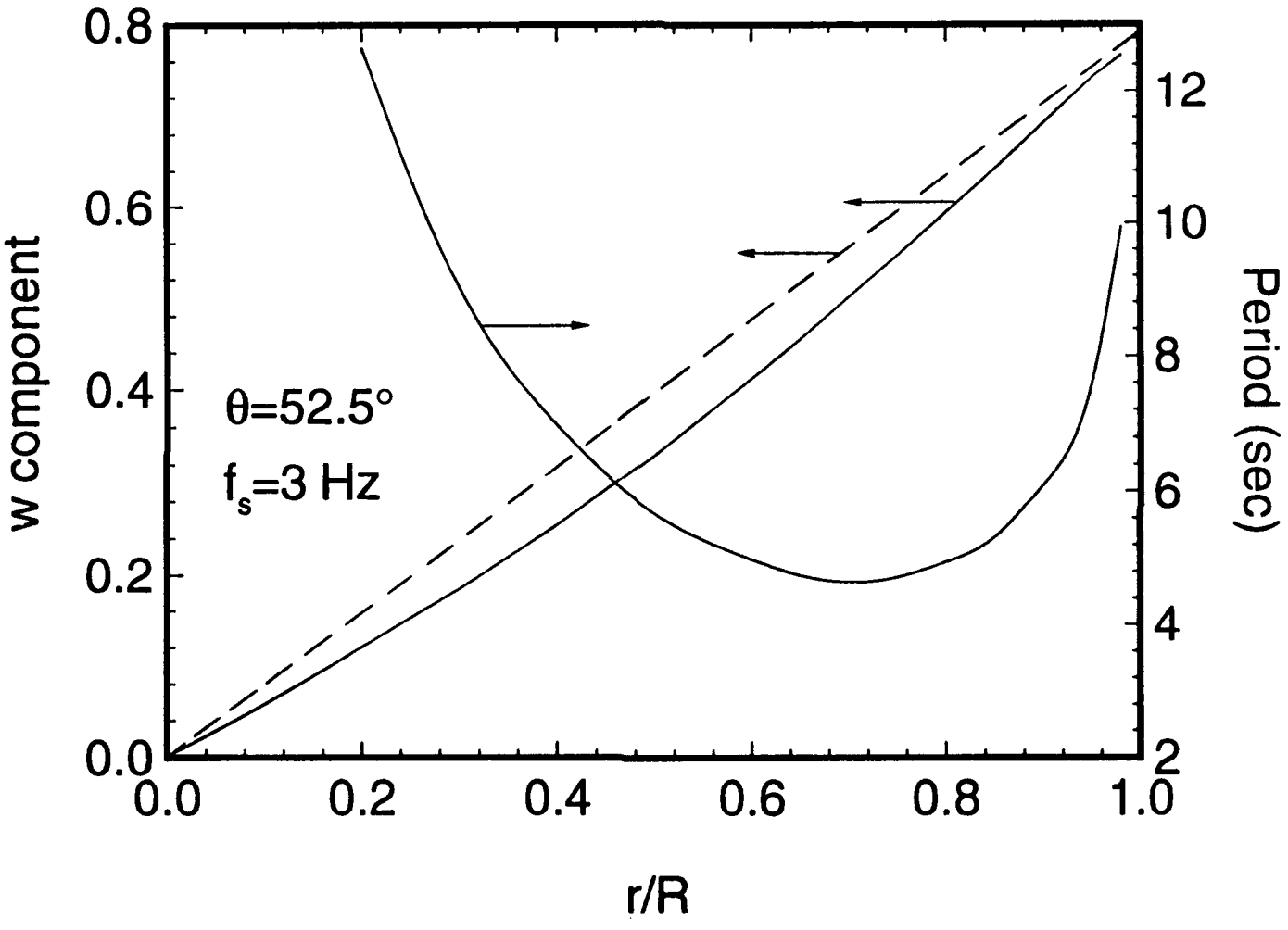
0.8
0.6
0.4
0.2
0.0
w component
θ=52.5°
f_s=3 Hz
0.0
0.2
0.4
0.6
0.8
1.0
r/R
12
10
8
6
4
2
Period (sec)

Fig 9

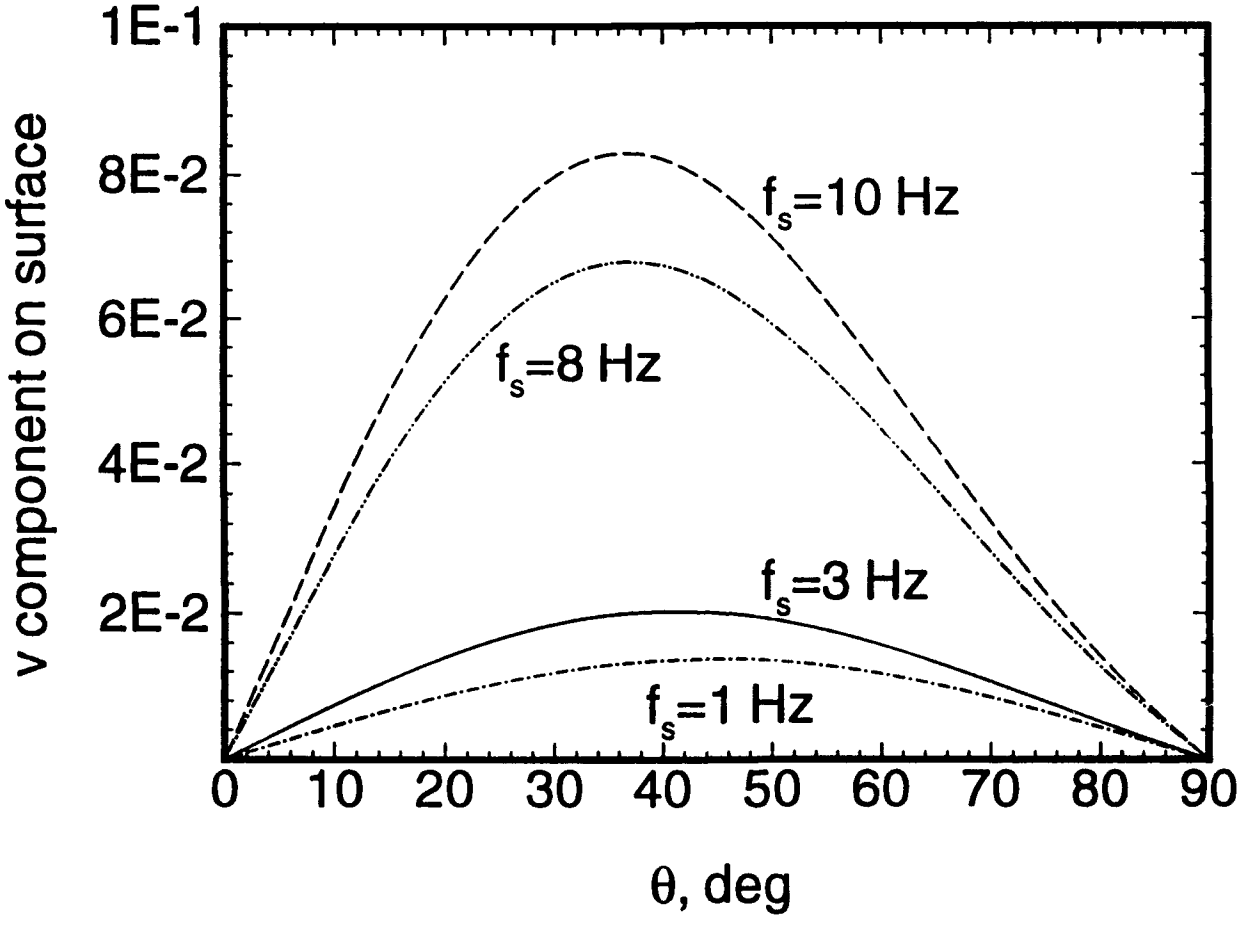
1E-1
8E-2
6E-2
4E-2
2E-2
v component on surface
f_s=10 Hz
f_s=8 Hz
f_s=3 Hz
f_s=1 Hz
0
10
20
30
40
50
60
70
80
90
θ, deg

Fig. 10

APPENDIX B

Combust. Sci. and Tech., 1993, Vol. 92, pp. 291-311
Photocopying permitted by license only

Liquid-Phase Variable Property Effects in Multicomponent Droplet Convective Evaporation

CONSTANTINE M. MEGARIDIS *Department of Mechanical Engineering University of Illinois at Chicago Chicago, Illinois 60607-7022*

Abstract—A numerical investigation is presented for multicomponent droplet evaporation under high-temperature laminar convective conditions. The study improves an existing model that did not account for the temperature dependence of liquid-phase densities and heat capacities. The new model, which accounts for variable gas and liquid-phase thermophysical properties, has also resolved previously reported numerical problems encountered during the early stages of the simulations. Detailed data on the temporal and spatial variation of the liquid-phase concentration fields throughout the lifetime of a bicomponent droplet provide new insight on the liquid mass-transport mechanisms within typical vaporizing hydrocarbon droplets. The current simulations indicate that the variation of liquid densities with temperature must be taken into account for an accurate representation of the transport processes in droplet convective vaporization. On the contrary, the effect of the variation of liquid heat capacities with temperature proves to be rather minor.

Key words: Multicomponent, droplet, evaporation, modeling

INTRODUCTION

It has been established that the transport phenomena involved in both droplet combustion and vaporization are qualitatively similar. Since gas-phase reaction rates are substantially higher than the liquid vaporization rates under high-temperature conditions, liquid component evaporation is the controlling process in most cases of spray combustion. The issues related to the vaporization of spray droplets are very important in combustor design and modeling. Therefore, the appropriate mechanisms must be adequately represented for the correct evaluation of energy conversion rates, mixture ratio distributions and overall combustor behavior. Recent knowledge on droplet vaporization and spray combustion is summarized in a series of review articles by Law (1982), Faeth (1983), Sirignano (1983), and Dwyer (1989). A wide variety of spray combustion issues is addressed in these articles and the contributions of a large number of investigations during the past several decades are analyzed.

A variety of models has been developed to simulate the spray dynamics under dense spray conditions. Idealized configurations, modeling single (Sangiovanni and Kesten, 1976) or multiple streams (Rangel and Sirignano, 1986; Delplanque et al. 1990) of fuel droplets have provided important insight on the related issues. More detailed droplet vaporization models have appeared recently that account for droplet interactions and employ a thorough representation of the gas and liquid-phase processes (Raju and Sirignano, 1990; Chiang and Sirignano, 1990). Even though spray models simulate conditions that are often encountered in practical systems, they frequently represent the related transport phenomena inadequately due to the very lengthy computational times associated with detailed modeling. On the other hand, the individual droplet processes are of primary importance in spray combustion applications, since many times the droplets are well separated from each other (dilute spray limit). To this end, detailed models (Haywood et al. 1989; Chiang et al. 1992) simulating the complex transport phenomena in convective droplet vaporization have provided an important insight on processes that are not thoroughly understood.

The multicomponent nature of most practical fuels used today in liquid-fired combustion systems signifies the importance of models that examine multicomponent droplet evaporation in high-temperature convective conditions. Megaridis and Sirignano (1990)

presented a detailed numerical model that examined the fundamental mass, momentum, and energy exchange processes governing the vaporization behavior of isolated bicomponent liquid droplets. The model provided data on the temporal and spatial variation of gas and liquid field parameters, as well as the temporal variation of global droplet quantities (drag coefficient, Nusselt and Sherwood numbers, etc). The same authors in a subsequent paper (Megaridis and Sirignano, 1992) presented a parametric study that examined the influence of various flow parameters, and evaluated the potential of droplet microexplosion for some hydrocarbon mixtures. The current work extends the model of Megaridis and Sirignano (1990, 1992) by incorporating the temperature variation of liquid-phase densities and heat capacities that have not been previously accounted for. Some additional information is also presented herein that elucidates important aspects of multicomponent-liquid convective evaporation.

MODEL DESCRIPTION

Experimental measurements of both droplet and gas-phase velocities in practical spray flames (Presser et al. 1990) have shown that even though the conditions in a typical spray combustor are turbulent, the typical values of Reynolds number (based on droplet diameter and relative velocity between the droplet and the free flow) are of the order of 100. The consideration of multicomponent liquid droplets is also of direct practical interest, since most conventional aerospace and diesel fuels consist of multiple substances.

The droplet configuration considered herein is identical to that modeled by Megaridis and Sirignano (1990) and involves a laminar, axisymmetric flow around a spherical, multicomponent droplet which has initially no internal motion and a uniform temperature before it is injected into a uniform, hot gas stream. As a result of the induced drag force, the droplet is accelerated in the direction of the gaseous stream, therefore, the relative velocity between the free stream and the droplet is reduced with time. An additional source of unsteadiness results from the establishment of shear-induced liquid motion and droplet heating which persist during the largest portion of the droplet lifetime.

A modified model based on the bi-component droplet work of Megaridis and Sirignano (1990, 1992) is employed in the current study. The original model considered the different volatilities of the liquid components, the alteration of the liquid-phase properties due to the spatial/temporal variations of the species concentrations, and also the effects of multicomponent gas-phase diffusion. No external body forces or thermal radiative effects were considered. Phase equilibrium was assumed over the gas/liquid interface, and gas solubility effects in the liquid phase were also neglected. Additional features of the model included variable thermophysical properties in the gas phase, variable liquid viscosity, mass diffusivity, conductivity and heat of vaporization, transient droplet heating with internal liquid circulation, droplet surface regression due to vaporization, and finally, droplet deceleration with respect to the free flow due to drag. The model produces time-varying spatially-resolved data for the entire flow field in the vicinity of a droplet, and thus provides important information on the fundamental processes governing the energy, mass, and momentum exchange between the two phases of vaporizing droplets in convective environments.

Even though Megaridis and Sirignano (1990) considered the variation of all liquid-phase thermophysical properties with species concentrations, they did not consider the dependence of liquid densities and heat capacities on temperature. Since in a typical spray combustion environment a liquid hydrocarbon droplet is heated significantly throughout its lifetime, the liquid densities are expected (Vargaftik, 1975) to diminish gradually as the droplet heating proceeds. The current model incorporates the temperature dependence of all liquid properties and examines its effects on droplet vaporization

dynamics. The temperature variation of the thermophysical properties of all gaseous and liquid components is given in the Appendix.

Since the local density of the liquid droplet varies throughout the simulation, the volumetric average droplet density at a specific instant is defined by

$$\rho_{l,ave} = \frac{3}{2a^3} \int_0^a r^2 dr \int_0^\pi \rho_l(r,\theta) sin\theta d\theta \tag{1}$$

where a is the instantaneous droplet radius, ρ_l the local value of liquid density, and r, θ the radial and angular spherical coordinates with respect to the droplet center.

The competing effects of vaporization and liquid heating are apparent in the following expression, which gives the rate of change of the instantaneous droplet radius a as a function of the volumetric average liquid density $\rho_{l,ave}$ (given by Eq. (1)), its rate of change, the gas density ρ_g above the droplet interface, and finally, the normal component of the vaporization velocity $V_{g,n}$ above the liquid surface

$$\frac{da}{dt} = -\frac{1}{2\rho_{l,ave}} \int_0^\pi \rho_g(\theta) V_{g,n}(\theta) sin\theta d\theta - \frac{a}{3\rho_{l,ave}} \frac{d\rho_{l,ave}}{dt} \tag{2}$$

The integral term on the right hand side of Eq. (2) depicts the loss of liquid mass due to vaporization from the droplet surface and is thus negative, while the second term is intrinsically positive since the volumetric average liquid density decreases monotonically with time $\left(\frac{d\rho_{l,ave}}{dt} < 0\right)$. The dominance of one of the above two terms obviously designates if the droplet expands $(\frac{da}{dt} > 0)$ or contracts $(\frac{da}{dt} < 0)$ during the heating period. In order to account for changes of the droplet volume due to the combined effect of liquid-component heating and vaporization, a continuous adjustment (as dictated by Eq. (2)) of the numerical grid in both phases is required throughout a simulation.

The governing equations in both gas and liquid phases, along with the gas/liquid interface conditions are given in detail in Megaridis and Sirignano (1990). The solution of the system of equations is performed numerically using finite-difference discretization techniques and employing an implicit iterative solution procedure (Chiang et al. 1992). A change of reference frame from a stationary coordinate system to a system moving with the droplet is performed in order to facilitate the computation. Since the relative velocity between the free stream and the droplet varies with time, an adjustment of the surrounding gas flow field is necessary throughout the calculation. The droplet is assumed to be spherical at all times, since the corresponding Weber and Bond numbers for the flows considered herein are sufficiently low to justify the assumption of no shape deformation.

An additional improvement of the current model over the previously published study of Megaridis and Sirignano (1990, 1992) is related to the finite-difference discretization of the convective terms of the liquid-phase energy and mass fraction equations. As reported by Megaridis and Sirignano (1990), the liquid mass-fraction model predictions displayed some oscillating behavior during the early stages of the simulations. This event was then attributed to the steep liquid concentration gradients established in the vicinity of the droplet surface, as a result of the vigorous preferential vaporization of the more volatile liquid component. However, a recent study by Shih and Megaridis (1993) determined that these oscillations are due to inherent limitations of the central-difference discretization schemes employed originally by Megaridis and Sirignano in the relevant transport equations. The current model employs a hybrid upwind discretization scheme

TABLE 1
Values of Physical Parameters Used in Base-Case Simulation

Parameter	Value
Initial gas-phase Reynolds number (based on diameter)	100
Free stream temperature, [*K*]	1250
Ambient pressure, [*atm*]	10
Initial droplet temperature, [*K*]	300
Prandtl number, gas phase	0.74
Initial liquid-phase Prandtl number	8.1
Lewis number, gas phase	3.23
Initial liquid-phase Lewis number	41.
Molecular weight, air, [*kg/kmol*]	28.96
Molecular weight, n-octane, [*kg/kmol*]	114.2
Molecular weight, benzene, [*kg/kmol*]	78.11
Latent heat at normal boiling point (398.8 K), n-octane [*kJ/kg*]	301.3
Latent heat at normal boiling point (353.3 K), benzene [*kJ/kg*]	393.8
Liquid/Gas viscosity ratio at injection (i.e., time=0)	11.48
Liquid/Gas conductivity ratio at time=0	1.78
Liquid/Gas density ratio at time=0	280.4
Liquid/Gas specific heat ratio at constant pressure, time=0	1.7

(in place of the previously used central differencing) that was proven to resolve the liquid phase concentrations adequately, without displaying signs of numerical oscillations.

Since the processes in the gas phase are significantly faster than those in the liquid phase, careful consideration must be taken for proper resolution of the various gas/liquid transport processes involved (Megaridis and Sirignano, 1990). The widely disparate characteristic times and length scales of the problem considered herein, with the added complexity of the coupled momentum, heat and mass transfer processes demand fine temporal and spatial resolution, therefore, the related computations are quite intensive. These computations were performed on a CRAY Y-MP supercomputer.

RESULTS AND DISCUSSION

As in Megaridis and Sirignano (1990), the base case in the current study simulates a cold bi-component liquid droplet suddenly injected into a hot air stream which is free of fuel vapor. The ambient pressure is 10 atm, corresponding to a typical combustor environment. The liquid phase is assumed to be initially quiescent. The two hydrocarbon components considered are n-octane (C_8H_{18}) and benzene (C_6H_6) with initial mass fractions of both liquids equal to 50%. These liquid components are considered to be fully miscible, and were selected because of their substantially different volatilities and physical properties. In addition, the selection of hydrocarbons for this study is relevant since most liquid fuels consist of hydrocarbon mixtures. The values of physical parameters and non-dimensional groups employed in the base-case calculation are given in Table 1. It should be emphasized that the non-dimensional numbers listed in Table 1 are based on initial conditions and are not representative of subsequent stages. For example, liquid-phase heating causes significant variations of the liquid-phase Lewis and Prandtl numbers due to the strong dependence of thermophysical properties on temperature. More specifically, uniform droplet heating from 300 K to 450 K would cause a reduction of the corresponding

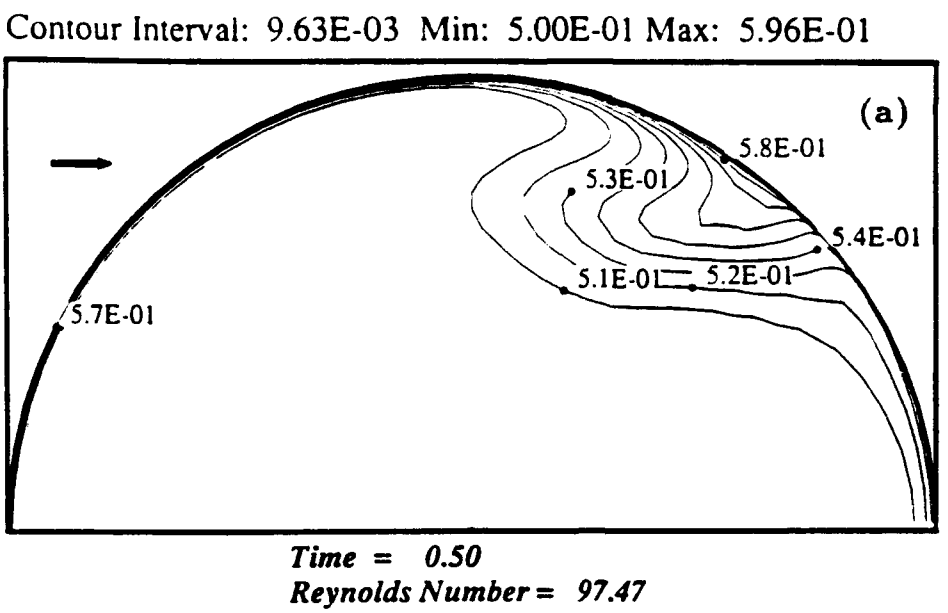

FIGURE 1a Liquid-phase n-octane mass fraction contours at three different instants of the base-case droplet simulation. (a) time = 0.5. The instantaneous Reynolds number is based on droplet diameter, and relative velocity between droplet and ambient stream. The ambient gas flow direction is indicated by the arrow.

liquid-phase Lewis number almost by a full order of magnitude (from 41 to 4.5 for the base-case droplet). The same event would cause a reduction of the liquid-phase Prandtl number by a factor of two (from 8.1 to 4.2).

The computational mesh employed throughout the numerical simulations consisted of 40 (radial direction) × 35 (angular direction) nodes in the gas phase, and 30 × 35 nodes in the liquid phase. The numerical grid was uniform in the angular direction, while variable spacing in the radial direction was employed with dense packing near the droplet surface, in order to resolve the high gradients occurring in the vicinity of the gas/liquid interface. The above grid proved to be adequate for a smaller than 5% deviation from the values obtained when a much finer grid (50% more nodes) was employed. The computational domain extended to a distance of approximately eighteen droplet radii from the droplet center, which proved to be adequate for far-field independent results. The times quoted in this section are normalized with respect to the characteristic time for gas-phase hydrodynamic diffusion, defined as the square of the initial droplet radius divided by the free-stream kinematic viscosity.

As reported in Megaridis and Sirignano (1990, 1992), liquid heating starts immediately when the cold n-octane/benzene droplet is immersed in a high-temperature convective air flow. Even though the liquid phase is initially quiescent, the time required to establish the liquid-phase motion is relatively short. In addition, the intensity of the liquid-phase motion varies considerably during the droplet lifetime. The heat transfer from the gas to the liquid phase is very intense at the initial stages, when liquid component evaporation is very slow due to low droplet-surface temperatures. As the droplet temperatures increase, vaporization becomes more vigorous, thus causing partial depletion of the more volatile species (benzene) from the droplet surface. While benzene vaporizes preferentially from the gas/liquid interface, the droplet surface is continuously resupplied with additional amounts of this component from the droplet interior through the convective liquid motion and the slower mass diffusion processes. Even though the droplet surface composition

Contour Interval: 9.4E-03 Min: 5.0E-01 Max: 5.9E-01

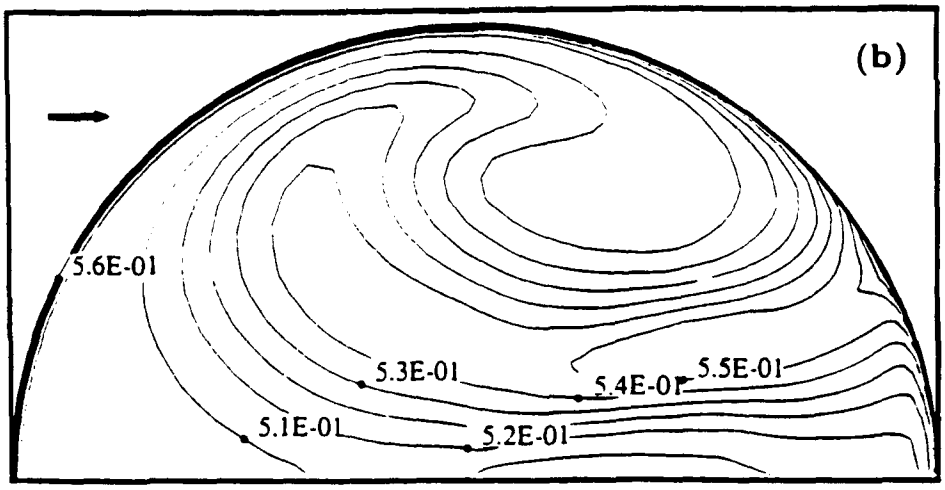

Time = 1.00
Reynolds Number = 95.34

Contour Interval: 1.98E-02 Min: 7.26E-01 Max: 9.24E-01

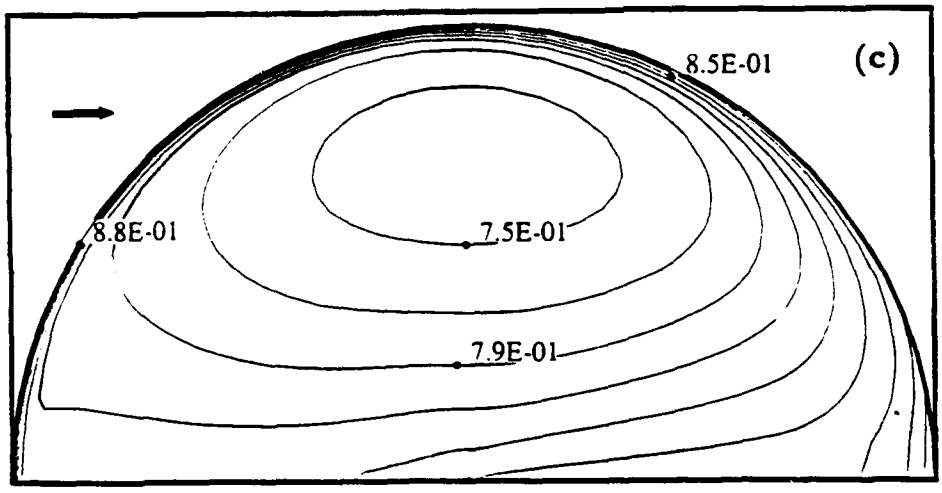

Time = 10.00
Reynolds Number = 66.89

(b) time = 1, and (c) time = 10

FIGURE 1b,c Liquid-phase n-octane mass fraction contours at ~~three different instants~~ of the base-case droplet simulation ~~(b) and (c)~~. The instantaneous Reynolds numbers are based on droplet diameter, and relative velocity between droplet and ambient stream. The ambient gas flow direction is indicated by the arrow.

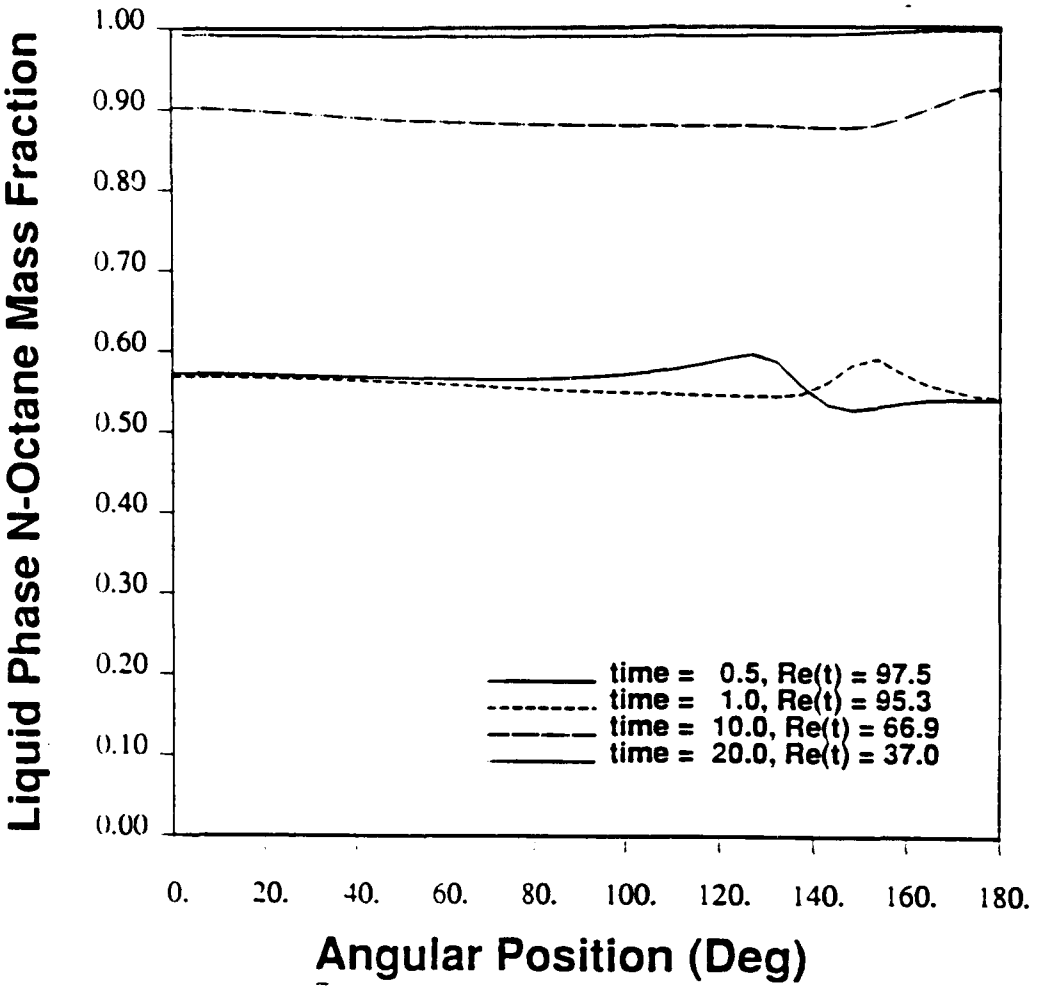

FIGURE 2 Angular variation of liquid n-octane mass fractions on the droplet surface at four different instants of the base-case droplet simulation (0.5, 1, 10 and 20).

shows increasingly higher mass fractions of the less volatile species, the calculations showed that both liquid mixture components vaporize together almost throughout the droplet lifetime. However, the instantaneous evaporation rates of the two liquid components remain substantially different (see also Fig. 4 below).

The above sequence of events is clearly displayed in Fig. 1 showing the n-octane mass fraction contours in the droplet interior at three different instants of the base-case simulation which was performed using the modified model. Figure 1a depicts the n-octane mass fractions at a very early stage (non-dimensional time=0.5) during the establishment of the liquid-phase circulating motion. The developing steep gradients below the gas/liquid interface are shown, while the preferential vaporization of benzene from the interface is displayed by the increasing n-octane concentrations along the wave-like feature and towards the droplet surface. Figure 1b depicts the n-octane mass fractions at a later stage (non-dimensional time=1), shortly after the establishment of the liquid-phase circulating motion. The dominant influence of liquid convection on the establishment of the mass fraction contours is apparent in this figure, which also demonstrates the gradual "global enrichment" of the droplet in n-octane as a result of the preferential vaporization of

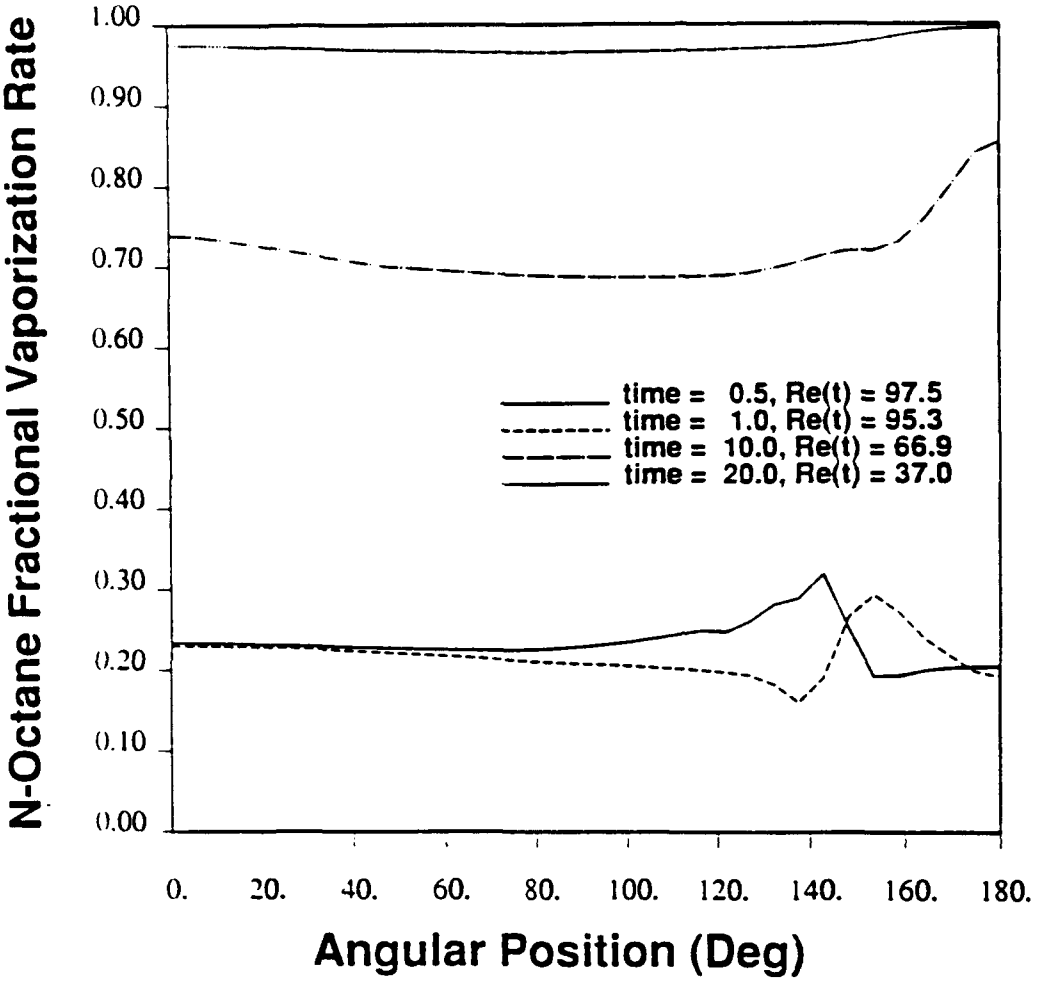

FIGURE 3 Angular variation of liquid n-octane fractional vaporization rates on the droplet surface at four different instants of the base-case droplet simulation (0.5, 1, 10 and 20).

benzene from the droplet surface. Figure 1c depicts the n-octane mass fractions at a subsequent stage (non-dimensional time=10) which corresponds to an instant where 35% of the droplet mass has vaporized. As shown in Fig. 1c, lower mass fractions of n-octane are established in the core of the liquid vortex, while higher values are (naturally) seen in the vicinity of the droplet surface. The spatial redistribution of mass and gradual enrichment of the droplet interior in the less volatile component is a result of the slow liquid-phase mass diffusion processes that prove inadequate to keep up with the gradual depletion of benzene from the droplet surface.

Figure 2 shows the angular variation of liquid n-octane mass fractions on the droplet surface at four different instances of the base-case simulation. The front stagnation point of the flow corresponds to angle zero, while the point on the axis of symmetry near the droplet wake is characterized by angle 180°. Even though these mass fractions do not show a strong angular dependence, they portray the gradual enrichment of the gas/liquid interface in n-octane (the less volatile species) as a result of the preferential vaporization of benzene. In fact, the curve corresponding to time=20 (when almost 75% of droplet mass has vaporized) indicates almost complete depletion of benzene from the droplet

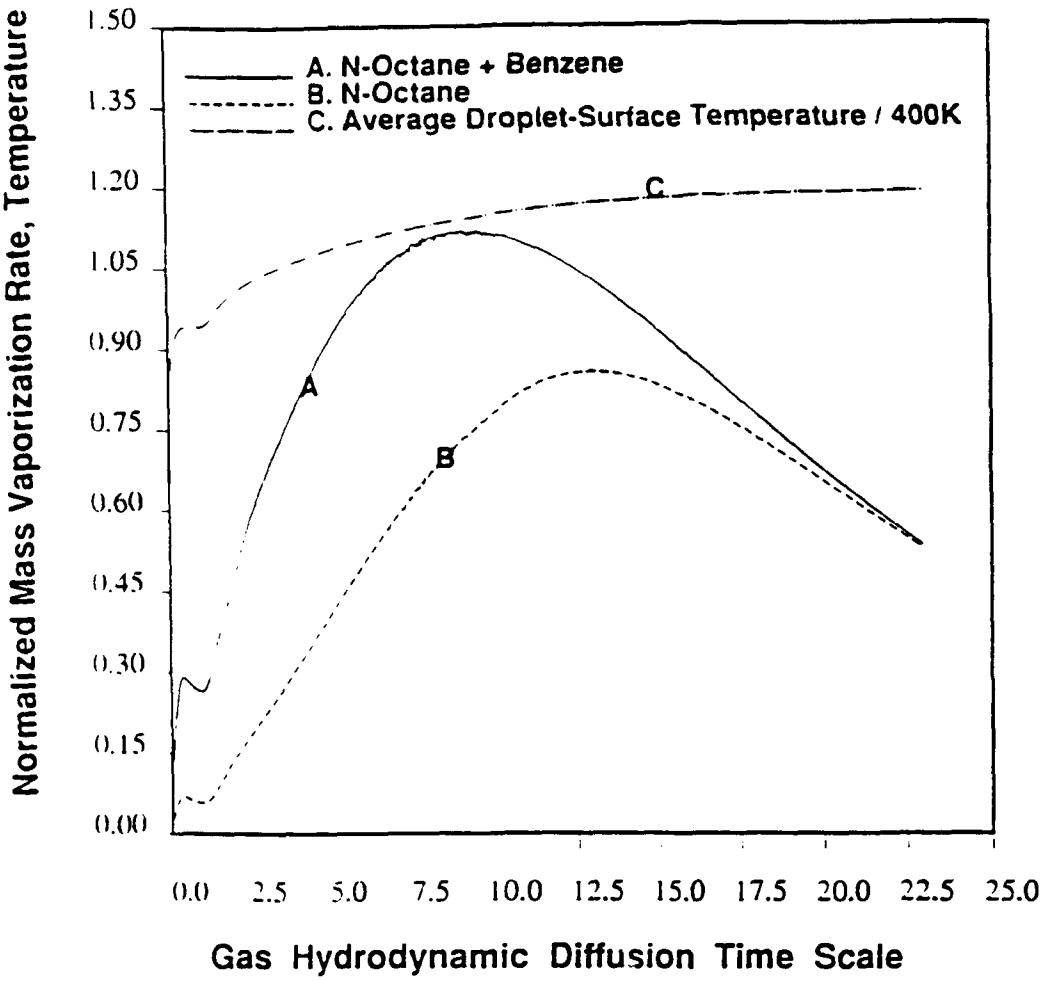

FIGURE 4 Timewise variation of normalized mass evaporation rates and surface-averaged droplet temperatures for the base-case droplet simulation. (A) Total evaporation rate, (B) n-octane evaporation rate, and (C) temperature.

surface. The early shift of the peak value towards the aft of the droplet is a result of the establishment of the liquid-phase motion. Figure 3 shows the angular variation of liquid n-octane fractional vaporization rates on the droplet surface at four different instances of the base-case simulation. The fractional vaporization rate (ϵ_i) is a quantity describing (in a local sense) the portion of the entire vaporization flux from the droplet surface that is attributed to liquid component i (Megaridis and Sirignano, 1990). For example, values of ϵ_i near zero indicate that species i plays a minor role in the evaporating processes over the droplet surface, while values of ϵ_i near unity suggest almost exclusive evaporation of this species from the surface. Some angular dependence of $\epsilon_{C_8H_{18}}$ is apparent on this figure, especially during the early and middle stages of the simulation. The initially low values of $\epsilon_{C_8H_{18}}$ demonstrate the preferential vaporization of the more volatile benzene from the droplet surface ($\epsilon_{C_6H_6} = 1 - \epsilon_{C_8H_{18}}$). Due to the gradual depletion of benzene from the gas/liquid interface, the corresponding values of $\epsilon_{C_8H_{18}}$ become larger with time, and eventually reach a level indicating almost exclusive vaporization of n-octane from the droplet surface (see curve at time=20 of Fig. 3). It is worth noting that the corresponding

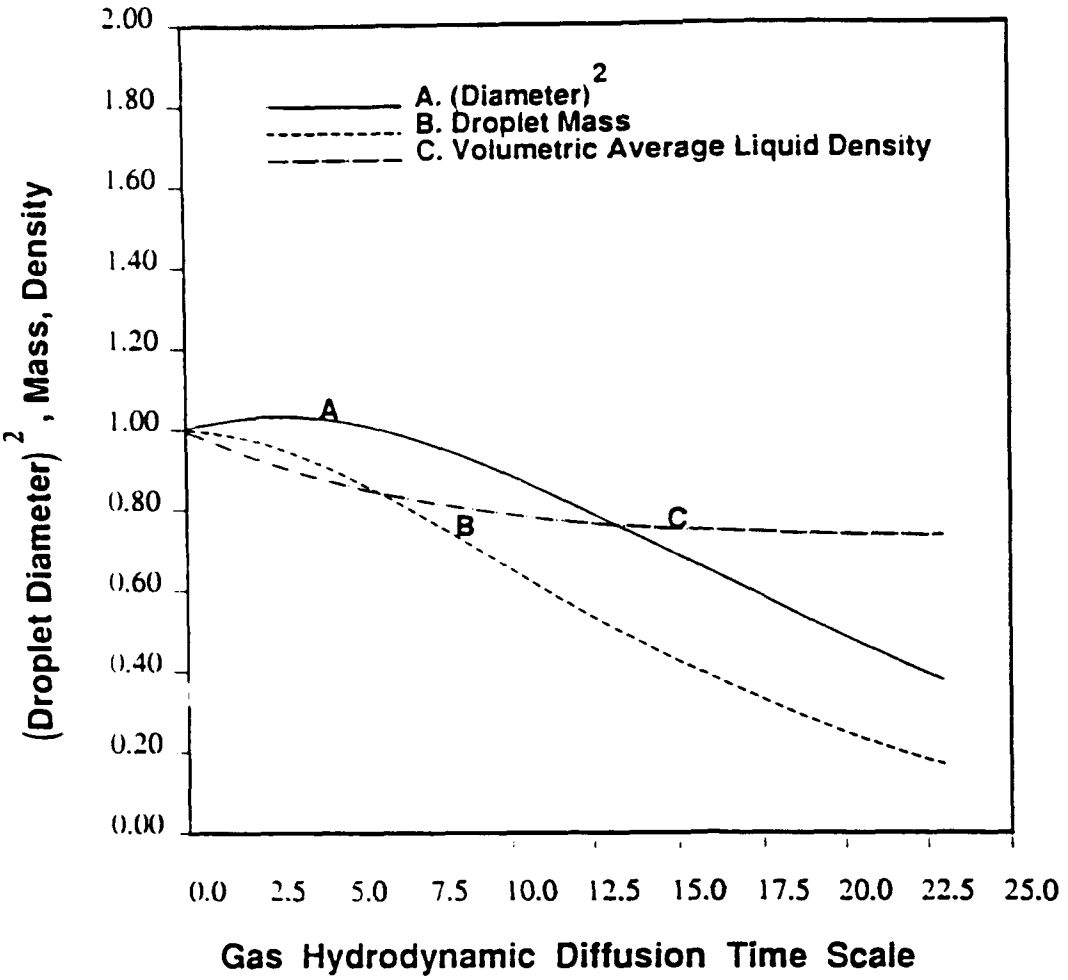

FIGURE 5 Timewise variation of normalized: (A) droplet diameter square, (B) droplet mass, and (C) volumetric average liquid density for the base-case droplet simulation.

values of the liquid mass fractions and fractional vaporization rates at each location of the droplet surface are substantially different, particularly during the early stages of the droplet lifetime.

The data presented in Figs 1-3 underline the importance of liquid-phase convection and diffusion processes in multicomponent droplet evaporation, and emphasize that transport processes in the droplet interior are very significant in the overall characterization of liquid evaporation. The mass evaporation rate at each instant of the simulation was calculated from

$$\frac{dm}{dt} = -2\pi a^2 \int_0^{\pi} \rho_g(\theta) V_{g,n}(\theta) \sin\theta d\theta \tag{3}$$

where m, a are the instantaneous values of the droplet mass and radius, ρ_g the gas mixture density above the droplet interface, and $V_{g,n}$ the normal component of the vaporization velocity. The vaporization rate given by the above equation represents the contributions of both liquid components. The contribution of species i in the overall

mass evaporation rate can be calculated using the angular distribution of the fractional vaporization rate ϵ_i of this species

$$\frac{dm_i}{dt} = -2\pi a^2 \int_0^{\pi} \epsilon_i(\theta)\rho_g(\theta)V_{g,n}(\theta)sin\theta d\theta \tag{4}$$

Figure 4 depicts the time variation of the overall (n-octane + benzene) mass evaporation rate for the base-case simulation (curve A), as well as the component attributed to the vaporization of n-octane alone (curve B). The evaporation rates shown on Fig. 4 correspond to the absolute values of the respective quantities, since the actual rates are always negative (see Eqs 3 and 4). In addition, these rates have been normalized with respect to the product of free-stream density, the square of the initial droplet radius and the initial relative velocity between droplet and free stream ($\rho_\infty a_0^2 U_{\infty,0}$). The time variation of the surface-averaged value of the droplet temperature $T_{av,s}$ (normalized with respect to 400 K) is also displayed in Fig. 4. This quantity is calculated from the local values of temperature on the gas/liquid interface using

$$T_{av,s} = \frac{1}{2}\int_0^{\pi} T_s(\theta)sin\theta d\theta$$

where θ is the angular position on the droplet surface ($\theta = 0$; front stagnation point). It is apparent from Fig. 4 that the overall mass evaporation rate is strongly dependent on time. The n-octane/benzene droplet mass evaporation rate initially increases and attains a temporal maximum at time ≈ 9, as a result of the initially slow droplet-surface regression rate and the increasing vaporization velocities (see Eq. 3). However, at subsequent times, the significant droplet-surface regression rate overtakes the effect of increasing vaporization velocity (due to higher liquid temperatures), an event that leads to a monotonic reduction of the droplet evaporation rate, even though the droplet temperatures maintain an increasing trend (curve C). As also seen on Fig. 4, during the early stages of the droplet lifetime, the main portion of the droplet mass evaporation rate is attributed to the evaporation of benzene. As time advances, the liquid droplet gradually heats up and benzene is depleted from the droplet surface as well as the droplet interior. During that time, n-octane accounts for increasingly higher portions of the overall evaporation rate, which eventually leads to exclusive evaporation of this species only (see Fig. 4 at times > 20). It is worth noting that information on partial evaporation rates of multicomponent droplets is needed for the calibration of exciplex-based vapor/liquid visualization techniques that are employed today in fuel spray evaporation studies (Rotunno et al. 1990). Finally, it should be noted that the droplet-surface temperature eventually rises to a level around 480 K, as shown by curve C of Fig. 4. This temperature is lower than the boiling point of pure n-octane (511 K) at the simulated pressure of 10 atm, but is significantly higher than the boiling point of pure benzene (451.6 K) at the same pressure.

We now turn our attention to the temperature variation of liquid densities; and its influence on the droplet vaporization dynamics. The liquid-density reduction with increasing droplet temperatures would obviously result in droplet expansion if vaporization were not present. On the other hand, liquid-component evaporation has the opposite effect, since it reduces the mass of the liquid by the transfer of fuel vapor from the droplet surface into the gas phase. Since the above two mechanisms (density reduction and vaporization) are simultaneously present and have variable intensities throughout the droplet lifetime, they compete continuously with an unclear outcome. Figure 5 shows the temporal variations of the square of droplet diameter (curve A), droplet mass m (curve B), and volumetric average liquid density $\rho_{l,ave}$ (curve C) as defined by Eq. (1).

All three quantities have been normalized with respect to their initial values. The time variation of droplet diameter clearly shows that the n-octane/benzene droplet actually expands during the heating stage, and that the applicability of the d^2-law is not valid until time ≈ 10 when approximately 35% of the droplet mass has vaporized. This period represents approximately 40% of the entire droplet lifetime. Thermal swelling during the heating stage of the droplet lifetime occurs due to the significant reduction of the volumetric average liquid density, as indicated by curve C of Fig. 5. An examination of the evaporation mass flux from the gas/liquid interface showed that this flux remains consistently positive, thus proving no possibility of condensation of vapor-phase species on the droplet surface. The above results clearly suggest the dominance of thermal expansion over liquid-component evaporation during the droplet heating stage of the base-case simulation. As shown on Fig. 5, droplet thermal expansion, which persists through a significant portion of the droplet lifetime, eventually ceases when vaporization becomes very intense due to substantially higher liquid temperatures.

The results obtained from the base-case calculation were used as a reference for the evaluation of various factors affecting thermal swelling of bicomponent liquid-hydrocarbon droplets vaporizing in high-temperature convective environments. The effects of ambient and initial droplet temperatures were investigated through two additional simulations, one with a lower ambient temperature ($T_\infty = 800$ K), and another with an initially uniform liquid temperature of $T_0 = 340$ K (pre-heated droplet). All other initial gas and liquid-phase variables were identical to those employed in the base-case calculation (Table 1). Figures 6 and 7 display the temporal variations of mass evaporation rates, surface-averaged temperatures, droplet diameter square, and liquid mass for all three droplets compared herein. The mass evaporation rates were normalized with respect to $\rho_{\infty} a_0^2 U_{\infty,0}$, the temperatures with respect to 350 K, while the droplet diameters and mass with respect to their initial values. As expected, the droplet temperatures for the lower ambient temperature case (T_∞=800 K) remain substantially lower than those corresponding to the other two simulations where T_∞=1250 K. The liquid temperatures of the pre-heated droplet are naturally higher than those corresponding to the base-case simulation, especially during the initial stages of the calculation when vaporization is not very intense. The mass evaporation rate of the pre-heated droplet appears to be displaced to earlier times with respect to that of the base-case simulation, while the evaporation rate corresponding to lower ambient temperatures remains substantially lower than that of the base-case simulation. It is worth noting that for all three simulations considered herein, the mass evaporation rate attains a maximum value that corresponds to an instant when approximately 30% of the liquid mass has vaporized. From the three droplets considered herein, the pre-heated droplet vaporizes faster than the other two, as indicated by the consistently lower values of liquid mass available for evaporation. The time variation of the corresponding droplet diameters on Fig. 7 shows that the magnitude of thermal expansion of the n-octane/benzene droplet is not affected by ambient temperature, even though the expansion period appears to be lengthened by lower ambient temperatures. On the contrary, the pre-heated droplet shows very little thermal expansion, as a direct result of the raised liquid temperatures that cause substantially higher vaporization rates at the early stages of the heating period. As also seen in Fig. 7, the applicability of d^2-law appears to be valid only during the later stages of a droplet lifetime. The above results also suggest that the outcome of the intense competition between thermal expansion and liquid-component evaporation depends on both initial droplet temperature and ambient conditions. Other parameters affecting this competition include the strength of the convective stream, initial droplet composition, etc.

Droplet thermal expansion has also been reported previously by other investigators. Law (1982) reported that for a sufficiently high-boiling point fuel, thermal expansion

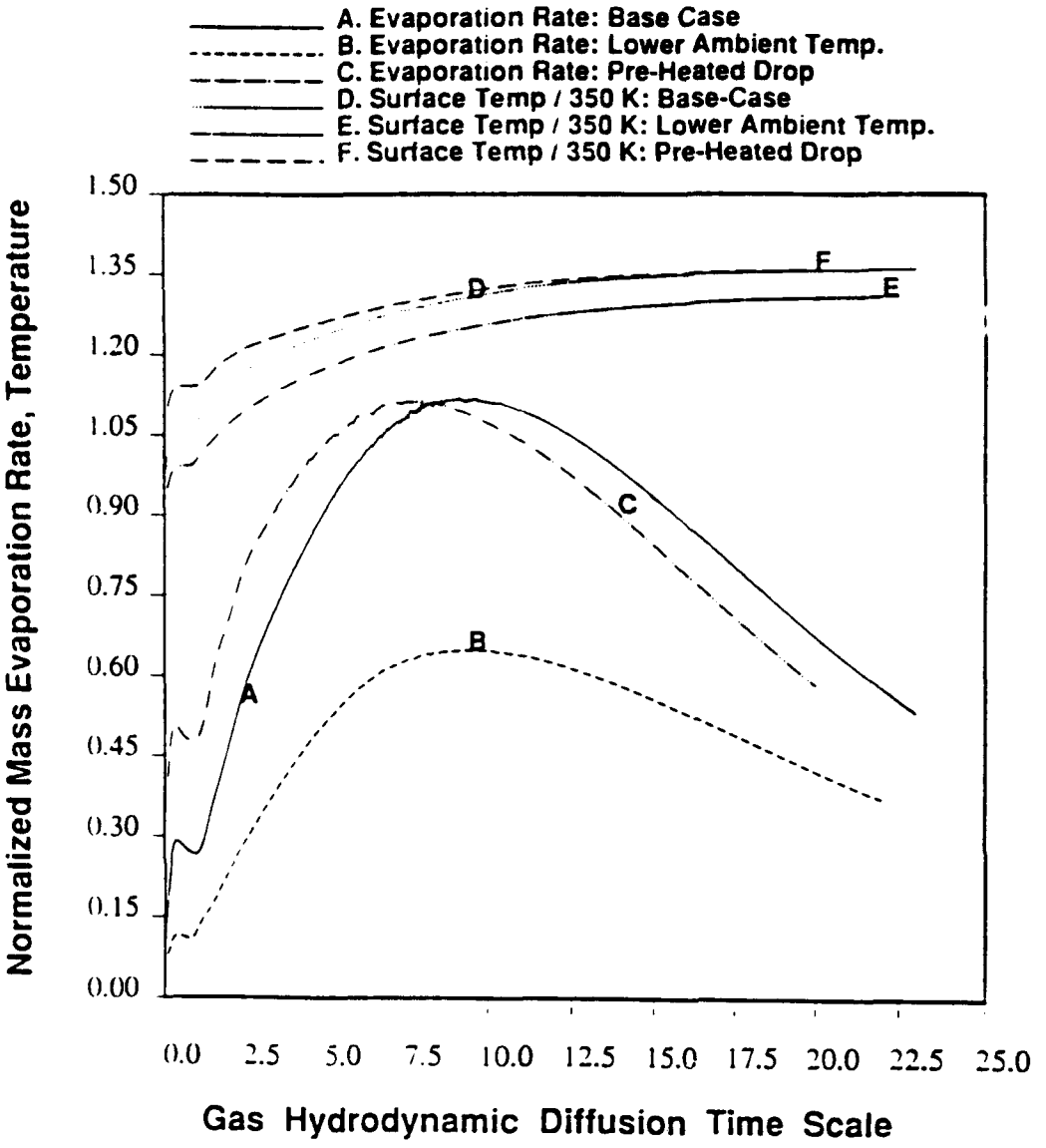

FIGURE 6 Timewise variation of normalized mass evaporation rates and surface averaged droplet temperatures for three different simulations: Base-case calculation (initial droplet temperature T_o = 300 K, free-stream temperature T_∞ = 1250 K); Lower ambient temperature calculation (T_∞ = 800 K); Pre-heated droplet calculation (T_o = 340 K).

of the liquid can actually cause the droplet to exceed its initial size. However, no experimental or theoretical verification was given in that work. Nguyen and Avedisian (1987) theoretically examined the evaporation of a spherical n-heptane droplet in the vicinity of a hot wall, and reported early droplet swelling that was attributed to liquid density variations with temperature. Renksizbulut and Haywood (1988) reported droplet volume increase during the convective evaporation of n-heptane droplets in their own vapor. However, the larger sizes of the droplet were also accompanied by a mass increase that was attributed to vapor condensation on the droplet surface. Chiang and Sirignano (1991) have also observed droplet thermal expansion during the heating stage in their

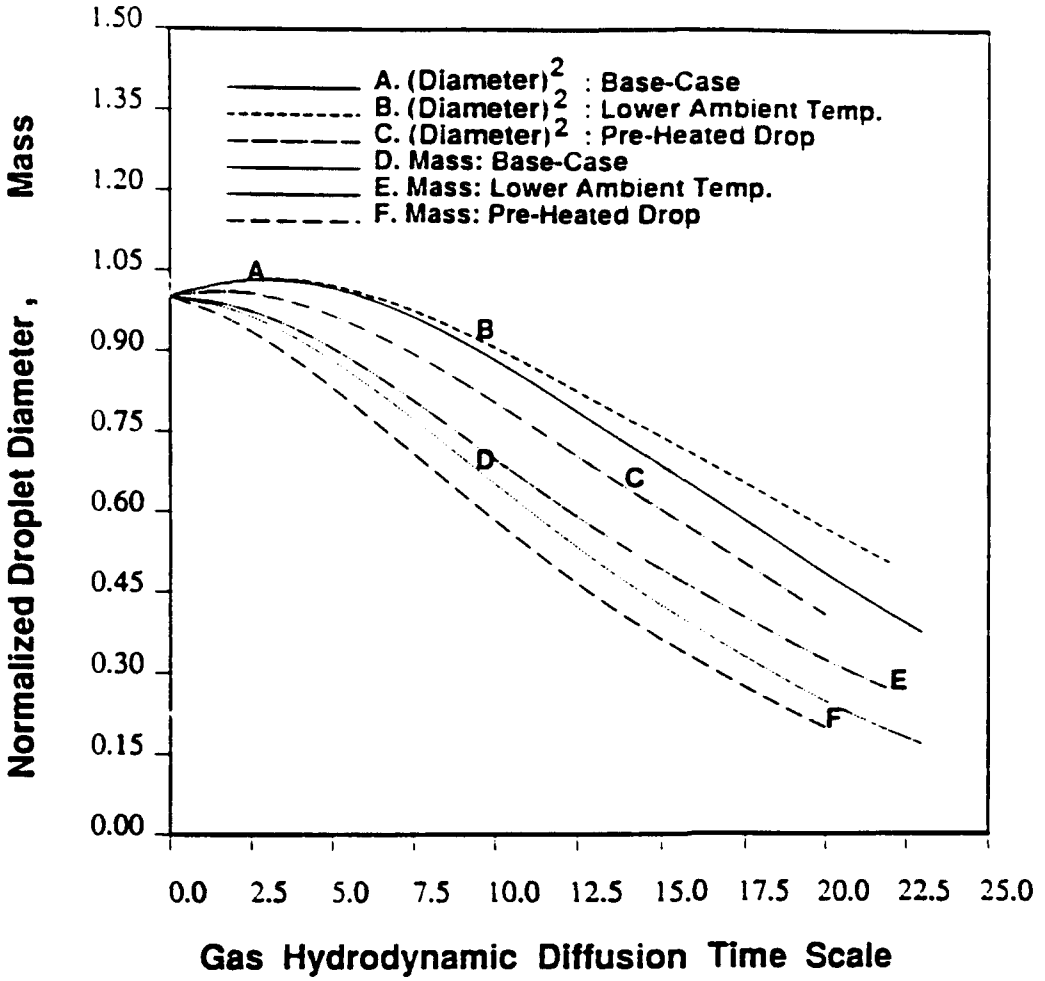

FIGURE 7 Timewise variation of normalized droplet diameter square and mass for three different simulations: Base-case calculation; Lower ambient temperature calculation; Pre-heated droplet calculation.

studies of convective vaporization of liquid oxygen droplets. Finally, Hanlon and Melton (1992) reported droplet swelling of the order of 14% for hexadecane droplets free-falling in an ambient of 500° C. In all the above studies, the droplet thermal expansion reported was of the same order of magnitude as that observed in the current work.

The above findings emphasize the belief that droplet heating is a primary source of unsteady behavior in spray dynamics. The influence of droplet thermal swelling on liquid vaporization rates (and thus on the droplet lifetime) is examined below, along with the effects of the temperature variation of liquid heat capacities. Two additional simulations were performed for this purpose: One employing temperature-independent liquid densities with temperature-dependent liquid heat capacities, and another, where both liquid densities and heat capacities were temperature independent (values corresponding to initial droplet temperature; 300 K).

Figure 8 displays the time variation of Reynolds numbers based on droplet diameter, free stream thermophysical properties and relative velocity between droplet and free stream for the three droplet simulations mentioned above. The monotonically decreasing values of Re with time indicate the relative deceleration of the droplet with respect to

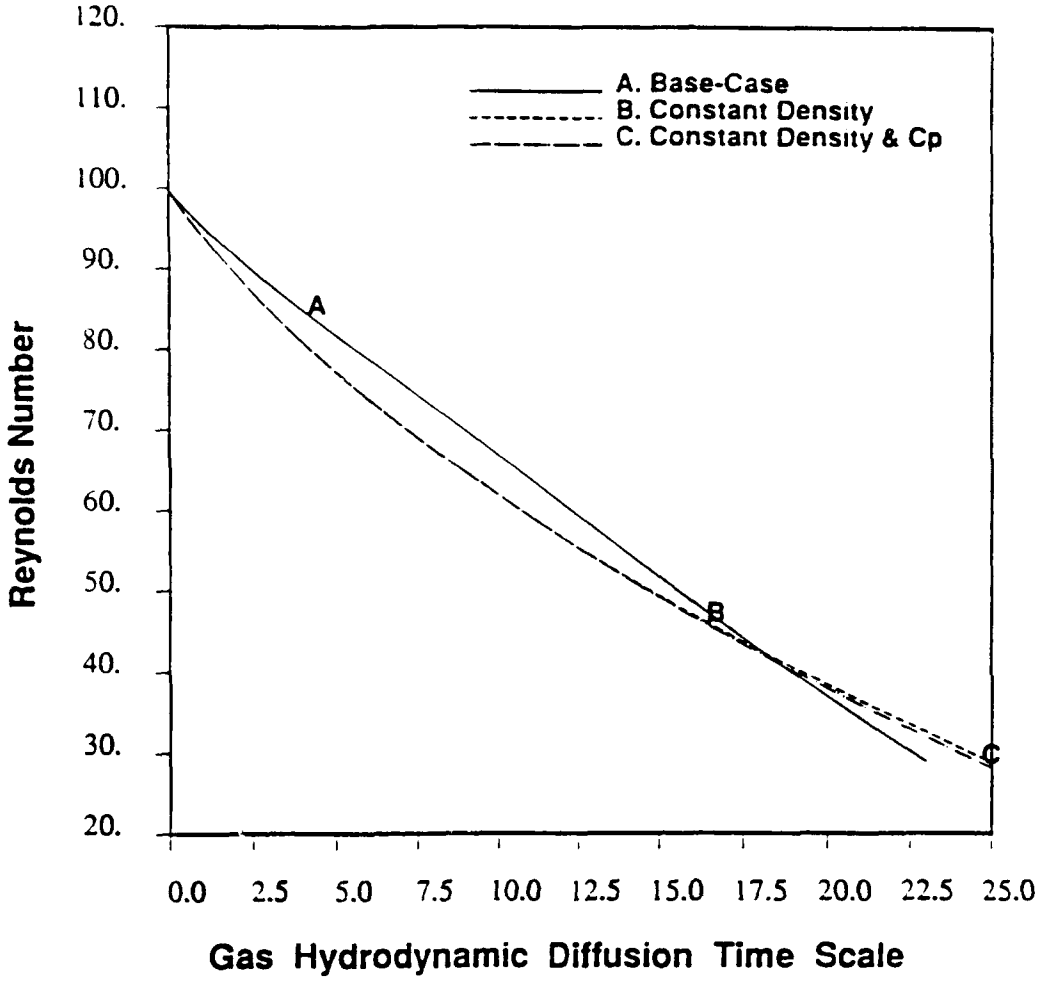

FIGURE 8 Timewise variation of Reynolds number for three different simulations: (A) Base-case calculation, (B) Calculation with temperature-independent liquid densities, and (C) Calculation with temperature-independent liquid densities and heat capacities.

the free stream. Even though the base-case droplet swells during the heating stage, the associated Reynolds number still maintains a descending character, obviously suggesting that droplet thermal expansion is not strong enough to counteract the steady deceleration of the droplet with respect to the free stream. As a result of thermal expansion, the values of Re for the expanding droplet are consistently higher than those of the non-swelling droplets, with the exception of the very late stages of the drop lifetime. The higher values of Re for the base case result in higher heat and mass transport rates, as indicated by Fig. 9 which shows the time variation of mass evaporation rates (normalized with respect to $\rho_\infty a_0^2 U_{\infty,0}$) and surface-averaged temperatures (normalized with respect to 350 K). It is apparent that temperature dependence of liquid heat capacities alone does not change the results in a significant manner (compare curves B, C as well as E and F). On the contrary, the consideration of temperature-dependent liquid densities results in substantially higher droplet temperatures that cause significantly higher evaporation rates. Figure 10 shows the time variation of drop diameter square, and droplet mass (both normalized with respect to their initial values). As seen in that figure, temperature dependence of liquid heat

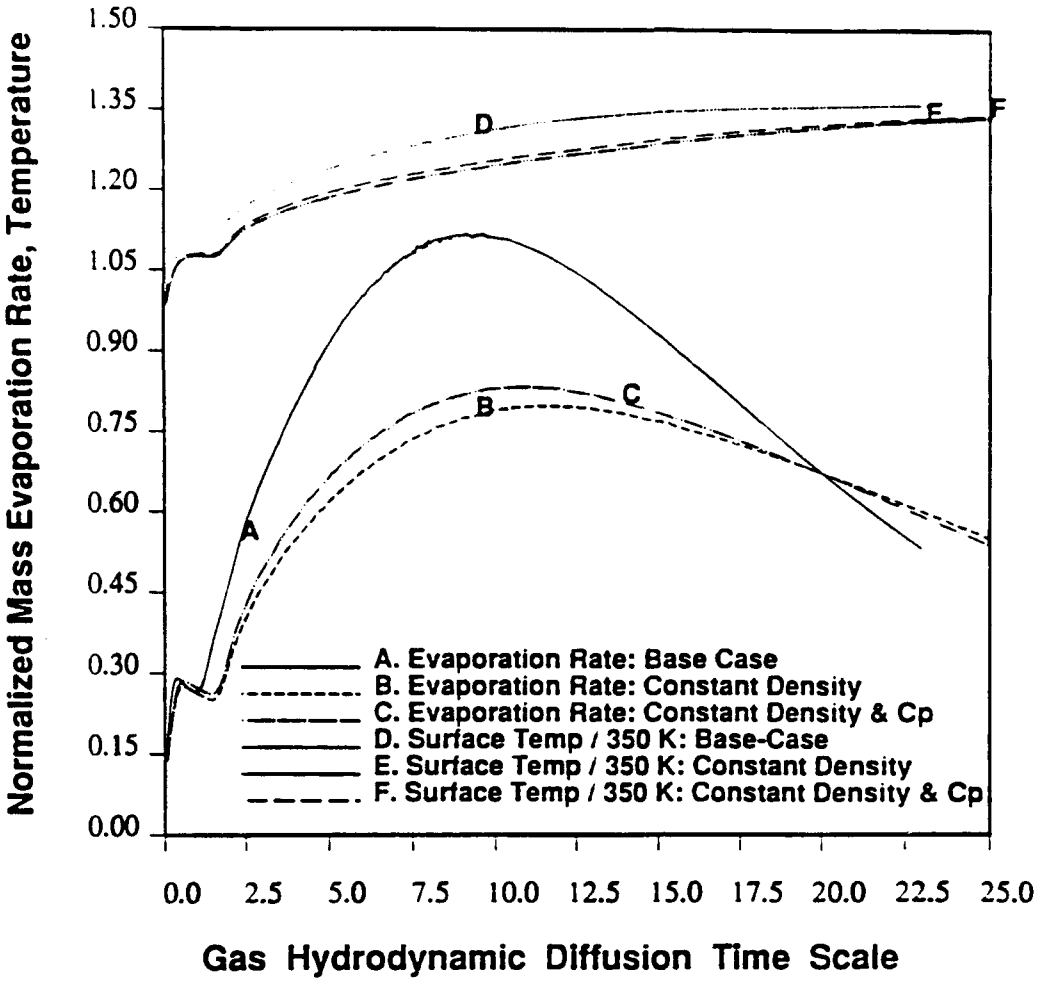

FIGURE 9 Timewise variation of normalized mass evaporation rates and surface-averaged droplet temperatures for three different simulations: Base-case calculation; Calculation with temperature-independent liquid densities; Calculation with temperature-independent liquid densities and heat capacities.

capacities alone does not alter the droplet lifetime by an appreciable amount. However, consideration of liquid density variation with temperature effectively reduces the droplet lifetime (almost by 25% at the conditions investigated herein). The above observations emphasize the importance of liquid-phase density variations with temperature in the modeling of droplet vaporization within high-temperature convective environments.

CONCLUSIONS

The present investigation extends the work of Megaridis and Sirignano (1990) on a spherical, multicomponent vaporizing droplet that is suddenly exposed to a uniform, high-temperature gaseous stream. The model accounts for variable liquid-phase thermophysical properties and has resolved previously reported numerical problems regarding the liquid concentration fields during the early stages of the numerical simulations. Detailed data on the temporal and spatial variation of the liquid-phase concentration fields throughout the lifetime of a n-octane/benzene droplet provide new insight on the

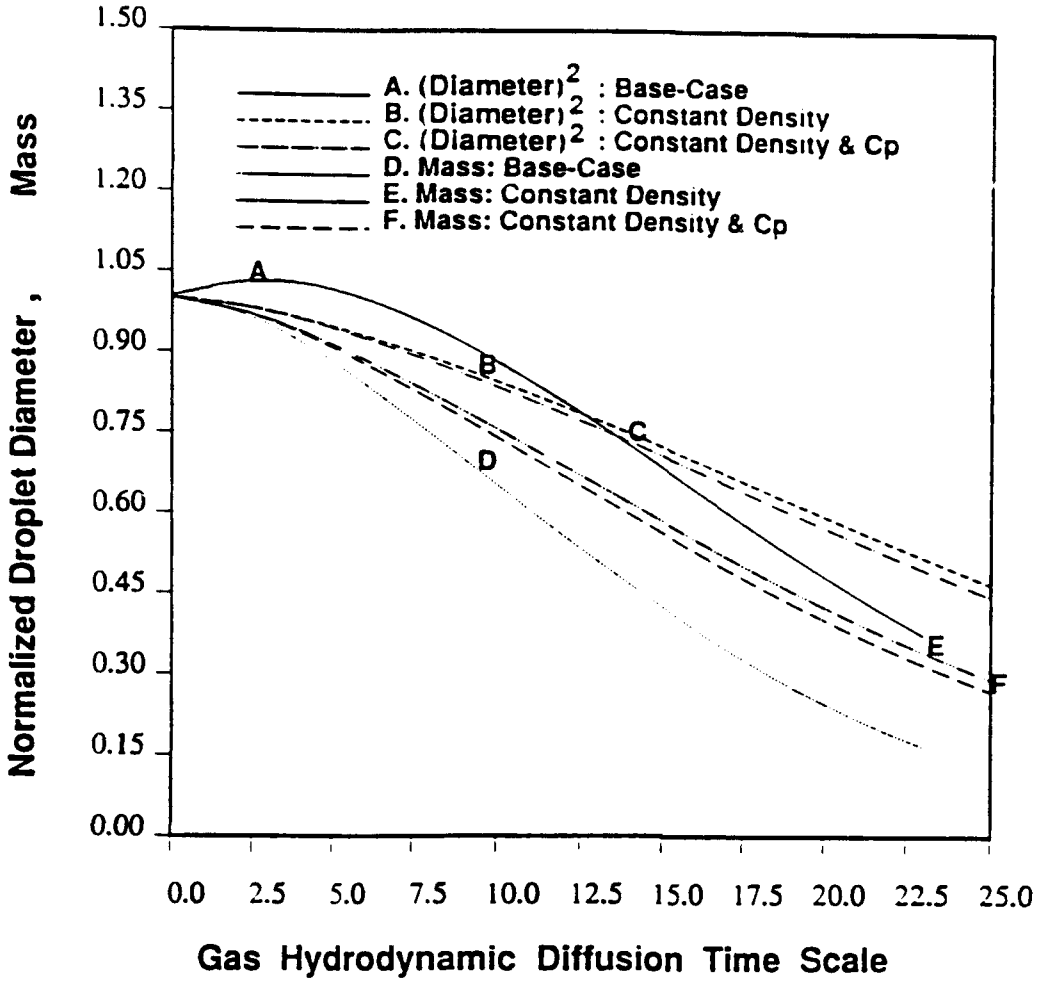

FIGURE 10 Timewise variation of normalized droplet diameter square and mass for three different simulations: Base-case calculation; Calculation with temperature-independent liquid densities: Calculation with temperature-independent liquid densities and heat capacities.

liquid mass-transport mechanisms within typical vaporizing hydrocarbon droplets. It was found that overall mass evaporation rates from a bicomponent droplet surface show an increasing trend during the early stages and achieve a temporal maximum near the droplet half-life point. The evaporation rates decrease monotonically thereafter, as the more volatile species is gradually depleted from the droplet interior. Droplet thermal expansion occurred under certain conditions as a result of the substantial reduction of liquid-phase densities during the heating stage of the droplet lifetime. The model predictions also showed that when droplet swelling occurs, it is generally limited, causing only small deviations from the initial droplet volume. However, the consideration of temperature-dependent liquid densities effectively enhanced liquid mass evaporation rates, which in turn reduced the droplet lifetime by as much as 25% under the conditions investigated in this study. In addition, the model predictions showed that the classical d^2-law for liquid droplet evaporation is not valid for a substantial portion of the droplet lifetime, especially during the heating stage of the liquid. In general, our bicomponent droplet simulations indicated that the variation of liquid densities with temperature must

be taken into account for an adequate representation of the transport processes in droplet convective vaporization. Finally, the effect of the variation of liquid heat capacities with temperature proved to be rather minor, thus suggesting that a concentration dependent approach is adequate for most practical applications.

ACKNOWLEDGEMENT

This work was partially supported by the Air Force Office of Scientific Research, Air Force Systems Command, USAF, under grant number AFOSR 92-J-0476. The author also acknowledges useful discussions with Prof. C. T. Avedisian of Cornell University during the early stages of this study.

REFERENCES

Abramzon, B., and Sirignano, W. A. (1987). Approximate theory of a single droplet vaporization in a convective field: Effects of variable properties, Stefan flow and transient liquid heating. *Proc. 2nd ASME-JSME Thermal Engng Joint Conf.*, Honolulu, Vol. 1, p. 11.

Bird, R. B., Stewart, W. E., and Lightfoot, E. N., (1960), *Transport Phenomena*, John Wiley & Sons, New York, NY.

Chiang, C. H., Raju, M. S. and Sirignano, W. A. (1992). Numerical analysis of convecting, vaporizing fuel droplet with variable properties. *Int. J. Heat Mass Transfer* **35**, 1307.

Chiang, C. H., and Sirignano, W. A. (1990). Numerical analysis of interacting, convecting, vaporizing, fuel droplets with variable properties. Paper 90-0357 presented at the *28th Aerospace Sciences Meeting*, Reno, Nevada.

Chiang, C. H., and Sirignano, W. A. (1991). Personal Communication.

Delplanque, J.-P., Rangel, R. H., and Sirignano, W. A. (1990). Liquid-waste incineration in a parallel-stream configuration: Parametric study. *Twenty-Third Symposium (International) on Combustion*, The Combustion Institute, p. 887.

Dwyer, H. A. (1989). Calculations of droplet dynamics in high temperature environments. *Prog. Energy Combust. Sci.* **15**, 131.

Faeth, G. M. (1983). Evaporation and combustion of sprays. *Prog. Energy Combust. Sci.* **9**, 1.

Gallant, R. W., (1968), *Physical Properties of Hydrocarbons*, Vol. 1, Gulf Publishing Co., Houston, Texas.

Hanlon, T. R., and Melton, L. A. (1992). Exciplex fluorescence thermometry of falling hexadecane droplets. *Journal of Heat Transfer* **114**, 450.

Haywood, R. J., Nafziger, R., and Renksizbulut, M. (1989). A detailed examination of gas and liquid phase transient processes in convective droplet evaporation. *Journal of Heat Transfer* **111**, 495.

Law, C. K. (1982). Recent advances in droplet vaporization and combustion. *Prog. Energy Combust. Sci.* **8**, 171.

Megaridis, C. M., and Sirignano, W. A. (1990). Numerical modeling of a vaporizing multicomponent droplet. *Twenty-Third Symposium (International) on Combustion*, The Combustion Institute, p. 1413.

Megaridis, C. M. and Sirignano, W. A. (1992). Multicomponent droplet vaporization in a laminar convective environment. *Combust. Sci. and Tech.* **87**, 27.

Nguyen, T. K., and Avedisian, C. T. (1987). Numerical solution for film evaporation of a spherical liquid droplet on an isothermal and adiabatic surface. *Int. J. Heat Mass Transfer* **30**, 1497.

Presser, C., Gupta, A. K., Avedisian, C. T., and Semerjian, H. G. (1990). Fuel property effects on the structure of spray flames. *Twenty-third Symposium (International) on Combustion*, The Combustion Institute, p. 1361.

Raju, M. S., and Sirignano, W. A. (1990). Interaction between two vaporizing droplets in an intermediate Reynolds number flow. *Phys. Fluids A* **2**, 1780.

Rangel, R. H., and Sirignano, W. A. (1986). Rapid vaporization and heating of two parallel fuel droplet streams. *Twenty-first Symposium (International) on Combustion*, The Combustion Institute, p. 617.

Reid, R. C., Prausnitz, J. M., and Poling, B. E., (1987), *The Properties of Gases and Liquids*, 4th ed., McGraw-Hill, New York, NY.

Reid, R. C., Prausnitz, J. M., and Sherwood, T. K., (1977), *The Properties of Gases and Liquids*, McGraw-Hill, New York, NY.

Renksizbulut, M., and Haywood, R. J. (1988). Transient droplet evaporation with variable properties and internal circulation at intermediate Reynolds numbers. *Int. J. Multiphase Flow* **14**, 189.

Rotunno, A. A., Winter, M., Dobbs, G. M., and Melton, L. A. (1990). Direct calibration procedures for exciplex-based vapor/liquid visualization of fuel sprays. *Combust. Sci. and Tech.* **71**, 247.

Sangiovanni, J. J., and Kesten, A. S. (1976). Effect of droplet interaction on ignition in monodispersed droplet streams. *Sixteenth Symposium (International) on Combustion*, The Combustion Institute, p. 577.

Shih, T.-M. and Megaridis, C. M. (1993). Finite-difference discretization effects on multidimensional droplet evaporation modeling. *Numerical Heat Transfer*, in press.

Sirignano, W. A. (1983). Fuel droplet vaporization and spray combustion theory. *Prog. Energy Combust. Sci.* 9, 291.

Svehla, R. A. (1962). Estimated Viscosities and Thermal Conductivities of Gases at High Temperatures. NASA Technical Report R-132.

Vargaftik, N. B., (1975). *Tables on the Thermophysical Properties of Liquids and Gases*, 2nd ed., Hemisphere, Washington.

White, F. M., (1974). *Viscous Fluid Flow*, McGraw-Hill, New York, NY.

APPENDIX: FLUID THERMOPHYSICAL PROPERTIES

The physical properties of the air/vapor mixture surrounding the vaporizing droplet were calculated using standard mixing rules involving the properties of the three gaseous components (air, n-octane, benzene). The inverse density of the mixture was correlated by the mass-fraction weighted average of the inverse densities of the gaseous components. In addition, the mixture heat capacity was calculated by a mass-fraction weighted rule, while the dynamic viscosity of the mixture was determined by Wilke's formula (Reid et al. 1977). Finally, the thermal conductivity of the gas mixture was estimated using Mason and Saxena's modification of the Wassiljewa conductivity expression (Reid et al. 1977).

The properties of the fuel vapors and air were approximated as functions of temperature (in degrees K). For n-octane vapor (molecular weight 114.22 kg/kmol) the following correlations were used (Abramzon and Sirignano, 1987): dynamic viscosity:

$$\mu_v^{C_8H_{18}} = 5.6 \times 10^{-6} + 1.75 \times 10^{-8}(T - 300) \quad [kg/m/s]$$

thermal conductivity:

$$k_v^{C_8H_{18}} = 4.7 \times 10^{-7} T^{1.8} \quad [W/m/K]$$

heat capacity:

$$C_{p_v}^{C_8H_{18}} = 106.6 + 5.76T - 1.67 \times 10^{-3}T^2 - 4.73 \times 10^{-7}T^3 \quad [J/kg/K];\ T < 800K$$

and

$$C_{p_v}^{C_8H_{18}} = 410.9 + 5.46T - 2.48 \times 10^{-3}T^2 + 4.23 \times 10^{-7}T^3 \quad [J/kg/K];\ T \geq 800K$$

The temperature dependence of mass diffusion coefficient of n-octane vapor in air was calculated using the Chapman-Enskog formula (Bird et al. 1960):

$$D_{C_8H_{18}\text{-}Air} = 2.96 \times 10^{-11} T^{1.738} \quad [m^2/s]$$

For benzene vapor (molecular weight 78.11 kg/kmol) the following correlations were used: dynamic viscosity (Svehla, 1962):

$$\mu_v^{C_6H_6} = \frac{1.08 \times 10^{-6} T^{1.5}}{T + 447.9} \quad [kg/m/s]$$

thermal conductivity (Svehla, 1962):

$$k_v^{C_6H_6} = 3.49 \times 10^{-6} T^{1.456} \quad [W/m/K]$$

heat capacity (Reid et al. 1977):

$$C_p^{C_6H_6} = -433.9 + 6.07T - 3.86 \times 10^{-3}T^2 + 9.12 \times 10^{-7}T^3 \quad [J/kg/K]$$

The temperature dependence of mass diffusion coefficient of benzene vapor in air was calculated using the Chapman-Enskog formula (Bird et al. 1960):

$$D_{C_6H_6,Air} = 3.69 \times 10^{-11}T^{1.772} \quad [m^2/s]$$

The mass diffusion coefficient of benzene in n-octane vapor was also calculated in a similar fashion:

$$D_{C_6H_6,C_8H_{18}} = 4.97 \times 10^{-12}T^{1.88} \quad [m^2/s]$$

For air (molecular weight 28.96 kg/kmol) the following correlations were used: Sutherland law for dynamic viscosity (White, 1974):

$$\mu_{air} = \frac{1.46 \times 10^{-6}T^{1.5}}{T + 110.6} \quad [kg/m/s]$$

Sutherland law for thermal conductivity (White, 1974):

$$k_{air} = \frac{2.5 \times 10^{-3}T^{1.5}}{T + 194.4} \quad [W/m/K]$$

heat capacity (Abramzon and Sirignano, 1987):

$$C_{p_{air}} = 1008[J/kg/K] \quad ; T < 400K$$

and

$$C_{p_{air}} = 920.5 + 0.218T \quad [J/kg/K] \quad ; T \geq 400K$$

Assuming that the two liquid components (n-octane, benzene) are fully miscible, the physical properties in the droplet interior were calculated using standard mixing rules involving the properties of the components. The inverse density of the liquid mixture was correlated by the mass-fraction weighted average of the inverse densities of the two components. In addition, the mixture heat capacity and thermal conductivity were calculated by a mass-fraction weighted rule, while its dynamic viscosity was determined by a mole fraction weighted average of the natural logarithms of the dynamic viscosities of the components (Reid et al. 1977).

For liquid n-octane the following values and correlations were used: density (Gallant, 1968):

$$\rho_l^{C_8H_{18}} = 906 - 0.7T \quad [kg/m^3]$$

dynamic viscosity (Reid et al. 1977):

$$\mu_l^{C_8H_{18}} = 13.1 \times 10^{-6}exp(1090.7/T) \quad [kg/m/s]$$

heat capacity (Gallant, 1968):

$$C_{pl}^{C_8H_{18}} = 2629.2 - 5.29T + 1.31 \times 10^{-2}T^2 \quad [J/kg/K]$$

For liquid benzene the following values and correlations were used: density (Vargaftik, 1975):

$$\rho_l^{C_8H_8} = 1145. - 0.88T \quad [kg/m^3]$$

dynamic viscosity (Reid et al. 1977):

$$\mu_l^{C_8H_8} = 8.78 \times 10^{-6} exp(1256.4/T) \quad [kg/m/s]$$

heat capacity (Vargaftik, 1975):

$$C_{pl_i}^{C_8H_8} = 2092. - 4.69T + 1.16 \times 10^{-2}T^2 \quad [J/kg/K]$$

The thermal conductivities of both liquid species were evaluated using the following expression (Reid et al. 1977):

$$K_l^i = \frac{1.1}{\sqrt{M_i}} \frac{3 + 20(1 - T/T_{ci})^{2/3}}{3 + 20(1 - T_{b.n_i}/T_{ci})^{2/3}} \quad [W/m/K]$$

where M_i is the molecular weight (kg/kmol) of liquid component i. The normal boiling points ($T_{b.n_i}$) of n-octane and benzene are 398.81 K and 353.3 K, respectively. The critical points (T_{ci}) of n-octane and benzene are 569.4 K and 562.1 K, respectively. It is important to note that the boiling points of both liquids are significantly higher at 10 atm, the pressure at which the above simulations have been performed (511 K for n-octane; 451.6 K for benzene).

The liquid-phase mass diffusivities were evaluated (according to Reid et al. 1987) by a mole-fraction weighted average of the corresponding binary diffusion coefficients at infinite dilution ($D_{i,j}^0$ denotes diffusion of traces of species i into j)

$$D_{i,j}^0 = \frac{7.4 \times 10^{-15} T \sqrt{M_j}}{\mu_j V_i^{0.6}} \quad [m^2/s]$$

where M_j, μ_j respectively denote molecular weight (kg/kmol) and viscosity (kg/m/s) of the solvent j, and V_i the molar volume (cm^3/mol) of solute i at its normal boiling temperature. The corresponding values of V_i (188.8 cm^3/mol, 96.4 cm^3/mol for n-octane and benzene, respectively) were evaluated by the Tyn and Calus expression (Reid et al. 1987).

The temperature variation of the latent heat of vaporization of each liquid component is given by (Abramzon and Sirignano, 1987)

$$L_i = L_{b.n_i} \left(\frac{T_{ci} - T}{T_{ci} - T_{b.n_i}} \right)^{0.38}$$

where T_{ci} is the critical temperature and $T_{b.n_i}$ the normal boiling point of liquid species i. The values of the heat of vaporization $L_{b.n}$ for n-octane and benzene at their normal boiling points are 301.3 kJ/kg and 393.8 kJ/kg, respectively.

APPENDIX C

Comparison Between Experimental Measurements and Numerical Predictions of Internal Temperature Distributions of a Droplet Vaporizing under High-Temperature Convective Conditions

CONSTANTINE M. MEGARIDIS
Department of Mechanical Engineering, The University of Illinois at Chicago, Chicago, IL 60680

The current study uses the data produced in a recent experimental investigation to evaluate and validate the methods employed in a detailed numerical model that simulates liquid–fuel droplet vaporization in a high-temperature, laminar, convective environment. The experimental study, which produced vaporization rates and internal temperature distributions of large, hydrocarbon, suspended droplets vaporizing at atmospheric pressure, involves Reynolds numbers up to 100, representative of practical situations of interest. A series of comparisons is performed between model predictions and experimentally measured relevant quantities. The agreement between experiment and theory on the temporal variation of certain temperatures in the droplet interior is favorable. The model predicts slightly higher vaporization rates, as indicated by lower values of the droplet diameter at corresponding instances of the droplet lifetime. The predicted temperature distributions in the droplet interior are also in good agreement with those measured experimentally throughout the droplet lifetime. To this end, both experiments and modeling agree on the establishment of internal circulation in liquid droplets exposed to laminar, high-temperature, gaseous flows. Agreement is also established on the relative insensitivity of the droplet temperature distributions when a considerable increase of free-stream momentum occurs. On the other hand, even though the model predictions show that substantially increased liquid viscosities do slow down the establishment of the liquid-phase motion, the experimental observations conclude that substantially higher liquid viscosities eliminate the liquid-phase motion entirely. The overall agreement between model predictions and experimental measurements shows that modeling can be a reliable tool in examining liquid-droplet convective evaporation under conditions that are not easily reproduced experimentally.

NOMENCLATURE

- a instantaneous liquid-droplet radius
- c_p heat capacity at constant pressure
- d instantaneous liquid-droplet diameter
- D binary mass diffusion coefficient
- k thermal conductivity
- L latent heat of vaporization
- p pressure
- r radial cylindrical coordinate
- Re instantaneous Reynolds number based on droplet diameter
- t time
- T temperature
- U_∞ free stream velocity
- V velocity
- Y mass fraction
- z axial cylindrical coordinate

Greek Symbols

- μ dynamic viscosity
- ρ density
- ψ stream function
- ω vorticity

Subscripts

- c droplet center
- g gas
- l liquid
- n normal component
- r radial component
- v fuel vapor
- z axial component
- o initial($t = 0$)
- ∞ free stream

INTRODUCTION

The operation of a wide range of liquid-fired combustion devices, from gas turbine engines, to common household oil furnaces and large-

Published by Elsevier Science Publishing Co., Inc.
0010-2180/93/$6.00

scale thermal incinerators, is governed by remarkably similar physical laws. Fundamental studies investigating the various physical and chemical processes involved in the operation of these systems, can thus have a very significant impact on the improvement of the performance of air-breathing combustion systems. The issues related to the vaporization and combustion of spray droplets are very important in combustor design and modeling, therefore, the appropriate transport mechanisms must be adequately represented for the correct evaluation of energy and mass conversion rates, as well as overall combustor behavior. Recent knowledge on droplet vaporization and spray combustion is summarized in a series of review articles by Law [1], Faeth [2], Sirignano [3], and Dwyer [4]. A wide variety of spray combustion issues is addressed in these articles and the contributions of a large number of experimental and theoretical investigations during the past several decades are analyzed.

Since a better understanding of the transport processes in dilute spray configurations provides a substantial insight into more realistic dense spray applications, a large body of work has concentrated on individual droplets. It has been established that the transport phenomena involved in both droplet combustion and vaporization are qualitatively similar. However, since gas-phase reaction rates are substantially higher than the liquid vaporization rates under high-temperature conditions, liquid-component evaporation is the controlling process in most cases.

Classical droplet vaporization theory [5] describes a fuel droplet in a spherically symmetric gas field. The only relative motion between liquid and gas involves radial convection due to vaporization. However, in practical situations droplets travel through a combustion chamber at different velocities than the surrounding gases. Relative motion enhances heat and mass transport rates, and causes a motion of the liquid at the surface due to shear interaction between the two phases. The Reynolds number (based on droplet diameter, ambient properties, and relative velocity between liquid/gas) in most practical combustion applications rarely exceeds 100 during the droplet lifetime.

The issue of internal circulation in large, free falling, nonevaporating droplets has been fundamentally addressed by McDonald [6], and subsequently by LeClair et al. [7]. LeClair et al. [7] used seed particles and streak photography to obtain data on the particle trajectories inside the drops and thus estimated the liquid velocities in an average sense. Flow patterns were visualized inside drops with high loadings of the seed particles; therefore, some ambiguity existed with respect to the influence of the presence of large populations of solid tracers on the induced liquid motion. More recently, Winter and Melton [8] used the quenching effects of oxygen on laser-induced fluorescence from naphthalene in order to examine whether internal circulation is important in submillimiter hydrocarbon droplets. Winter and Melton used 300–500-μm-diameter decane droplets that were allowed to fall into a quiescent chamber at room temperature. Even though this work employed droplet sizes that are on the high end of the range observed in practice, it was a pioneering step towards an experimental verification of phenomena that have been long predicted by numerical models. The droplets studied by Winter and Melton [8] contained naphthalene, to produce fluorescence images of variable intensity that revealed internal circulation patterns. As the authors admitted, the liquid circulation observed in their work could be influenced (to a questionable degree) by the process of droplet injection. However, the contribution of the injection disturbance was not quantified in their work. Due to the nature of the liquid compound (decane) used in that work and the room-temperature experimental conditions, liquid-component vaporization was entirely suppressed.

A variety of detailed droplet vaporization models has been developed over the past decade, addressing the issue of internal liquid circulation and transient heating in fuel droplets exposed to high-temperature, laminar, convective environments [9–12]. Extensions of these models [13, 14] considered multicomponent droplets, and addressed issues related to liquid-phase mixing and preferential vaporization from the gas–liquid interface. Even though the above models have been very helpful in studying the fundamental transport mecha-

nisms in droplet vaporization, there exists very little experimental data that these models can be validated against. This is mainly due to the inherent difficulties encountered in investigations employing realistic liquid-fired combustion devices (insufficient instrumentation access, obscuration due to the presence of combustion generated particulates, high temperatures, turbulence, etc.). Relevant experimental investigations have produced an array of data on the temporal variation of global droplet parameters, but have produced very limited quantitative information on the temporal character of velocity and temperature fields.

The validation of a detailed numerical model requires the availability of transient, spatially resolved field data originating from reliable experimental measurements performed on a well-defined system. To this end, a recent experimental study by Wong and Lin [15] produced internal temperature distributions of large, hydrocarbon droplets that vaporize after being exposed to a 1000 K gaseous stream at atmospheric pressure. The droplets studied by Wong and Lin were of initial diameter of 2 mm, and were suspended using a thin shell-shaped probe specially designed to minimize interference to the internal liquid motion. The experimental conditions investigated correspond to Reynolds numbers between 17 and 100, that are representative of practical situations of interest. The current study uses the experimental data produced in [15] to evaluate and validate the methods employed in a recently developed numerical model by Sirignano and co-workers [12, 13]. In the following, a model simulating the experimental conditions of [15] is presented, and a series of comparisons is subsequently performed between the model predictions and the experimentally determined relevant quantities.

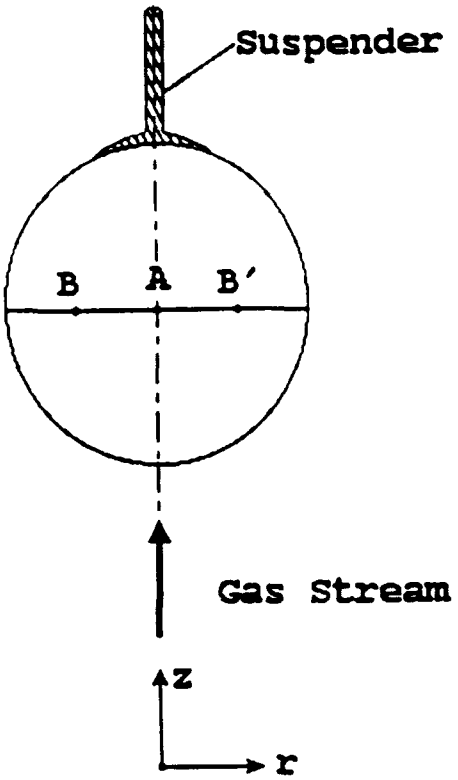

Fig. 1. Schematic of arrangement for suspended liquid-droplet convective evaporation and the applicable axisymmetric coordinate system [15].

DROPLET VAPORIZATION SETUP

The axisymmetric droplet vaporization arrangement employed by Wong and Lin [15] is depicted in Fig. 1. Individual droplets of diameter 2000 $\pm$ 50 μm were suspended on a ceramic shell suspender, which was attached to a 100-μm-diameter glass filament. According to Wong and Lin [15], this thin shell-shaped suspender caused minimum interference to the internal droplet motion. However, no information on the physical dimensions of the suspender was reported [15]. The temperature distributions within the droplet interior were measured by Wong and Lin [15] using fine thermocouples (25 μm wire diameter, 70 μm bead diameter) that were introduced and maintained in the bulk of the suspended droplets at either one or three fixed locations; the droplet center (Point A on Fig. 1), and two mutually symmetric locations with respect to the vertical axis (Points B and B' on Fig. 1). All three temperature measurement points correspond to $\theta = 90°$, where θ is the angular position with respect to the front stagnation point of the flow ($\theta = 0$). Internal droplet temperature distributions were measured along the $\theta = 90°$ line, by carefully adjusting the horizontal positions of the thermocouple beads prior to the test. The droplets were heated by a hot (1000 K) free stream produced by a flat-flame burner or an electrical heater [15]. The free stream velocity was adjusted to pro-

duce different Reynolds numbers. The full details of the experimental setup are given in Ref. 15. Three test conditions were investigated corresponding to Reynolds numbers (based on droplet diameter and free stream properties) of 17, 60, and 100. During a typical test in Ref. 15, a droplet was suddenly exposed to the hot gas stream by quickly withdrawing a protective shield. No mention was made in Ref. 15 regarding the initial establishment of the free stream flow over the suspended droplet. According to Wong and Lin's video observations, the droplets were "nearly" spherical. Two pure fuels were tested by Wong and Lin: *n*-decane and JP-10. In addition, JP-10 droplets thickened with polystyrene were employed in order to examine the effect of fuel viscosity.

MODEL DESCRIPTION

The experimental configuration, along with the appropriate axisymmetric coordinate system, is displayed in Fig. 1. This configuration was modeled by a spherical droplet that is suddenly exposed to a hot gaseous stream. The assumption of sphericity was adopted since the droplets studied by Wong and Lin [15] were characterized as "nearly spherical." The presence of the suspending fiber and the shell-type suspender was not modeled, due to limited data given in [15] with respect to their dimensions. The model assumes no internal liquid motion and a uniform temperature before the droplet is exposed to the hot stream (time = 0). The model configuration is similar to that modeled in single-component [12] and multicomponent [13] fuel droplet vaporization problems.

The current model is applicable throughout the range of Reynolds numbers applicable during the measurements reported in Ref. 15. It accounts for variable thermophysical properties and transient droplet heating with internal liquid circulation. External body forces, surface tension effects, droplet spinning and thermal radiative effects are neglected. Physically, the problem may be viewed as an impulsively started gaseous flow over a stationary droplet. The hot gas that comes in contact with the droplet surface causes the initiation of liquid-phase circulating motion as a result of shear forces. In addition, transfer of heat from the gas to the liquid causes higher droplet-surface temperatures, which spread to the droplet interior due to the establishment of the liquid motion [12]. Droplet heating amplifies liquid evaporation which causes the droplet diameter to diminish with time, thus resulting in a gradual decrease of the associated Reynolds number. All these mechanisms have been thoroughly examined and quantified by Chiang [16]; therefore, the details will not be repeated herein.

The model produces time-varying spatially resolved data for the entire flow field within and around the droplet, thus providing important information on the fundamental transport processes governing the energy and momentum exchange between the droplet and the gaseous stream. The governing equations are listed below.

Governing Equations

The following equations are expressed with respect to a reference frame that is based on the center of the liquid droplet. The gas-phase formulation is cast in primitive variables (including pressure), while a vorticity/stream function formulation is employed in the liquid phase in order to bypass the pressure calculation. In the following, the subscripts g and l indicate gas and liquid phase, respectively.

Gas Phase

The gas phase mixture of the incoming stream and the vapor was assumed to behave as an ideal gas.

Continuity Equation

$$\frac{\partial \rho_g}{\partial t} + \frac{1}{r}\frac{\partial}{\partial r}(\rho_g r V_r) + \frac{\partial}{\partial z}(\rho_g V_z) = 0. \quad (1)$$

Momentum Equation in Radial Direction

$$\frac{\partial}{\partial t}(\rho_g V_r) + \frac{1}{r}\frac{\partial}{\partial r}(\rho_g r V_r V_r) + \frac{\partial}{\partial z}(\rho_g V_z V_r) = -\frac{\partial p}{\partial r} + \Phi_r, \quad (2)$$

where Φ_r includes the relevant viscous terms [16].

Momentum Equation in Axial Direction

$$\frac{\partial}{\partial t}(\rho_g V_z) + \frac{1}{r}\frac{\partial}{\partial r}(\rho_g r V_r V_z) + \frac{\partial}{\partial z}(\rho_g V_z V_z) = -\frac{\partial p}{\partial z} + \Phi_z, \tag{3}$$

where Φ_z includes the relevant viscous terms [16].

Energy Equation. The viscous dissipation terms are neglected since velocity gradients are small. The terms associated with temporal or spatial derivatives of pressure are also neglected, since they are directly proportional to the square of the Mach number which is very low for the laminar flow conditions considered herein.

$$c_{p_g}\left\{\frac{\partial}{\partial t}(\rho_g T) + \frac{1}{r}\frac{\partial}{\partial r}(\rho_g r V_r T) + \frac{\partial}{\partial z}(\rho_g V_z T)\right\} = -\frac{1}{r}\frac{\partial}{\partial r}(r q_r) - \frac{\partial q_z}{\partial z}, \tag{4}$$

where the radial and axial components of the energy flux vector are given by the following expressions (the radiative flux effect has been neglected)

$$q_r = -\kappa_g \frac{\partial T}{\partial r}, \qquad q_z = -\kappa_g \frac{\partial T}{\partial z}.$$

Species Equation. The gaseous mixture is composed of the incoming gas and the fuel vapor. For a binary mixture

$$\frac{\partial}{\partial t}(\rho_g Y) + \frac{1}{r}\frac{\partial}{\partial r}(\rho_g r V_r Y) + \frac{\partial}{\partial z}(\rho_g V_z Y) = \frac{1}{r}\frac{\partial}{\partial r}\left(\rho_g r D \frac{\partial Y}{\partial r}\right) + \frac{\partial}{\partial z}\left(\rho_g D \frac{\partial Y}{\partial z}\right). \tag{5}$$

Liquid Phase

The continuity equation for a constant density liquid is satisfied automatically when we define the velocity components in terms of the stream function:

$$V_{l,r} = \frac{1}{r}\frac{\partial \psi}{\partial z}, \qquad V_{l,z} = -\frac{1}{r}\frac{\partial \psi}{\partial r}.$$

Vorticity Equation. Assuming low spatial variations of the liquid viscosity μ_l, the vorticity ω is governed by

$$\frac{\partial(\rho_l \omega)}{\partial t} + \frac{\partial}{\partial r}\left(\frac{\rho_l \omega}{r}\frac{\partial \psi}{\partial z}\right) - \frac{\partial}{\partial z}\left(\frac{\rho_l \omega}{r}\frac{\partial \psi}{\partial r}\right) = -\frac{\mu_l}{r^2}\omega + \frac{\mu_l}{r}\frac{\partial}{\partial r}\left(r\frac{\partial \omega}{\partial r}\right) + \mu_l \frac{\partial^2 \omega}{\partial z^2}. \tag{6}$$

Stream Function Equation

$$\frac{\partial}{\partial r}\left(\frac{1}{r}\frac{\partial \psi}{\partial r}\right) + \frac{\partial}{\partial z}\left(\frac{1}{r}\frac{\partial \psi}{\partial z}\right) = \omega. \tag{7}$$

Energy Equation

$$c_{p_l}\left\{\frac{\partial}{\partial t}(\rho_l T) + \frac{1}{r}\frac{\partial}{\partial r}\left(\rho_l \frac{\partial \psi}{\partial z} T\right) - \frac{\partial}{\partial z}\left(\frac{\rho_l}{r}\frac{\partial \psi}{\partial r} T\right)\right\} = -\frac{1}{r}\frac{\partial}{\partial r}(r q_r) - \frac{\partial q_z}{\partial z}, \tag{8}$$

where the radial and axial components of the energy flux vector are given by the following expressions (the radiative flux effect has been neglected)

$$q_r = -\kappa_l \frac{\partial T}{\partial r}, \qquad q_z = -\kappa_l \frac{\partial T}{\partial z}.$$

Initial and Boundary Conditions

The initial conditions correspond to the sudden exposure of a spherical, quiescent, liquid droplet to a uniform, high-temperature gaseous stream. The presence of the ceramic shell suspender, as well as the suspending glass

filament (Fig. 1) were not modeled due to insufficient information. The boundary conditions at the gas–liquid interface include continuity of shear stress, tangential velocity and temperature, conservation of energy and mass, and finally, phase equilibrium, as expressed by the Clausius–Clapeyron equation. Appropriate inflow/outflow conditions were applied at a distance adequately far from the droplet (eight droplet diameters [16]), while the axisymmetric nature of the flow imposed symmetry conditions that were applied on the axis of the flow. The detailed form of the above conditions can be found in Ref. 16.

NUMERICAL SOLUTION PROCEDURE

The above listed governing equations were cast in a nondimensional parameter formulation [12]. The solution of the system was performed numerically using finite-difference discretization techniques and an implicit iterative solution procedure [12, 16]. A transformation of the physical domain to a temporally invariable, rectangular, computational domain using equal spacings in both directions was employed. A modified ICE method [17] was used to calculate velocities, pressures, and densities in the gas phase. The mass conservation equation was indirectly satisfied by the pressure correction equation. The stream function and pressure correction equations were solved using the successive-over-relaxation method. The momentum, energy, and species equations in the gas phase, as well as the vorticity and energy equations in the liquid phase, were solved using an alternate direction predictor-corrector method. The nonlinear interface conditions were treated by a quasilinearization technique that determined the interface parameters, matching both gas and liquid-phase fields at each instant. The details of the numerical techniques are given in Ref. 16 and will not be repeated here. It is worth noting that in order to account for the droplet size reduction due to liquid evaporation, an adjustment of the numerical grid in both phases was necessary throughout the calculation. The widely disparate characteristic times and length scales of the transport processes involved required fine temporal and spatial resolution; therefore, the related computations were quite intensive. These computations were performed on a CRAY Y-MP supercomputer.

RESULTS AND DISCUSSION

The experimental work of Wong and Lin [15] presented data on internal temperature distributions of *n*-decane ($C_{10}H_{22}$) and JP-10 (exo-tetrahydrodicyclopentadiene) droplets at three different initial Reynolds numbers Re_0, namely 17, 60, and 100. For all cases the ambient pressure and temperature were 1 atm and 1000 K, respectively. An *n*-decane, 1961-μm-diameter droplet exposed to a free-stream velocity U_∞ = 1 m/s (Re_0 = 17) was chosen as the base case for direct comparisons of the experimental measurements with the numerical model predictions. According to the data given in Ref. 15, the *n*-decane droplet was initially quiescent and at a uniform temperature (316 K) before being exposed to the uniform gas stream generated by a flat-flame burner fueled with CO, O_2, and N_2. Since the exact composition of the combustion gases was not reported in Ref. 15, air was assumed to adequately represent the properties of the free stream. The gas and liquid thermophysical properties needed for the numerical simulations are given in the Appendix.

The computational mesh employed throughout the numerical simulations consisted of 30 (radial direction) × 31 (angular direction) nodes in the gas phase, and 30 × 31 nodes in the liquid phase. The numerical grid was uniform in the angular direction, while variable spacing in the radial (in spherical sense) direction was employed with dense packing near the droplet surface, in order to resolve the high gradients occurring in the vicinity of the gas–liquid interface. As reported in Ref. 12, the model provides a wealth of information on the temporal variation of both liquid and gas fields, gas/liquid interface quantities, and global heat and mass transport rates. Our attention will be directed mainly to the liquid-phase fields, since the data presented in Ref. 15 primarily concern the droplet interior.

Figure 2 depicts the model-predicted isothermal contours for the droplet interior at two different instants of the simulation (0.1

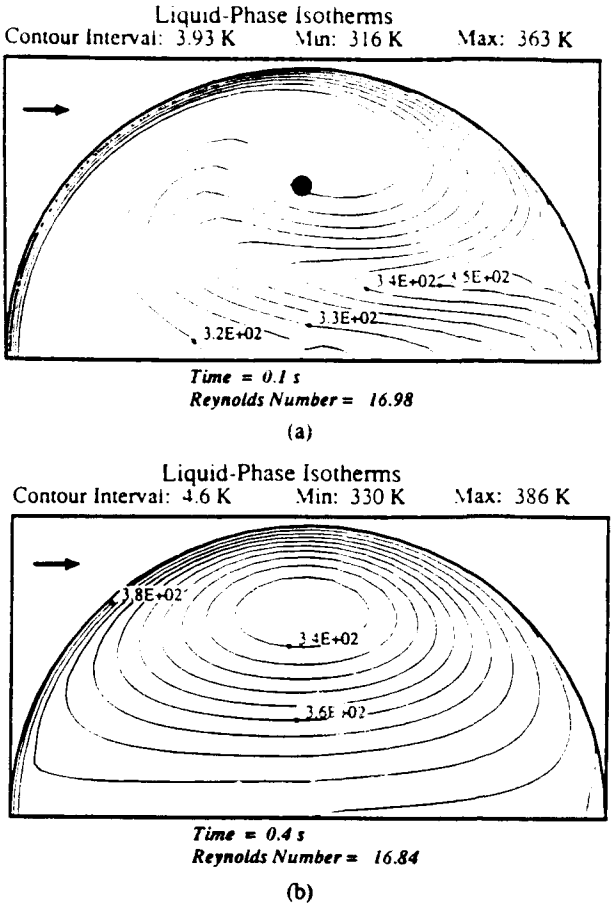

Fig. 2. Numerically predicted isothermal contours within a liquid n-decane droplet at two different instants (0.1 and 0.4 s) of the base-case simulation (Re_0 = 17, T_∞ = 1000 K). The dark circle in A depicts the relative size of a 70-μm-diameter thermocouple bead used by Wong and Lin [15]. The gaseous flow direction is indicated by the arrow.

and 0.4 s). The dark circle in Fig. 2a depicts the relative size of a 70-μm-diameter thermocouple bead used by Wong and Lin [15]. The specific location indicated by the bead corresponds to a radial location r equal to 60% of the initial droplet radius. It is worth noting that the thermocouple bead physically occupies a space in the droplet interior where liquid temperatures vary by 4–5 K; therefore, the experimental measurements cannot be characterized as point measurements in an absolute sense. It is apparent from Fig. 2 that the establishment of the liquid-phase motion due to the shear interaction between gas and liquid results in substantial temperature differences between the droplet surface and the bulk of the liquid. As also seen in Fig. 2, the higher temperatures occur on the gas–liquid interface, while lower temperatures are established early at regions off the droplet axis and at an angular location $\theta \approx 90°$ from the front stagnation point of the flow. Since the droplet vaporizes with time, the computational grid in the droplet interior is adjusted in order to conform to the regressing surface [12]. In principle, an interpolation scheme can be used to follow the temporal variation of temperature or any other quantity at a specific point within the droplet using the field data produced numerically for the neighboring grid points.

Figure 3 shows a comparison between the predicted and experimentally determined [15] temperatures at the droplet center (T_c) and a point located at an angular location $\theta = 90°$ from the front stagnation point of the flow, and a distance r equal to 60% of the initial droplet radius (bead location indicated on Fig. 2A). In fact, the off-center experimental value is the mean of the two values measured by two symmetrically positioned thermocouples at the proper locations [15]. Both experimental and numerical data agree that the temperature at the droplet center is higher than that of the off-center location throughout most of the period considered. The two sets of data also agree on the merging trend of the two temperatures (note merging of T_c and T_r values at late times on Fig. 3). The agreement between experiment and theory is excellent for the off-center position during the early and intermediate stages. Some deviation is apparent at later stages that might be attributed to the deterioration of the experimental measurements at late times, due to increasing interference from the intrusive thermocouples and the nature of the suspending probe. As seen on Fig. 3, the model predicts higher droplet center temperatures than those measured at early and intermediate stages of the droplet lifetime. This trend is reversed during the late phases of the droplet lifetime. The fair agreement between experiment and theory with respect to the temporal variation of T_c might be attributed to a slowdown of the convective transport processes resulting from the presence of the thermocouple bead at the droplet center. We should also note, that even though the predicted temperatures are leveling off at late stages, the experimental curves for T_c and T_r maintain an ascending character.

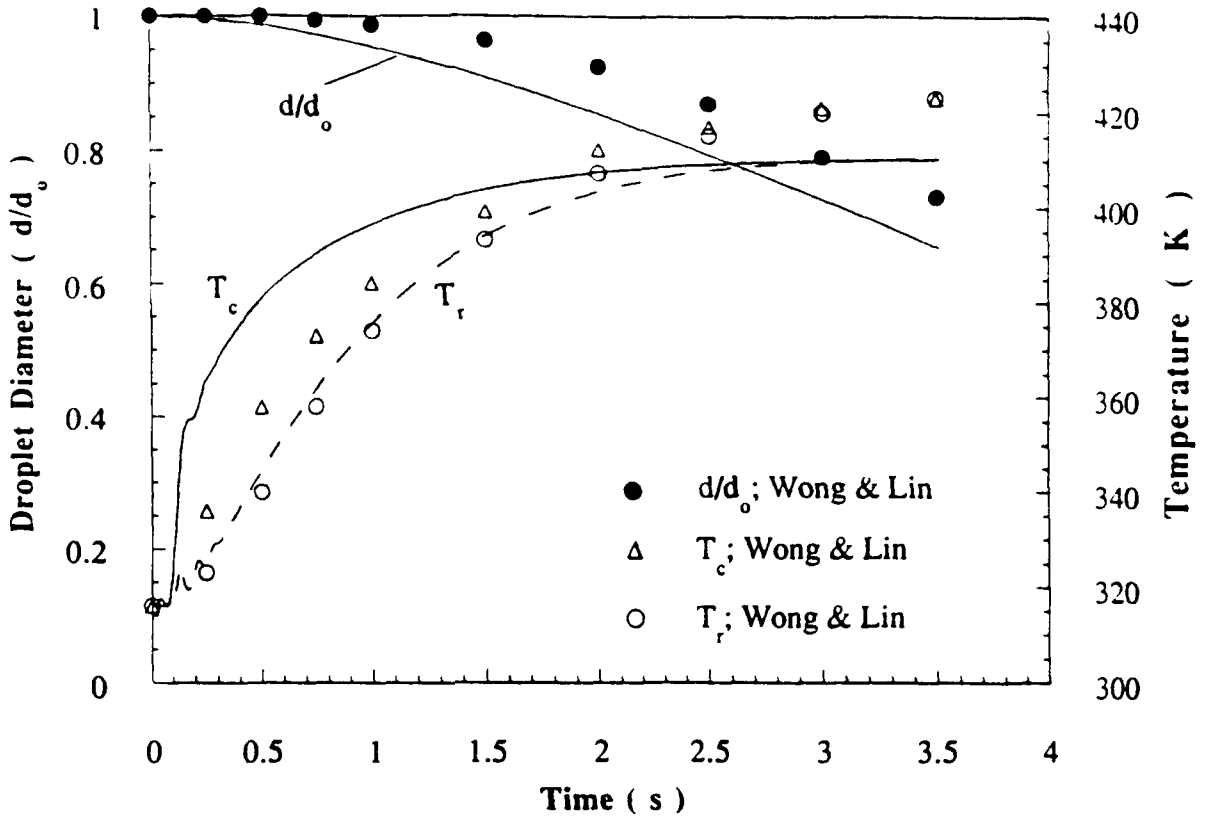

Fig. 3. Comparison between predicted (curves) and experimentally determined (symbols [15]) temperatures at the droplet center (T_c) and a point located in the droplet interior at an angular location $\theta = 90°$ from the front stagnation point of the flow, and a distance r equal to 60% of the initial droplet radius. The temporal variation of droplet diameter is displayed as well.

Figure 3 also shows the comparison between experiments and theory for the normalized droplet diameter d with respect to its initial value d_0. Since the suspended droplets examined in Ref. 15 were nearly spherical, effective droplet diameters were evaluated by Wong and Lin by approximating the particles as ellipsoids. The model-predicted droplet diameters appear to be consistently lower (up to 10%) than the measured ones. This disparity cannot be solely attributed to experimental error related to the determination of the droplet diameter, which was measured by Wong and Lin using video imaging [15]. The liquid density of *n*-decane is gradually reduced as droplet heating proceeds. In fact, a temperature rise of the order of 70 K causes a liquid-density reduction of the order of 10%. Since the numerical model adopted a constant liquid density assumption, it is expected that the rate of droplet diameter reduction is overpredicted, as clearly indicated in Fig. 3. The model predictions were used to examine the transport processes in the droplet wake in order to identify additional sources of disagreement.

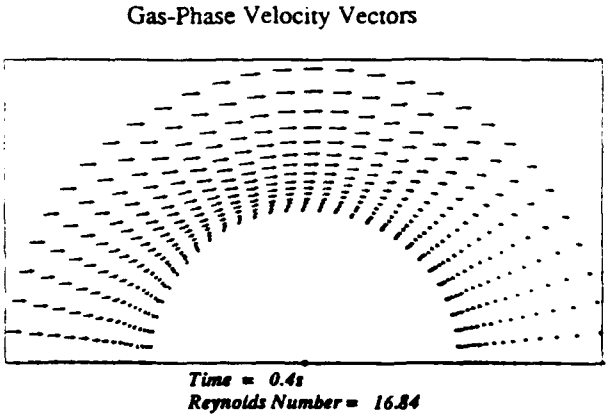

Fig. 4. Numerically predicted gaseous velocity vector field in the vicinity of the *n*-decane droplet of the base-case simulation at 0.4 s after exposure to the free stream. The droplet occupies the blank circular region contained between the arrows and the axis of symmetry.

Figure 4 depicts the model-predicted gas-phase velocity vectors in the vicinity of the

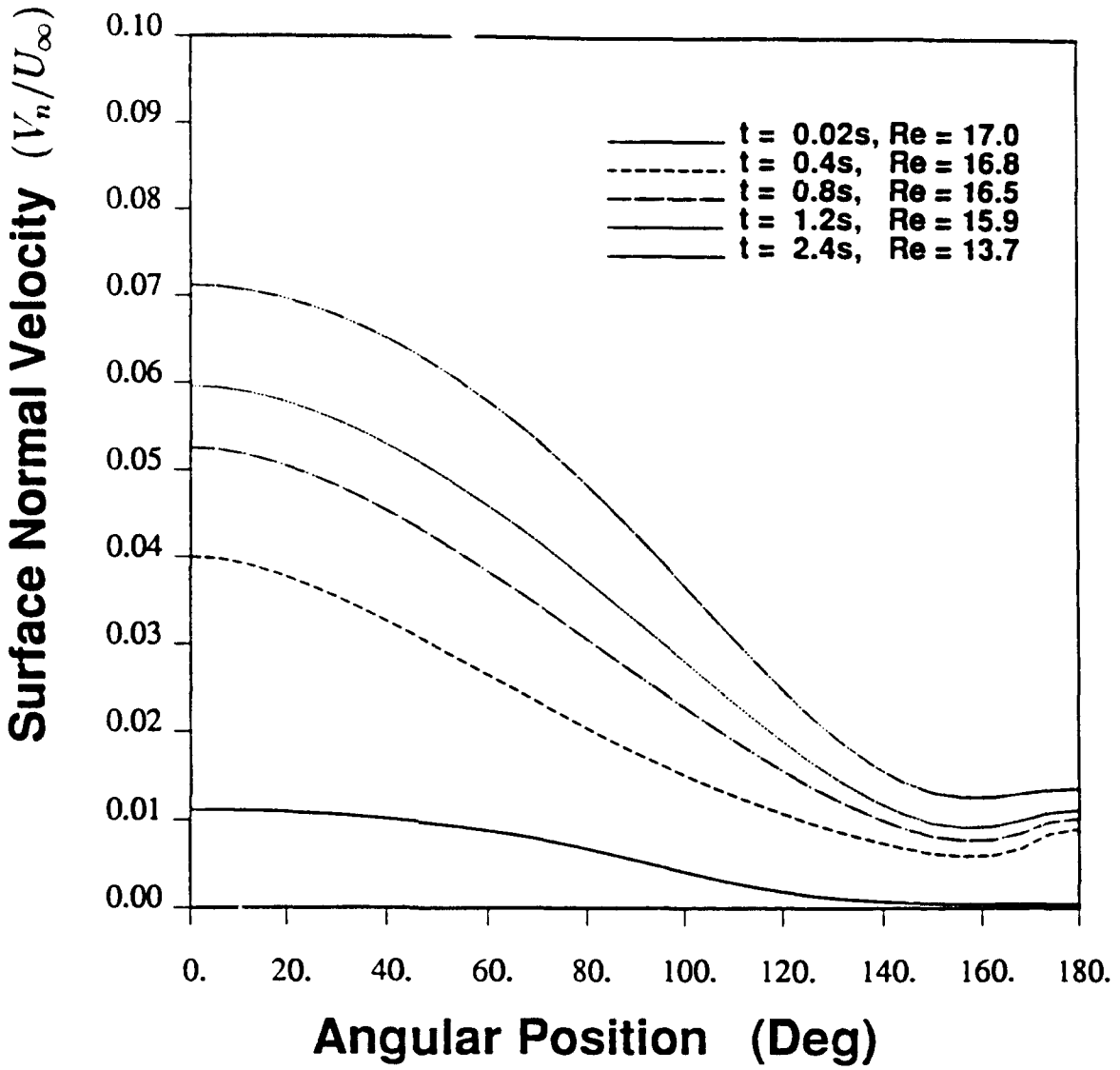

Fig. 5. Numerically predicted angular variation of normal component of the vaporization velocity over the droplet surface at five different instances of the base-case simulation (0.02 , 0.4, 0.8, 1.2, and 2.4 s). Angle zero corresponds to the front stagnation point of the flow.

vaporizing *n*-decane droplet at an instant 0.4 s after exposure of the droplet to the gas stream. The characteristic opposing flow pattern in the vicinity of the front stagnation point of the flow underlines the significance of liquid-component evaporation in the overall flow structure around the droplet [12]. As also seen in Fig. 4, no return flow region appears in the droplet wake at that instant. However, a small wake region emerged later in the simulation (approximate time 1 s), which was not attached to the droplet. The early observation of no droplet wake, according to the non-evaporating droplet study of Rivkind and Ryskin [18], is consistent with the relatively low value of the Reynolds number at that instant (Re = 16.8), and the value of liquid–gas dynamic-viscosity ratio applicable for this specific case (μ_l/μ_g = 16.4). In addition, the absence of recirculating flow in the droplet wake at early stages of the low Reynolds number simulation, underlines a difference from flows around vaporizing droplets that are characterized by higher Reynolds numbers [12, 18].

Figure 5 shows the angular variation of the normal component of the vaporization velocity V_n over the droplet surface at five different instances of the simulation; 0.02, 0.4, 0.8, 1.2, and 2.4 s. The corresponding values of the instantaneous Reynolds number Re are also

shown in Fig. 5. Since the displayed velocity values were normalized with respect to the free-stream velocity U_∞, it is apparent that as vaporization becomes more intense with droplet heating, the normal velocity component above the gas–liquid interface can attain values up to a significant percentage of the incoming (free stream) velocity. Even though vaporization is strongest in the vicinity of the front stagnation point of the flow, it is also apparent that the contribution of the droplet wake to the overall vaporization behavior of the droplet is substantial. This observation may be an additional factor responsible for the above-mentioned deviation of droplet vaporization rates between experimental measurements and model predictions. Since the experimental setup used in Ref. 15, due to the presence of the thin shell-shaped suspender (Fig. 1), suppresses liquid-component evaporation from the regions of the droplet surface near the wake; it is naturally expected that the experimentally determined diameters will be higher than the corresponding computed values at all times (trend displayed in Fig. 3).

The experimental study of Wong and Lin [15] also produced data on droplet temperature distributions with respect to time for a 2000-μm-diameter *n*-decane droplet exposed to a 1000-K gaseous stream at $Re_0 = 17$. The thermocouple measurements were performed in identical droplets over a series of radial locations (r) within the bulk of the liquid, along a horizontal line passing through the droplet center (see Fig. 1). The comparison between measured and predicted temperature distributions is given in Fig. 6. The temperature distributions in the droplet interior, as displayed in Fig. 6, have been plotted versus a radial location normalized with respect to ini-

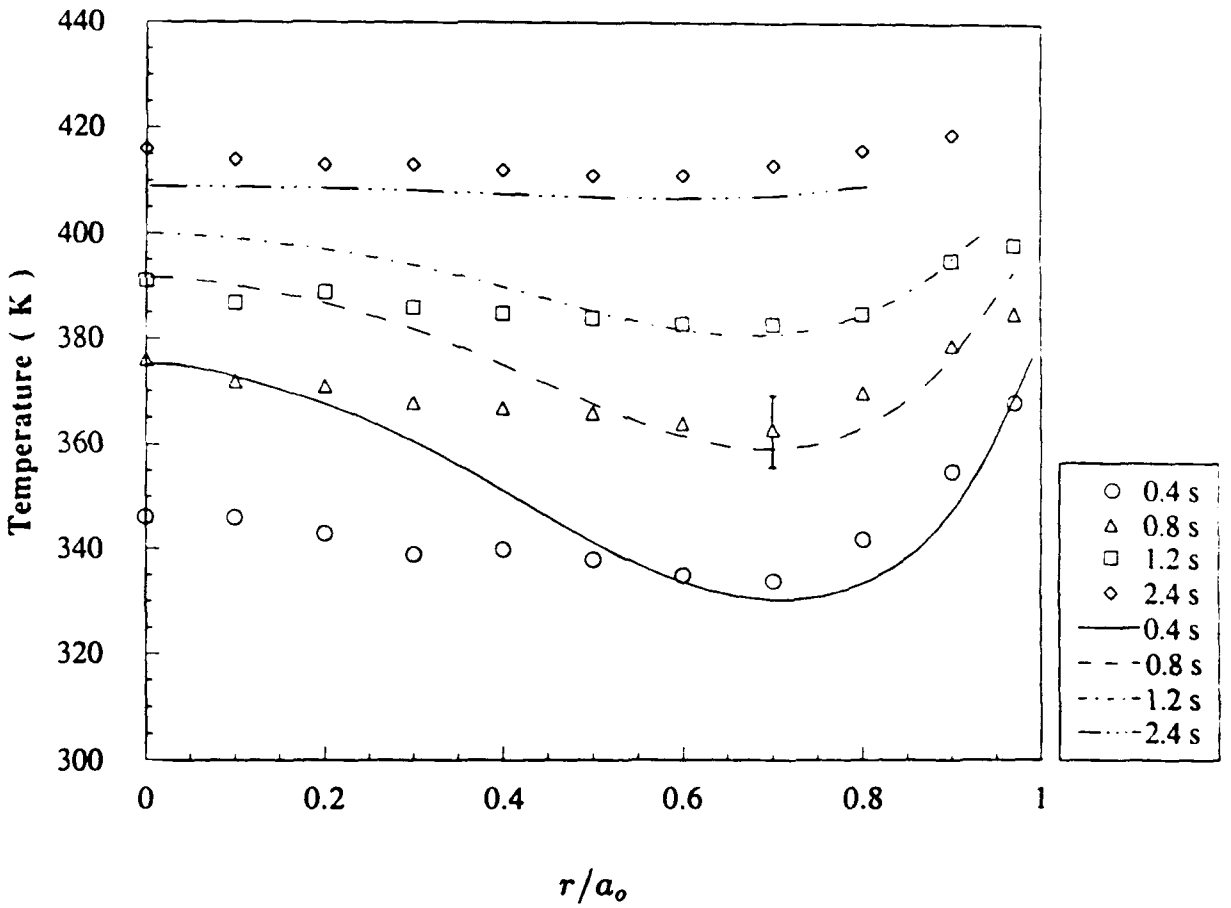

Fig. 6. Comparison between numerically predicted (curves) and experimentally measured (symbols [15]) temperature distributions in the droplet interior at four different instances of the droplet lifetime (0.4, 0.8, 1.2, and 2.4 s). The data have been plotted versus a radial location normalized with respect to the initial droplet radius. The error bar displays the scatter of the experimental data reported in Ref. 15.

tial droplet radius a_0. The error bar drawn on one of the experimental data points represents the scatter of the measurements reported in Ref. 15. Both experimental and predicted temperature distributions show that the minimum temperatures occur around $r/a_0 = 0.6 - 0.7$. The temperatures at the droplet core are higher than the minimum values; however, the temperature difference is substantially higher for the numerically predicted temperature radial distributions. The experimentally measured droplet-center temperatures are lower than the temperatures in the vicinity of the droplet surface. However, the numerically predicted droplet-center temperatures are almost identical to those of the droplet surface. As also mentioned in Ref. 15, this temperature distribution pattern is an outcome of the existence of internal circulation, which promotes the heat transfer mechanisms from the droplet surface to the droplet interior. The overall agreement between the measured and predicted temperature distributions is good, except in the regions near the droplet center and during the earlier stages of the droplet lifetime. The discrepancy between the predicted and measured droplet center temperatures gradually diminishes from 29 K at 0.4 s to 8 K at 2.4 s. We should note that the sudden exposure of the droplets to the free stream during the experiments [15] does involve unsteady effects with rather unpredictable consequences. To that effect, the perfectly uniform free stream imposed initially on the droplets during the numerical simulations, would be difficult to reproduce experimentally. This initial "exposure" effect might be partially responsible for the above mentioned discrepancy between the temperatures near the droplet center. In addition, the presence of thermocouple beads and wires within the droplets examined in the experiments, also act as restraining factors on the development of the liquid-phase motion, thus slowing down the heat transport processes.

Wong and Lin [15] compared the experimental radial temperature distributions at various Reynolds numbers (17, 60, and 100), and reported only minor changes, suggesting that there was no substantial enhancement of the internal liquid-core motion with increased free-stream momentum. This was demonstrated by similar (± 10 K) temperature distributions within liquid droplets exposed to ambient flows corresponding to the above mentioned different Reynolds numbers. An additional simulation was performed using the numerical model in order to examine the experimental trend. This run simulated a liquid *n*-decane droplet that was suddenly exposed to a 1000-K free stream at $Re_0 = 60$. Figure 7 compares the predicted droplet temperature distributions for $Re_0 = 17$ and 60, at four different instances of the corresponding droplet lifetimes (0.4, 0.8, 1.2, and 2.4 s). These temperatures correspond to a series of radial locations (r) within the bulk of the liquid, along a horizontal line passing through the droplet center (Fig. 1). The distributions have been plotted versus a radial location normalized with respect to the initial droplet radius a_0. As in the $Re_0 = 17$ case, the temperature distributions for $Re_0 = 60$ (curves marked with symbols) show that the minimum temperatures occur around $r/a_0 = 0.6 - 0.7$. It is important to note that even though the predicted droplet surface temperatures for the Re = 60 case are slightly higher (by 10 K or so) than those of the Re = 17 droplet at corresponding instances, the overall temperature distributions in the droplet interior are very similar (within experi-

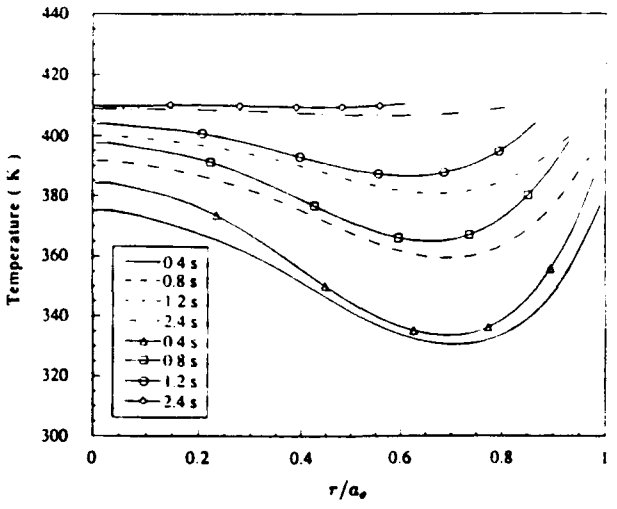

Fig. 7. Comparison of numerically predicted droplet temperature distributions for $Re_0 = 17$ and 60, at four different instances of the corresponding droplet lifetimes (0.4, 0.8, 1,2 and 2.4 s). The curves marked with symbols correspond to $Re_0 = 60$. The data have been plotted versus a radial location normalized with respect to the initial droplet radius.

mental detection limitations) for both values of Re_0. Our simulations confirm that a considerable increase of free-stream momentum fails to have a substantial effect on the temperature distribution within the droplet interior. This trend is entirely consistent with the results reported in Ref. 15. However, the conjecture of Wong and Lin [15] that similar liquid temperature distributions also suggest insensitivity of the internal liquid-core motion to free-stream momentum is misleading. The numerical simulations also show (Fig. 7) that the higher Re_0 droplet vaporizes faster, as indicated by the lower values of r/a_0 at the right end of each curve, when compared with the one corresponding to the lower Re_0 droplet. The faster vaporization rates associated with higher Re_0 are attributed to more efficient heat transport from the gas to the droplet interface [12]. Figure 8 shows the temporal variation of surface-averaged temperatures and volumes for the two droplets compared (Re_0 = 17, 60). The droplet volumes have been normalized with respect to their initial values. The average liquid-surface temperatures for the lower Re_0 droplet are by 10 K lower than those of $Re_0 = 60$ at the early stages of the droplet lifetimes. The two temperatures

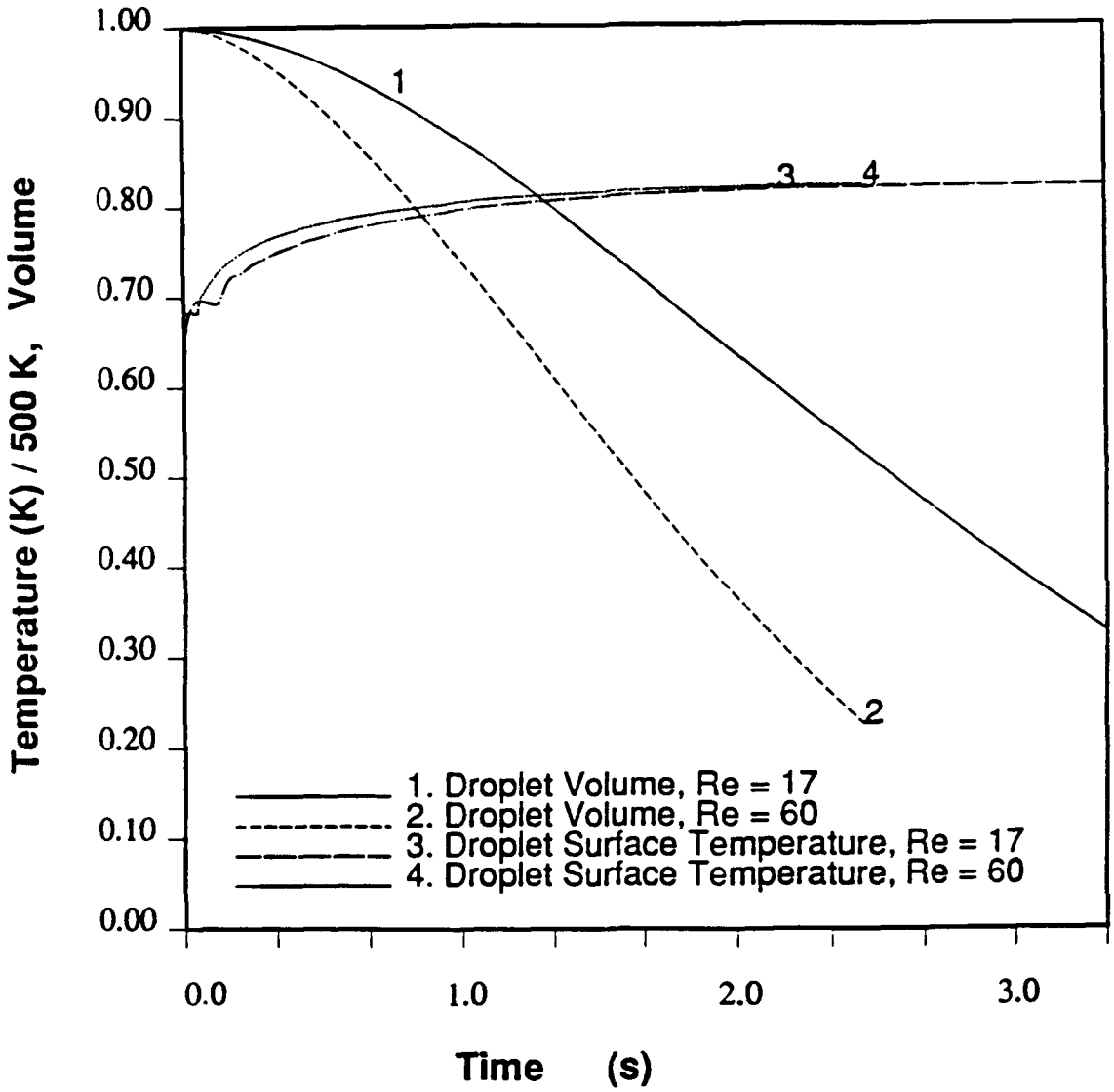

Fig. 8. Temporal variations of surface-averaged temperatures and volumes, as predicted by the model, for two droplets exposed to different ambient streams (Re_0 = 17, 60). The volumes have been normalized with respect to their initial values.

subsequently converge as time proceeds. The numerical simulations also revealed that stronger ambient flows result in substantially enhanced liquid-phase circulating motion, as indicated by the increased values of the circumferential component of the liquid velocity on the droplet surface. In addition, stronger ambient flows result in a substantial enhancement of the liquid evaporation rates, as shown by the significantly lower values of droplet volume corresponding to the $Re_0 = 60$ simulation (Fig. 8). To this end, even though the liquid temperatures appear to be relatively insensitive to ambient momentum, both liquid-phase circulation and vaporization dynamics are highly dependent on the strength of the gaseous stream.

In order to obtain more information about internal droplet dynamics and heat transport mechanisms related to liquid motion, Wong and Lin [15] also measured droplet temperature distributions with increased liquid viscosity. High-viscosity fuels were prepared by dissolving 5% or 10% (weight) of polystyrene in JP-10. The resulting viscosities were respectively 6 and 22 times higher than that of pure JP-10 fuel. It was reported [15] that for identical Re_0, higher-viscosity droplets showed internal temperatures with a monotonically decreasing trend toward the droplet center, thus indicating that the vortex structure in the liquid bulk is inapplicable. The above observations were examined using the numerical model and performing an additional simulation (at $Re_0 = 17$) with an artificially higher liquid viscosity (ten times larger than that employed in the base case). Figure 9 shows the temperature distributions at four different instances of the higher-viscosity simulation (0.4, 0.8, 1.2, and 2.4 s). These temperatures correspond to a series of radial locations (r) within the bulk of the liquid, and along a horizontal line passing through the droplet center (see Fig. 1). In contrast to our observations in the base-case simulation and in agreement with Ref. 15, the minimum temperatures during the early stages of the high-viscosity calculation do occur at the droplet center (Fig. 9; 0.4 s curve). However, even though the higher liquid viscosities slow down the initial development of the liquid-phase motion, the predicted temperature distributions reveal the presence of a weak liquid vortex at later times (curves for 0.8 and 1.2 s). It is also apparent that higher liquid viscosities result in lower temperature differences between the vortex core and the droplet center (compare corresponding distributions of Figs. 6 and 9). Figure 10 shows the liquid temperature contours at two different times (0.4 and 1.2 s) of the high-viscosity simulation. Comparing Figs. 2b and 10a, it is apparent that liquid viscosity affects the strength of the liquid circulating motion: note the fully developed toroidal structure within the low viscosity droplet (Fig. 2b) versus the still developing character of the high-viscosity droplet (Fig. 10a). In fact, as Fig. 10b indicates, the high-viscosity droplet does not reach the fully developed state even at late stages of the simulation. The lowest liquid temperatures in the high-viscosity droplet are established at regions off the droplet axis and at an angular location closer to the front stagnation point of the flow. Apparently, this thermal pattern inhibits the detection of the liquid-phase circulating motion when the thermocouple is traversed along a line passing from the droplet center at 90° from the front stagnation point of the flow. It is worth noting that for the experimentally studied vaporizing droplets [15], the gradually increasing polystyrene concentration with time causes increasing viscosities due to the reduc-

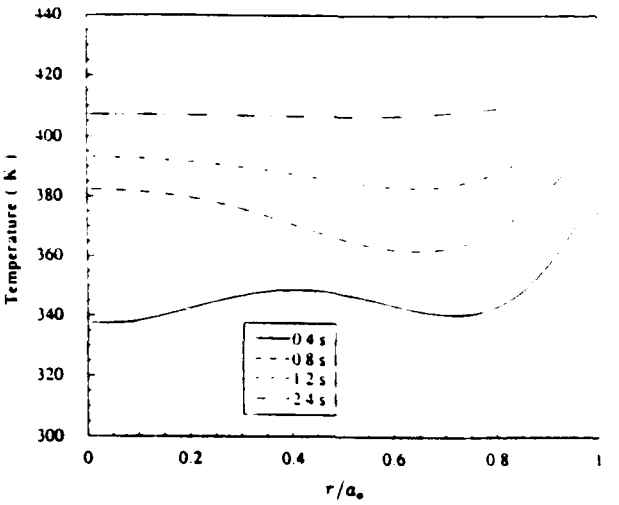

Fig. 9. Numerically predicted temperature distributions for the droplet interior at four different instances of the higher liquid-viscosity simulation (0.4, 0.8, 1.2, and 2.4 s). The data have been plotted versus a radial location normalized with respect to the initial droplet radius.

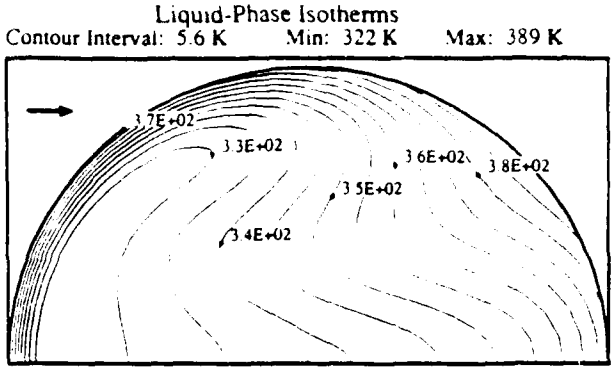

Fig. 10. Numerically predicted isothermal contours within a liquid *n*-decane droplet at two different instances (0.4 and 1.2 s) of the high-viscosity simulation. The gaseous flow direction is indicated by the arrow.

tion of the mass of the evaporating fuel. Even though this variation is not expected to affect the measured temperature distributions in a dramatic way, it does have an unclear effect on direct comparisons between the experimentally measured and the numerically predicted temperature distributions. Finally, an additional source of discrepancy is attributed to the interaction between thermocouple wires and polystyrene during the experimental observations in the droplet interior. The effect of this interaction should be more pronounced for increased polystyrene concentrations, thus reducing the reliability of the experimentally determined temperature distributions for the polystyrene-doped droplets.

CONCLUSIONS

The data of a recent experimental investigation performed by other researchers on suspended, evaporating droplets is used to evaluate and validate the methods employed in a detailed numerical model simulating the vaporization behavior of liquid droplets vaporizing at high-temperature convective conditions. The model uses numerical techniques previously employed to examine the evaporation of droplets that are transported in a laminar, high-temperature, gaseous stream. A series of comparisons has been performed between model-predicted and experimentally measured vaporization rates and internal temperature distributions at atmospheric pressures and Reynolds numbers below 100, that are representative of practical situations of interest. The agreement between experimental measurements and model predictions on the temporal variation of certain temperatures in the droplet interior is good, with largest discrepancies occurring near the droplet center. The predicted temperature distributions in the droplet interior are also in very good agreement with those measured experimentally throughout the droplet lifetime, with the exception of regions near the droplet center and during the early stages of the droplet lifetime. Both experiments and modeling agree on the establishment of internal circulation in liquid vaporizing droplets exposed to laminar, high-temperature, gaseous flows. In addition, the model predicts slightly higher liquid vaporization rates, as indicated by consistently lower values (up to 10%) of the droplet diameter throughout the droplet lifetime.

Comparisons of the calculated internal droplet temperature distributions for two different values of the Reynolds number showed that a considerable increase of free-stream momentum failed to have a substantial effect on the temperature distributions within the droplet interior. This observation is consistent with the results reported in the relevant experimental investigation. However, the model predictions suggest that liquid-phase circulation and vaporization dynamics are highly influenced by ambient momentum. The model predictions showed that substantially increased liquid viscosities affect the establishment and the strength of the liquid-phase motion. On the other hand, the experimental observations concluded that substantially higher liquid viscosities eliminate the liquid-phase motion entirely.

The above comparisons show that the experiment suggests a weaker liquid-phase motion than that predicted by the model. Some possible sources for disagreement between experiment and theory were discussed in the context of the experimental setup and the limitations of the employed instrumentation. In conclusion, the overall agreement between model predictions and experimental measurements shows that modeling can be used in a reliable manner to examine liquid-droplet convective evaporation under conditions that are not easily reproduced experimentally, or when time constraints prohibit any experimental setup implementation.

This work was sponsored in part by the Air Force Office of Scientific Research, Air Force Systems Command, USAF, under grant number AFOSR 92-J-0476. The support of the Pittsburgh Supercomputing Center through an allocation of computer time on the Cray Y-MP is also acknowledged with appreciation. The author also wishes to acknowledge Ms. Jie Zhang for the assistance provided in the preparation of the figures.

REFERENCES

1. Law, C. K., *Prog. Ener. Combust. Sci.* 8:171–201 (1982).
2. Faeth, G. M. *Prog. Ener. Combust. Sci.* 9:1–76 (1983).
3. Sirignano, W. A. *Prog. Ener. Combust. Sci.* 9:291–322 (1983).
4. Dwyer, H. A., *Prog. Ener. Combust. Sci.* 15:131–158 (1989).
5. Kuo, K. K. *Principles of Combustion*, J. Wiley, New York, 1986, p. 370.
6. McDonald, J. E., *J. Meteor.* 11:478–494 (1954).
7. LeClair, B. P., Hamielec, A. E., Pruppacher, H. R., and Hall, W. D., *J. Atmos. Sci.* 29:728–740 (1972).
8. Winter, M., and Melton, L. A., *Appl. Opt.* 29: 4574–4577 (1990).
9. Prakash, S., and Sirignano, W. A., *Int. J. Heat Mass Transf.* 23:253–268 (1980).
10. Renksizbulut, M., and Haywood, R. J., *Int. J. Multiphase Flow* 14:189–202 (1988).
11. Haywood, R. J., Nafziger, R., and Renksizbulut, M., *J. Heat Transf.* 111:495–502 (1989).
12. Chiang, C. H., Raju, M. S., and Sirignano, W. A., *Int. J. Heat Mass Transf.* 35:1307–1324 (1992).
13. Megaridis, C. M., and Sirignano, W. A., *Twenty-Third Symposium (International) on Combustion*, The Combustion Institute, Pittsburgh, 1990, p. 1413.
14. Renksizbulut, M., Nafziger, R., and Li, X., *Chem. Eng. Sci.* 46:2351–2358 (1991).
15. Wong, S.-C., and Lin, A.-C., *J. Fluid Mech.* 237: 671–687 (1992).
16. Chiang, C. H., Ph.D. thesis, University of California Irvine, 1990.
17. Westbrook, C. K., *J. Comput. Sci.* 29:67–80 (1978).
18. Rivkind, V. Ya., and Ryskin, G. M., *Fluid Dyn.* 1:5–1. (1976).
19. Reid, R. C., Prausnitz, J. M., and Sherwood, T. K. *The Properties of Gases and Liquids*, McGraw-Hill New York, 1977.
20. Abramzon, B., and Sirignano, W. A., *Proceedings o the Second ASME-JSME Thermal Engineering Join Conference*, Honolulu, 1987, Vol. 1, p. 11.
21. White, F. M., *Viscous Fluid Flow*, McGraw-Hill, Nev York, 1974, p. 28.

Received 23 July 1992; revised 11 December 1992

APPENDIX: FLUID THERMOPHYSICAL PROPERTIES

The physical properties of the air–vapor mixture surrounding the vaporizing droplet were calculated using standard mixing rules involving the properties of the two gaseous components. The inverse density of the mixture was correlated by the mass-fraction weighted average of the inverse densities of air and *n*-decane vapor. In addition, the mixture heat capacity was calculated by a mass-fraction weighted rule, while the dynamic viscosity of the mixture was determined by Wilke's formula [19]. Finally, the thermal conductivity of the gas mixture was estimated using Mason and Saxena's modification of the Wassiljewa conductivity expression [19].

The properties of *n*-decane vapor and air were approximated as functions of temperature (in degrees K). For *n*-decane vapor (molecular weight 142.3 kg/kmol) the following correlations were used:

dynamic viscosity [20]:

$$\mu_v = 5 \times 10^{-6} + 1.75 \times 10^{-8}(T - 300) \quad \text{kg/m/s}$$

thermal conductivity [20]:

$$k_v = 4.2 \times 10^{-7} T^{1.8} \quad \text{W/m/K}$$

heat capacity [20]:

$$c_{p_v} = 106.6 + 5.76T - 1.67 \times 10^{-3} T^2 - 4.73 \times 10^{-7} T^3 \quad \text{J/kg/K:}$$

$T < 800$ K

and

$$c_{p_v} = 410.9 + 5.46T - 2.48 \times 10^{-3}T^2 + 4.23 \times 10^{-7}T^3 \quad \text{J/kg/K}; \qquad T \geq 800 \text{ K}$$

mass diffusion coefficient of n-decane in air [20]:

$$D = 6.54 \times 10^{-10}T^{1.583} \quad \text{m}^2/\text{s}$$

For air (molecular weight 28.96 kg/kmol) the following correlations were used:
dynamic viscosity (Sutherland law [21]):

$$\mu_{\text{air}} = \frac{1.46 \times 10^{-6}T^{1.5}}{T + 110.6} \quad \text{kg/m/s}$$

thermal conductivity (Sutherland law [21]):

$$k_{\text{air}} = \frac{2.5 \times 10^{-3}T^{1.5}}{T + 194.4} \quad \text{W/m/K}$$

heat capacity [20]:

$$c_{p_{\text{air}}} = 1008 \quad \text{J/kg/K}; \qquad T < 400 \text{ K}$$

and

$$c_{p_{\text{air}}} = 920.5 + 0.218T \quad \text{J/kg/K}; \qquad T \geq 400 \text{ K}$$

For liquid n-decane the following values and correlations were used:
density:

$$\rho_l = 730 \text{ kg/m}^3$$

dynamic viscosity [19]:

$$\mu_l = 11.6 \times 10^{-6} \exp(1286.2/T) \quad \text{kg/m/s}$$

thermal conductivity [20]:

$$k_l = 0.129 \quad \text{W/m/K}$$

heat capacity [20]:

$$c_{p_l} = 2.22 \times 10^3 \quad \text{J/kg/K}$$

The temperature variation of the latent heat of vaporization of n-decane is given by [20]

$$L = 276\left(\frac{T_{\text{cr}} - T}{T_{\text{cr}} - T_b}\right)^{0.38} \quad \text{kJ/kg},$$

where $T_{\text{cr}} = 617.6$ K is the critical temperature, and $T_b = 447.3$ K the normal boiling point of n-decane.